Title
Model Order Reduction Methods for Meshfree Approximation of Problems with Singularities and Discontinuities

Author
Marodon, Camille

Publication Date
2013

Peer reviewed|Thesis/dissertation

UNIVERSITY OF CALIFORNIA

Los Angeles

Model Order Reduction Methods for Meshfree Approximation of Problems with Singularities and Discontinuities

A dissertation submitted in partial satisfaction of the
requirements for the degree Doctor of Philosophy
in Civil Engineering

by

Camille Marodon

2014

ABSTRACT OF THE DISSERTATION

Model Order Reduction Methods for Meshfree Approximation
of Problems with Singularities and Discontinuities

by

Camille Marodon
Doctor of Philosophy in Civil Engineering
University of California, Los Angeles, 2014
Professor Jiun-Shyan Chen, Chair

The modeling of problems with singularities and discontinuities, such as cracks in elastic media, is one of the most challenging problems in computational mechanics. The numerical solution of such problems necessitates sufficient resolution in the discretization, which is very costly. In this work, model order reduction (MOR) techniques are developed for problems with singularities based on meshfree methods. Theoretical investigation on the performance of the proposed methods via error estimation, stability analysis, and complexity analysis is also carried out in this research.

In the first part of this work, the full discrete model is constructed using meshfree approximation along with enrichment techniques to properly approximate singularities and discontinuities. This, on the other hand requires high order quadrature rules for sufficiently accurate integration of enrichment functions and their derivative. Instead, an integrated singular basis function method (ISBFM) is introduced to circumvent this difficulty. If the enrichment basis functions are properly selected so that they satisfy the governing equation and the boundary conditions on the boundaries connected to the singularity point, the resulting ISBFM Galerkin formulation considers only the integration of the enrichment functions on the boundaries away from the singularity point. This

ISBFM Galerkin formulation also allows effective MOR procedures proposed in this work.

Two MOR methods via projection of a discrete system obtained from the ISBFM Galerkin formulation have been proposed. These are the ISBFM-UR method based on a uniform projection, and the ISBFM-DR method based on the decomposed projection of the full scale system. The ISBFM-UR method projects all smooth and non-smooth DOF to the reduced order space, while the ISBFM-DR method projects smooth and non-smooth DOF separately in order to retain the singular behavior of the full scale solution.

Error estimation and stability analysis show that the reduced order solution from the ISBFM-DR method with the decomposed projection can achieve a much-enhanced accuracy with only slight increase of condition number compared to the ISBFM-UR method with uniform project. It is shown in the error estimation and confirmed by the numerical results that the errors of the two MOR methods is mainly controlled by the right hand side vectors of the full and reduced order systems. While the stability analysis shows that the two MOR methods provide better conditioning that the full scale system, it also suggests that the conditioning of the ISBFM-DR method is somewhat compromised by its better accuracy compared to that of the ISBFM-UR method. Nevertheless, the complexity analysis shows that the ISBFM-DR method does provide a slightly better efficiency in addition to the enhanced accuracy compared to the ISBFM-UR method.

The proposed MOR methods are applied Poisson problems with singularities and LEFM problems. The numerical tests validate the effectiveness of the proposed MOR methods, and the numerical results on accuracy and stability of the proposed methods are also shown to be in good agreement with the analytical predictions carried in this research.

The dissertation of Camille Marodon is approved.

Stanley B. Dong

Ertugrul Taciroglu

Joseph M. Teran

Jiun-Shyan Chen, Committee Chair

University of California, Los Angeles

2014

To my parents Martine and Claude,

Contents

List of Figures

List of Tables

ACKNOWLEDGEMENTS

First of all, I would like to sincerely express my thanks and gratitude to my advisor, Professor J. S. Chen. He introduced me to the world of computational mechanics and gave me this great opportunity to be part of his research group. This dissertation would not have been possible without his guidance, patience and support. Thanks are also extended to the members of the doctoral committee, Professor Stanley Dong, Professor Ertugrul Taciroglu, and Professor Joseph Teran for their insightful comments.

I would like to acknowledge Professor Hsin-Yun Hu at Tunghai University for her valuable collaboration while working closely on my research presented in Chapter 7. Her support and encouragement were also greatly appreciated.

The sponsorship of this research by the US Army Engineer Research Development Center for UCLA is also greatly acknowledged.

Thanks go to my current and previous coworkers for their friendship and assistance and for the great discussions we had at the office and over memorable dinners.

I would like to thank Dr. Zeynep Tuna for being such a wonderful friend and for inspiring me throughout my graduate studies at UCLA. She was part of this invaluable group of friends who came from so many different places and with whom I have shared so many good memories during the last five years. Thank you all, and may those who are still working on their thesis find what they are researching for.

Last but not the least, I would like to especially thank my parents Claude and Martine, my brothers Cédric and Cyril, my sister Cécile, but also my dear Sébastien and our amazing families, who sent me so much love and support and even managed to cross many oceans to visit me. A special thank to Louis and Maxime, the latest additions to my family who have bring me lots of joy this year.

VITA

Camille Marodon

Education

2009 M.S., Civil Engineering, École Spéciale des Travaux Publics, Paris, France.

2009 M.S., Civil Engineering, University of California, Los Angeles, USA.

Work Experience

2011-2012	Teaching assistant coordinator, Civil & Environmental Engineering Department, University of California, Los Angeles. Instructed workshops for teaching assistants.
2010	Teaching assistant, HSSEAS-Master of Science Online Program, University of California, Los Angeles. Instructed discussion for finite element method graduate course.
2009-2010	Teaching assistant, Civil & Environmental Engineering Department, University of California, Los Angeles. Instructed discussion for mechanics of solids undergraduate course.
2009-present	Graduate student researcher, Civil & Environmental Engineering Department, University of California, Los Angeles. Performed research and work on applications of meshfree methods.

Research Experience

Theory and application of meshfree methods

- RKPM semi-Lagrangian formulation for extremely large deformation problems
- Enriched RKPM for Poisson problems with singularities and linear elastic fracture mechanics problems

Image based computational mechanics for bio-mechanics

- Level set method and segmentation algorithm to identify boundaries and material interfaces
- Application to the modeling of a 3D musculoskeletal system

Model order reduction methods

- Application to enriched meshfree approximation of problems with singularities and discontinuities
- Analysis of accuracy, stability and complexity of reduced methods

Publications and Presentations

1. Chen, J. S., Marodon, C. and Hu, H. Y. Model Order Reduction for Enriched Meshfree Solution of Linear Elastic Fracture Mechanics Problems, under preparation.
2. Chen, J. S., Marodon, C. and Hu, H. Y. Model Order Reduction for Meshfree Solution of Singularity Problems, under preparation.
3. Marodon, C., Chen, J. S. and Hu, H. Y. Reduced Meshfree Approximation of Static Singular Problems, Abstract and Presentation, 12th US National Congress of Computational Mechanics, Raleigh, North Carolina, July 22-25, 2013.
4. Marodon, C., Chen, J. S. and Chi, S. W. Reproducing Kernel Based Image Segmentation and Computational Biomechanics, Abstract and Presentation, 11th US National Congress of Computational Mechanics, Minneapolis, Minnesota, July 25-28, 2011.
5. Chen, J. S., Chi, S. W., Lee, C. H., Lin, S. P., Marodon, C., Roth, M. J. and Slawson, T. R. A Multiscale Meshfree Approach for Modeling Fragment Penetration into Ultra High-Strength Concrete. Final Report, ERDC/GSL TR-11-35, 2011.
6. Marodon, C., Chen, J. S. and Chi, S. W. Image Based Computational Method for Bio-Mechanics, Abstract and Presentation, 9th World Congress on Computational Mechanics, Sydney, Australia, July 19-23, 2010.

Chapter 1

Introduction

1.1 Motivation

Recent advances in virtual reality require real time simulation capabilities in order to provide realistic training such as virtual combat, virtual surgery, and driving simulators. However, such activities require complex models with high efficiency in many engineering and scientific applications. Modeling complex physical phenomena such as crack formation and fragmentation requires high fidelity models, with high demand for data storage and communication. These challenges necessitate techniques for achieving both computational efficiency and accuracy. Significant efforts have been devoted to the development of adaptive model refinement and model order reduction (MOR) techniques to advance computational mechanics into the new frontier of "Simulation Based Engineering Science".

The purpose of MOR methods is to provide a projection of the original approximation space to a much smaller finite dimensional space while minimizing the loss of accuracy. Issues encountered in large-scale systems such as data storage and computational intensity can be relieved by introducing a reduced order projection provided with an acceptable loss of accuracy. Current MOR methods are typically formulated under the mesh based computational framework, which can be ineffective in large deformation problems and problems with evolving discontinuities and

singularities. The motivation for this dissertation is to develop new MOR approaches, based on enhanced projection techniques, for improved accuracy in the reduced order modeling of problems with singularities and discontinuities that are often encountered in fragment-impact applications.

1.2 Objective

The objective of this dissertation is to address the challenges in the reduced order modeling of problems with singularities and discontinuities. The main tasks of this dissertation can be summarized as follows:

- Investigation of enhanced Galerkin formulation for enriched meshfree approximation as a pre-conditioner for an optimal MOR. In this work, the full model is constructed from the integrated boundary singular function method (IBSFM). This technique avoids using high order quadrature for the domain and boundary integrals near the singularity point. This technique is first introduced for Poisson problems with singularities and is then extended to linear elastic fracture mechanics (LEFM).

- Development of MOR for problems with singularities and discontinuities. Typically, meshfree methods such as the reproducing kernel particle method (RKPM) or the element free Galerkin (EFG) method introduce enrichment functions for achieving high accuracy in problems with rough solutions. For example, the asymptotic crack tip displacement field can be introduced as an enrichment function in fracture mechanics problems. Under this construction of the finite dimensional scape, the RKPM and EFG solutions can be decomposed into a smooth meshfree approximation and a non-smooth enriched approximation. An MOR approach is investigated that introduces a reduced projection of the smooth part of the solution, and constructs the total solution by superposition of the reduced smooth solution and unreduced non-smooth solution represented by the enrichment functions. This approach is compared to an MOR approach that projects both smooth and non-smooth part of solutions

altogether.

- Theoretical investigation on the performance of the proposed MOR methods via error estimation, stability analysis, and complexity analysis. These analytical predictions on the numerical performance of the proposed methods are validated with the numerical results in the benchmark problems.

- Applications of the MOR methods to problems of interest such as Poisson problems with singularities (due to domain geometry) and stationary crack problems in fracture mechanics.

1.3 Outline

This dissertation is organized as follows. Chapter 2 provides a literature review for meshfree methods and enrichment techniques for solving problems with singularities and discontinuities, as well as several commonly used MOR methods. In Chapter 3, ISBFM is introduced along with enriched reproducing kernel approximations for Poisson problems with singularities. In Chapter 4, two proposed MOR methods that are well suited for problems with singularities and discontinuities are discussed in detail. An extension of the ISBFM technique to stationary crack problems is investigated in Chapter 5. Chapter 6 addresses the application of the proposed MOR methods to two dimensional linear elastic fracture mechanics. The error estimation as well as stability and complexity analyses of the two proposed reduced systems are presented in Chapter 7, and numerical examples along with discussions are provided to illustrate the effectiveness of the proposed methods. Finally, a summary of this work and concluding remarks are given in Chapter 8.

Chapter 2

Literature Review

2.1 Review of Meshfree Methods

2.1.1 Background

Meshfree methods offer purely node-based approximations and discretizations for solving boundary value problems. The domain of interest is discretized completely by nodes, and the methods do not rely on an interconnected mesh. In mesh-based methods like the finite element method (FEM), mesh distortion may occur when the material undergoes large deformation due to the topology of the discretization and the connectivity between nodes. Meshfree methods offer flexibility for the nodal distribution and only use nodal information for the approximation. The methods have efficiently been applied to problems where FEM encounters difficulty, such as simulation of crack growth, strain localization problems, and large deformation analysis, among others.

Meshfree methods were first introduced in 1977 by Lucy [Lucy, 1977] and by Gingold and Monaghan [Gingold and Monaghan, 1977], who presented the smooth particle hydrodynamics (SPH) for applications in astrophysics. Gingold and Monaghan presented SPH as a kernel estimate, which now characterizes most particle methods. However, SPH approximations encounter difficulty in the treatment of boundary conditions and lacks of stability. Methods have then been

developed to improve its accuracy and efficiency as well [Libersky and Petschek, 1991] [Randles and Libersky, 1996].

Lancaster and Salkauskas [Lancaster and Salkauskas, 1981] proposed interpolants constructed by moving least squares (MLS), that were later introduced by Nayroles et al. [Nayroles et al., 1992] in the diffuse element method (DEM) for solving partial differential equations (PDEs). The EFG method was proposed by Belytschko et al. [Belytschko et al., 1994] [Lu et al., 1994], as a modification of DEM, which used the real derivatives in MLS, and performed a study on the choice of the weight functions in MLS for solving PDEs.

Melenk and Babuška developed the partition of unity method (PUM) [Melenk and Babuška, 1996], which provides global conforming finite element approximation spaces for any order of regularity. The PUM was applied to rough problems [Babuška and Melenk, 1997], for which the local singular behavior of the solution is embedded in the construction of the PUM approximation space.

Liu et al. [Liu et al., 1995b] introduced RKPM, an approximation method based on the correction of kernel estimates that ensures polynomial reproducing conditions. The application of RKPM is quite extensive in the solid mechanics field. Chen et al. proposed an RKPM formulation to large deformation problems including hyper-elasticity and plasticity [Chen et al., 1996] [Chen et al., 1997] [Chen et al., 1998] as well as fragment impact problems [Guan et al., 2011]. The method was also extended to nearly incompressible problems [Chen et al., 2000] and structural dynamics [Liu et al., 1995a]. As a typical example of meshfree methods, the RKPM formulation will be used for the remainder of this dissertation, and is discussed in detail in the following section.

2.1.2 Reproducing Kernel Particle Method

The reproducing kernel (RK) approximation of a function u , denoted as u^h , is expressed in (2.1) as a linear combination of N RK shape functions as follows

$$u^h(\boldsymbol{x}) = \sum_{i=1}^{N} \Psi_i(\boldsymbol{x}) d_i = \sum_{i=1}^{N} C\left(\boldsymbol{x}; \boldsymbol{x} - \boldsymbol{x}_i\right) \Phi_a \left(\frac{\|\boldsymbol{x} - \boldsymbol{x}_i\|}{a} \right) d_i \tag{2.1}$$

where $\boldsymbol{x}_i$ are the nodal coordinates of each of the N particles, d_i are nodal coefficients and Ψ_i are the RK shape functions composed of a compactly supported kernel Φ_a multiplied by a correction function C . The compact support of the kernel function provides locality to the shape functions. In this manner, the shape function associated with a node is in interaction with only a small group of neighboring nodes. This provides computational efficiency in the construction of the shape function as well as better conditioning in the linear system associated with the function approximation.

The kernel function Φ_a also determines the order of continuity of the RK shape function. The cubic-B splines and quintic-B splines, defined respectively as

$$\Phi_a(z) = \begin{cases} 1 - 6z^2 + 6z^3, & 0 \leq z < \frac{1}{2} \\ 2(1-z)^3, & \frac{1}{2} \leq z < 1 \\ 0, & z \geq 1 \end{cases} \tag{2.2}$$

and

$$\Phi_a(z) = \begin{cases} 1 - \frac{90}{11} z^2 + \frac{405}{11} z^4 - \frac{405}{11} z^5, & 0 \leq z < \frac{1}{3} \\ \frac{17}{22} + \frac{75}{22} z - \frac{315}{11} z^2 + \frac{675}{11} z^3 - \frac{1215}{22} z^4 + \frac{405}{22} z^5, & \frac{1}{3} \leq z < \frac{2}{3} \\ -\frac{81}{22}(z-1)^5, & \frac{2}{3} \leq z < 1 \\ 0, & z \geq 1 \end{cases} \tag{2.3}$$

are commonly used as kernel functions, where $z = \|\boldsymbol{x} - \boldsymbol{x}_i\|/a$, $\boldsymbol{x}_i$ is the nodal coordinates, a is

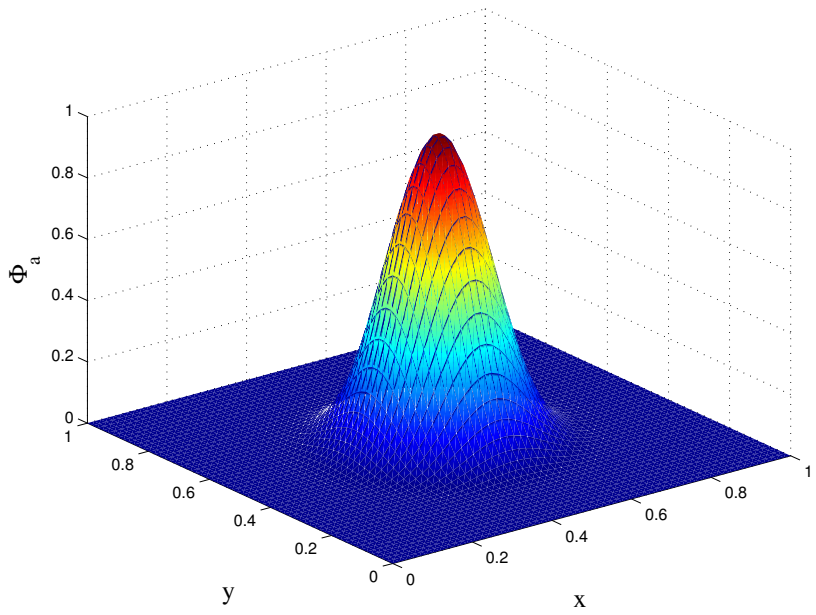

Figure 2.1: Cubic-B spline kernel function

the support size of the function. In this dissertation, the cubic-B spline, which is C^2 continuous and shown in Figure 2.1 for illustration, is employed as the kernel function in the RK approximation.

The correction function C , defined as

$$C(\boldsymbol{x};\boldsymbol{x}-\boldsymbol{x}_i)=\sum_{|\alpha|\leq n}(\boldsymbol{x}-\boldsymbol{x}_i)^{\alpha}b_{\alpha}(\boldsymbol{x})=\boldsymbol{H}^{\mathrm{T}}(\boldsymbol{x}-\boldsymbol{x}_i)\boldsymbol{b}(\boldsymbol{x}) \tag{2.4}$$

where monomials up to degree n are used as bases, i.e. $\boldsymbol{H}^{\mathrm{T}}(\boldsymbol{x})=[\boldsymbol{x}^{\alpha}]_{|\alpha|\leq n}$, is introduced to the shape function in order to impose the order of completeness in the approximation. The coefficient vector $\boldsymbol{b}$ is obtained by satisfying the following reproducing conditions

$$\sum_{i=1}^{N}C\left(\boldsymbol{x};\boldsymbol{x}-\boldsymbol{x}_i\right)\Phi_a\left(\frac{\|\boldsymbol{x}-\boldsymbol{x}_i\|}{a}\right)\boldsymbol{x}_i^{\alpha}=\boldsymbol{x}^{\alpha},|\alpha|\leq n \tag{2.5}$$

The above can also be written as

$$\sum_{i=1}^{N} C(\boldsymbol{x};\boldsymbol{x}-\boldsymbol{x}_i)\Phi_a\left(\frac{\|\boldsymbol{x}-\boldsymbol{x}_i\|}{a}\right)(\boldsymbol{x}-\boldsymbol{x}_i)^{\alpha}=\delta_{|\alpha|,0},\ |\alpha|\leq n \tag{2.6}$$

which leads to

$$\sum_{i=1}^{N} \boldsymbol{H}(\boldsymbol{x}-\boldsymbol{x}_i)\boldsymbol{H}^{\mathrm{T}}(\boldsymbol{x}-\boldsymbol{x}_i)\Phi_a\left(\frac{\|\boldsymbol{x}-\boldsymbol{x}_i\|}{a}\right)\boldsymbol{b}(\boldsymbol{x})=\boldsymbol{H}(\boldsymbol{0}) \tag{2.7}$$

Using (2.7), the coefficient vector is obtained by

$$\boldsymbol{b}(\boldsymbol{x})=\boldsymbol{M}^{-1}(\boldsymbol{x})\boldsymbol{H}(\boldsymbol{0}) \tag{2.8}$$

where

$$\boldsymbol{M}(\boldsymbol{x})=\sum_{i=1}^{N} \boldsymbol{H}(\boldsymbol{x}-\boldsymbol{x}_i)\boldsymbol{H}^{\mathrm{T}}(\boldsymbol{x}-\boldsymbol{x}_i)\Phi_a\left(\frac{\|\boldsymbol{x}-\boldsymbol{x}_i\|}{a}\right) \tag{2.9}$$

is the moment matrix. The construction allows the RK approximation to exactly reproduce monomials up to degree n and therefore the partition of unity property holds. The RK shape functions and u^h are then obtained as

$$\Psi_i(\boldsymbol{x})=\boldsymbol{H}^{\mathrm{T}}(\boldsymbol{0})\boldsymbol{M}^{-1}(\boldsymbol{x})\boldsymbol{H}(\boldsymbol{x}-\boldsymbol{x}_i)\Phi_a\left(\frac{\|\boldsymbol{x}-\boldsymbol{x}_i\|}{a}\right) \tag{2.10}$$

$$u^h(\boldsymbol{x})=\sum_{i=1}^{N} \boldsymbol{H}^{\mathrm{T}}(\boldsymbol{0})\boldsymbol{M}^{-1}(\boldsymbol{x})\boldsymbol{H}(\boldsymbol{x}-\boldsymbol{x}_i)\Phi_a\left(\frac{\|\boldsymbol{x}-\boldsymbol{x}_i\|}{a}\right)d_i \tag{2.11}$$

It should be noted that the RK approximation is not an interpolation function, and the RK shape functions do not possess the Kronecker delta property, i.e.,

$$\Psi_i(\boldsymbol{x}_j)\neq\delta_{ij} \tag{2.12}$$

Therefore, the imposition of essential boundary conditions while solving boundary value problems

needs particular attention. Techniques that force the shape function to satisfy the nodal interpolation property have been proposed, such as boundary singular kernel (BSK) [Chen and Wang, 2000] [Chen et al., 2003]. The coupling of RK shape functions with finite elements [Fernández-Méndez and Huerta, 2004] has also been developed to recover the Kronecker delta property at essential boundary nodes. Furthermore, transformation methods [Chen et al., 1996] [Chen and Wang, 2000] have been derived to express the nodal coefficient d_i in terms of the value of the RK shape function Ψ_i at the nodes, which eases the imposition of the kinematic constraints. Other techniques are based on a modification of the weak formulation [Fernández-Méndez and Huerta, 2004]. The essential boundary conditions can be weakly imposed using the penalty method [Zhu and Atluri, 1998], Nitsche's method [Nitsche, 1971] or the Lagrange multipliers method [Belytschko et al., 1994].

2.1.3 Numerical Treatments of Singularities and Cracks

Engineering problems with local features and singularities are difficult to solve numerically due to the roughness of the solution. Smooth approximations such as FEM and RKPM are based on recovering polynomial completeness; therefore accuracy improvement can only be made by adaptive refinements in the vicinity of the singularity [Krysl and Belytschko, 1997]. However, the remeshing process in FEM can be quite cumbersome and can result to additional error as the crack propagates. Alternatively, enrichment functions that represent the local singular characteristics of the solution are commonly introduced in the approximation for enhanced accuracy [Li et al., 1987] [Li and Lu, 2000] [Fries and Belytschko, 2010]. Various enriched approximation methods have been proposed to solve problems with singularities and discontinuities, such as the extended finite element method (XFEM) [Belytschko and Black, 1999] [Moës et al., 1999] [Fries, 2008], the enriched EFG [Belytschko et al., 1995a] [Belytschko et al., 1995b] [Fleming et al., 1997] [Belytschko and Fleming, 1999] and the enriched radial basis collocation method (RBCM) [Wang et al., 2010].

In order to approximate a non-smooth solution, the approximation space can be enriched by shape functions that represent the singular behavior. Enriched methods utilize a prior knowledge of the asymptotic solution near the singularity to select adequate singular functions, which makes them more efficient than refinement techniques. The additional functions can be added in the basis vector already composed of monomials that is used to construct the approximation space. This technique, termed intrinsic enrichment, was presented by Fleming et al. for the study of crack propagation [Fleming et al., 1997]. In this manner, no additional degrees of freedom are needed. However, when using intrinsic enrichment over the whole domain, the bases can be rapidly linearly dependent when evaluated away from the singularity point. Blending techniques were proposed to localize the enrichment to a subdomain surrounding the singularity and avoid ill-conditioning of the moment matrix in the construction of the shape functions [Belytschko et al., 1996a].

Enrichment functions can also be extrinsically added to the smooth approximation. With extrinsic enrichments, the numerical solution is approximated by a linear combination of a smooth approximation with shape functions such as RK shape functions for instance, and a non-smooth component obtained using the enrichment functions. However, the extrinsic enrichment functions result in additional degrees of freedom, which increases the size of the discrete system.

Enrichment techniques can either be employed in the whole domain or be localized by means of blending. Multiplying singular functions by blending functions introduces additional degrees of freedom and modifies the overall enrichment that can lead to a deterioration of the accuracy and the convergence rate [Chessa et al., 2003] [Fries, 2008]. Additional parameters must be determined such as the size of the enriched subdomain and the type of blending functions. The global enrichments are not polluted by blending functions, which leads to a better approximation of the non-smooth behavior of the solution, however it requires a special treatment of boundary conditions away from the singularity point.

In fracture mechanics, the geometric representation of the crack surface must be addressed. Belytschko et al. [Belytschko et al., 1994] proposed an EFG formulation to model discontinuities by truncating the support of the shape function along the crack surface. This technique, called the

visibility criterion [Belytschko et al., 1996b], however creates artificial discontinuities of the shape functions near the crack tip. Organ et al. [Organ et al., 1996] proposed to fix this defect with the diffraction criterion for non-convex boundaries. The crack surface can also be represented using the Heaviside function as an enrichment of the meshfree approximation.

In this dissertation, RKPM with global extrinsic enrichment bases will define the approximation space for solving singularity problems.

2.2 Review of Model Order Reduction

2.2.1 Background

The MOR methods have been developed to reduce the computational costs of solving large-scale systems. They project an original approximation space onto a smaller subspace, and have been developed in the context of linear dynamical systems [Antoulas and Sorensen, 2001]. These methods can be classified in two types that are formulated with either an approximation in the time domain or an approximation in the frequency domain. Methods based on singular value decomposition (SVD) such as the proper orthogonal decomposition (POD) [Everson and Sirovich, 1995] [Chatterjee, 2000] and the balanced truncation method [Moore, 1981] [Lall et al., 2002] introduce a projection onto dominant eigenspaces in the time domain. Moment-matching MOR methods, such as the Krylov subspace method [Boley, 1994] [Grimme, 1997] [Cullum and Zhang, 2002], provide an approximation of the transfer function of the discrete system in the frequency domain. The moment-matching methods require less numbers of operations than the SVD ones but do not preserve the stability of the system, which is a fundamental characteristic used in control theory.

Most of the applications and recent developments are done in the domain of circuit design, computational fluid dynamics, control design, and structural dynamics [Schilders et al., 2008]. While MOR methods are well developed for dynamic fields, repeated analysis of static problems such as singularity problems under various loading conditions leads to significant computation

efforts, and could benefit from the application of reduced techniques.

2.2.2 SVD-based MOR Methods

The SVD-based MOR methods rely on eigenvector analysis to provide an approximation of the original system. The reduced projection is constructed from eigenmodes obtained from collected samples of the solution, or input and output variables at different times.

A great number of these analyses are based on the POD method, first introduced by Kosambi [Kosambi, 1943] and further developed by Loève [Loève, 1945] in probability theory. The POD method determines the optimal lower rank approximation of a discrete system by constructing a projection onto its dominant states. For the reconstruction of partial image, Everson and Sirovich [Everson and Sirovich, 1995] proposed the snapshot POD method that constructs the subspace of the reduced model based on data collected by snapshots or samples of the solution. The SVD of the correlation matrix of the snapshots indicates the dominant POD modes that will be preserved during the reduction process. This technique has been introduced by Lumley [Lumley, 1967] for the study of turbulence and further explored in the field of fluid mechanics by Holmes et al. [Holmes et al., 1998]. It is widely applied to signal analysis, data compression and pattern recognition [Kirby and Sirovich, 1990], to extract principal features of a system from the collection of experimental data. The POD method has also been applied to the analysis of structural vibrations and micro-electromechanical systems (MEMS) [Hung and Senturia, 1999], to nonlinear ordinary differential equations (ODEs) [Rathinam and Petzold, 2003] and recently to damage mechanics problems [Kerfriden et al., 2012]. The method of snapshots requires further investigation. First the sampling of the snapshots is to be properly determined; otherwise the resulting reduced model might not reflect the essential behavior of the original model. The states and phenomena that are not represented by the set of snapshots cannot be represented by the reduced system; indeed the approximation constructed by the POD method may vary a lot depending on the given snapshots. Also, the number of POD modes to be chosen for the low rank approximation also strongly affects

the accuracy of the reduced model.

The balanced truncation method is another commonly used SVD-based MOR method, introduced by Willcox and Peraire [Willcox and Peraire, 2002] in the discipline of computational fluid dynamics. It does not use direct snapshots of the original solution of the system but rather identifies the interaction between input, state and output variables to generate relevant modes that are then used to construct the projection. The original system is transformed such that the truncated states truncated are the ones that are least influenced by the inputs and have also less influence on the outputs. The balanced truncation method retains only certain states in the representation of the original model and an error bound is available for the reduced approximation. The controllability and observability gramians of a system, that respectively identify the state the relationship between input to the state variables and state to the output variables are discretized using samples of input and corresponding output variables from numerical simulations. The balanced truncation method computes a balancing transformation of lower-rank empirical gramian matrices, which are constructed by the POD method of snapshots.

2.2.3 Moment-Matching MOR Methods

Moment matching methods are used in the context of MOR to compute a projection of the high-dimensional space onto a much smaller space while satisfying a moment matching condition in the frequency domain. The moment matching condition states that the Taylor expansions of the transfer functions of the original and the reduced systems are equals up to a certain order.

Under the framework of moment-matching MOR methods, Padé [Padé, 1899] introduced a function approximation, later called the Padé approximant. This approximant is constructed based on a ratio of two polynomials by matching the moments of the Taylor expansions of both the original and the approximated rational functions. The asymptotic waveform evaluation (AWE) method, developed by Pillage and Rohrer [Pillage and Rohrer, 1990] for circuit simulations, introduces the Padé approximation for the transfer function of the reduced system satisfying the moment match-

ing condition. The transfer function is defined as a ratio of the Laplace transform of the input over the Laplace transform of the output. The Padé approximation of the transfer function is constructed in a two-step process. The moments of the original system are first evaluated, and the numerator and denominator parameters of the reduced system are chosen so that the moments of the reduced-order system equal those of the original system. This method involves solving a linear system of equations involving Hankel matrix. Taking the inverse Laplace transform of the Padé approximant, the transfer function in time domain from the reduced solution is obtained and the reduced approximation can be deduced. However, solving for an explicit representation of the approximated transfer function of large-scale systems often exhibits numerical instabilities. To resolve this issue, techniques have been developed that provide a reduced model satisfying the moment-matching condition implicitly.

In the early 50's, Lanczos and Arnoldi algorithms were introduced to iterative methods for computing eigenvalues and eigenvectors. Lanczos [Lanczos, 1950] contributed to the computation of eigenvalues of symmetric matrices by providing a matrix reduction to tri-diagonal form. Arnoldi [Arnoldi, 1951] provided an algorithm to reduce non-symmetric matrices to an upper Hessenberg form. Both algorithms can be applied for MOR purposes. Gallivan et al. [Gallivan et al., 1994] proposed to satisfy the moment-matching condition using Lanczos algorithm without having to explicitly compute the moments. This method employs the Krylov subspace approach that was first introduced in the context of eigenvalue estimations. The Krylov methods are also very efficient as there is no need to computed the moments or evaluate the transfer function of the original model and do not encounter the same instability issues as AWE methods. The projection matrix is constructed from the original system matrices and can be directly used to express the reduced system. The moment matching condition can also be introduced for the Taylor expansion at multiple points by the multipoint moment matching MOR methods [Elfadel and Ling, 1997]. However as these methods are local in nature, and their global error bounds are difficult to derive. Recent studies have been conducted to preserve the stability and the passivity of the original system in the moment-matching methods.

The iterative Krylov methods encounter ill-conditioning type instability as the size of the reduced system increases. The round off error increases in the Gram-Schmidt procedure used for the construction of orthonormal basis vector but can be fixed by re-orthogonalization techniques. Feldmann and Freund [Feldmann and Freund, 1995] introduced the Padé via Lanczos (PVL) method, in the domain of circuit simulation. A Padé approximant is calculated by means of a two-sided Lanczos algorithm, which improves the efficiency and the stability of the procedure. The Lanczos and Arnoldi procedures were also improved by Lehoucq and Sorensen [Calvetti et al., 1994] [Lehoucq and Sorensen, 1996] by introducing an implicit restarting approach that enhances computational and data storage efficiency. Applications of Krylov methods to second order systems and nonlinear ODEs [Bai et al., 1999] [Bai and Su, 2005] [Salimbahrami and Lohmann, 2006] have also been examined in the past decade.

Chapter 3

Meshfree ISBFM Galerkin Formulation for Poisson Problems with Singularities

3.1 Preliminaries

In this chapter, the characteristics of Poisson problems with singularities are first introduced. The treatments of numerical methods by enrichment of near-tip asymptotic functions and the associated numerical integration of the singular enrichment functions in the Galerkin formulation are discussed. The resulting ISBFM Galerkin meshfree approximation serves as the full scale base model for the proposed MOR methods presented in Chapter 4.

3.1.1 Model Problem

We consider Poisson problems with singularities induced by the non-smooth boundary in the non-convex domain and the discontinuities in the boundary conditions. For demonstration purpose,

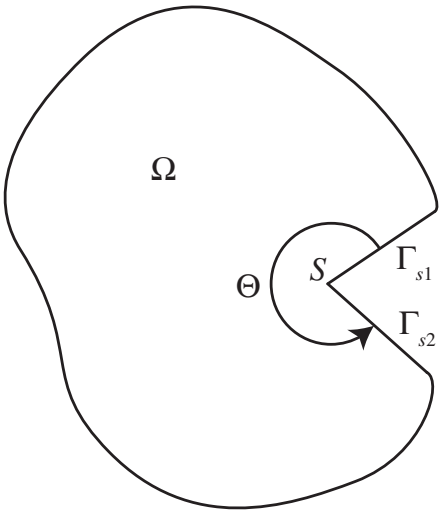

Figure 3.1: Model of general singularity problem

consider the following boundary value problem

$$\Delta u = 0 \quad \text{in } \Omega, \tag{3.1a}$$

$$u = g \quad \text{on } \Gamma_g, \tag{3.1b}$$

$$\boldsymbol{\nabla} u \cdot \boldsymbol{n} = h \quad \text{on } \Gamma_h \tag{3.1c}$$

where $\Delta = \boldsymbol{\nabla} \cdot \boldsymbol{\nabla}$, Ω is a bounded concave domain with boundary $\partial\Omega = \Gamma = \Gamma_g \cup \Gamma_h$, the vector $\boldsymbol{n}$ is the outward normal of $\partial\Omega$, and g and h are smooth functions.

In Figure 3.1, there is a singularity in the derivative of the solution at point S when $\Theta > \pi$. The order of singularity is also affected by the angle Θ as well as the type of boundary conditions on the two boundaries Γ_{s1} and Γ_{s2} connected to the point S and we denote $\Gamma_s = \Gamma_{s1} \cup \Gamma_{s2}$. Two combinations of boundary conditions on Γ_{s1} and Γ_{s2} are considered: pure Dirichlet (D-D) and mixed Neumann and Dirichlet (N-D) boundary conditions. The harmonic solution of problem in (3.1) can be derived by means of the method of separation of variable [Li et al., 2005], and they have been used as the enrichment functions in numerical solution of singularity problems.

For simplicity, we consider the case of homogeneous boundary conditions on the adjacent boundaries associated with the point S; i.e. $g = 0$ on $\Gamma_g \cup \Gamma_s$ and $h = 0$ on $\Gamma_h \cup \Gamma_s$. The

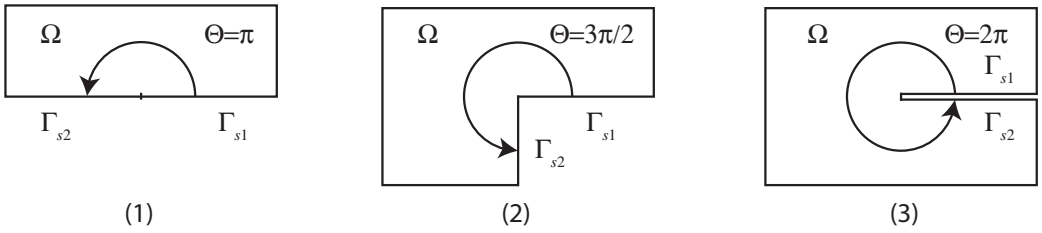

Figure 3.2: Different types of geometric singularities

Table 3.1: Order of singularity for harmonic solutions of problems with D-D or N-D types of boundary conditions

	(1) $\Theta = \pi$	(2) $\Theta = \frac{3\pi}{2}$	(3) $\Theta = 2\pi$
D-D Type	$O(r)$	$O(r^{\frac{2}{3}})$	$O(r^{\frac{1}{2}})$
N-D Type	$O(r^{\frac{1}{2}})$	$O(r^{\frac{1}{3}})$	$O(r^{\frac{1}{4}})$

forms of the solution for different singularity problems, presented in Figure 3.2, are summarized in Table 3.1 below, wherein r is the distance between any point in the domain and the singularity point.

It can be observed from Table 3.1 that the strongest singularity occurred when angle $\Theta = 2\pi$ and N-D boundary conditions are imposed, which corresponds to the edge crack Poisson problem. In the L-shaped domain Poisson problem [Igarashi and Honma, 1996], with a concave angle $\Theta = 3/2\pi$, a singularity weaker than that in the edge crack Poisson problem is observed, with either D-D or N-D types of boundary conditions. Furthermore, the edge crack Poisson problem with D-D boundary conditions has the same order of singularity as its equivalent symmetric problem [Lu et al., 2004] with $\Theta = \pi$, and subjected to N-D boundary conditions. The edge crack and L-shaped domain Poisson problems are commonly selected as model problems to show the effectiveness of numerical methods [Li et al., 2008]. In Chapter 4, we choose L-shaped domain and edge crack Poisson problems as models to test our proposed MOR approaches.

Since the solution of problem in (3.1) has the asymptotic behavior $u = O\left(r^{\alpha}\right)$, where $0 < \alpha \leq$

1, the convergence rate of the numerical solution is reduced when standard meshbased or meshfree methods are used for the approximation. Increasing the order of the approximate solution does not help to enhance the convergence and additional techniques are needed to improve the effectiveness of the numerical solution. Those treatments of the numerical approximation, including the enrichment methods that will be used in our development, are described in the following section.

3.1.2 Numerical Treatments of Singularities

Different treatments of the numerical approximation, such as very high adaptive refinement near the singularity point or adding a similar singularity behavior to the approximation space by the means of enrichments, were investigated in order to improve the accuracy of the solution [Li and Lu, 2000]. In this work, the refinement techniques are avoided and instead, the approximation space is enriched by adding particular shape functions that represent the singularity behavior of the derivative of the solution [Fries and Belytschko, 2010]. Enrichment methods require a prior knowledge of the asymptotic expansion of the solution near the singularity,

$$u(\boldsymbol{x}) = \sum_{i=1}^{\infty} a_i F_i(\boldsymbol{x}), \quad \text{as } \boldsymbol{x} \to \boldsymbol{x}_s \tag{3.2}$$

where F_i are singular functions and $\boldsymbol{x}_s$ the coordinates of the singularity point. The singular functions, used as enrichments, are commonly obtained from the basis function of the analytical asymptotic solution near the singularity point. The corresponding enrichment functions for the singularity problems presented in Table 3.1 are given in Table 3.2 [Li et al., 2005].

In this work, global enrichments are employed, however this technique requires a special treatment of the boundary conditions away from the singularity. It is worth noting that whenever enrichment functions are used in the approximation, high order quadrature rules are needed for the integration cells near the singularity point, which lead to high computational costs. The Integrated Singular Basis Function Method (ISBFM) proposed by Georgiou et al. [Georgiou et al., 1997] [Olson et al., 1991] [Elliotis et al., 2005], is introduced to obtain a Galerkin formulation, in which

Table 3.2: Enrichments functions $F_i,\ i = 1, 2, \ldots$

	F_i	α_i
D-D Type	$r^{\alpha_i} \sin(\alpha_i \theta)$	$\frac{(i-1)\pi}{\Theta}$
N-D Type	$r^{\alpha_i} \cos(\alpha_i \theta)$	$\frac{(i-1/2)\pi}{\Theta}$

the enrichment basis functions do not need to be integrated on the domain and on boundaries near the singularity point. The detailed formulation of this ISBFM Galerkin formulation is given in the next section.

3.2 Integrated Singular Boundary Function Method (ISBFM)

In this section, the ISBFM Galerkin formulation modified with Nitsche's method for singularity problems as well as the enriched RK approximation will be introduced. The reproducing kernel approximation for the smooth part of the solution in singularity problems will also be reviewed. These basic formulations constitute the framework for the construction of the full model for the proposed reduced order formulation to be discussed in Chapter 4.

3.2.1 Background

ISBFM [Georgiou et al., 1996] was first introduced to embed the asymptotic solution of the Laplace equation, where the enrichment functions were selected from the leading terms of the singular local solutions of the problem, while the smooth part of the solution was approximated by standard FEM. In this approach, the selected enrichment functions satisfy the governing differential equation and the boundary conditions near the singularity points, the Galerkin formulation can be expressed such that the non-smooth approximation does not appear in integrals near the singularity. As such, high order integration of the domain integrals near the singularity points can be avoided to yield

improved solution accuracy.

3.2.2 ISBFM Galerkin Formulation

The functional associated with the model problem in (3.1) is

$$I = \frac{1}{2}\int_{\Omega} \boldsymbol{\nabla} u \cdot \boldsymbol{\nabla} u \, \mathrm{d}\Omega - \int_{\Gamma_h} uh \, \mathrm{d}\Gamma \tag{3.3}$$

where $u \in \mathrm{H}^{1+\alpha}(\Omega)$ to account for the singularity in the geometry. Let the approximation of u, denoted as u^h, be decomposed into a smooth part $\bar{u}^h$ and a non-smooth part $\hat{u}^h$ which is regarded as the enrichment of the standard smooth solution $\bar{u}^h$ as

$$u^h = \bar{u}^h + \hat{u}^h \tag{3.4}$$

Here, a RK approximation, detailed in Chapter 2, is considered for the smooth solution, while the local asymptotic functions given in Section 3.1.2 are employed for the singular part of the solution and these will be discussed further in Section 3.2.3.

The functional (3.3) is modified for imposition of the essential boundary condition on Γ_g using Nitsche's method [Nitsche, 1971] [Fernández-Méndez and Huerta, 2004], it becomes

$$\begin{aligned} I = &\frac{1}{2}\int_{\Omega} \boldsymbol{\nabla}(\bar{u}^h + \hat{u}^h) \cdot \boldsymbol{\nabla}(\bar{u}^h + \hat{u}^h) \, \mathrm{d}\Omega - \int_{\Gamma_h} (\bar{u}^h + \hat{u}^h) h \, \mathrm{d}\Gamma \\ &- \int_{\Gamma_g} \boldsymbol{\nabla}(\bar{u}^h + \hat{u}^h) \cdot \boldsymbol{n}(\bar{u}^h + \hat{u}^h - g) \, \mathrm{d}\Gamma + \frac{\beta}{2}\int_{\Gamma_g} (\bar{u}^h + \hat{u}^h - g)(\bar{u}^h + \hat{u}^h - g) \, \mathrm{d}\Gamma \end{aligned} \tag{3.5}$$

Compared to (3.3), the additional integrals corresponding to boundary integrals on Γ_g are due to Nitsche's formulation for enforcement of essential boundary conditions, and β is a penalty parameter. Minimizing the functional (3.5) leads to a standard Galerkin formulation associated

with the smooth and non-smooth approximations as follows

$$\begin{aligned}
&\int_{\Omega} \boldsymbol{\nabla}\delta\bar{u}^h \cdot \boldsymbol{\nabla}(\bar{u}^h + \hat{u}^h)\ \mathrm{d}\Omega \\
&- \int_{\Gamma_g} \left(\delta\bar{u}^h \left(\boldsymbol{\nabla}(\bar{u}^h + \hat{u}^h) \cdot \boldsymbol{n} - \beta\left(\bar{u}^h + \hat{u}^h\right)\right) + \boldsymbol{\nabla}\delta\bar{u}^h \cdot \boldsymbol{n}\left(\bar{u}^h + \hat{u}^h\right)\right)\ \mathrm{d}\Gamma \\
&= \int_{\Gamma_h} \delta\bar{u}^h h\ \mathrm{d}\Gamma - \int_{\Gamma_g} \left(-\delta\bar{u}^h \beta g + \boldsymbol{\nabla}\delta\bar{u}^h \cdot \boldsymbol{n} g\right)\ \mathrm{d}\Gamma
\end{aligned} \tag{3.6a}$$

$$\begin{aligned}
&\int_{\Omega} \boldsymbol{\nabla}\delta\hat{u}^h \cdot \boldsymbol{\nabla}(\bar{u}^h + \hat{u}^h)\ \mathrm{d}\Omega \\
&- \int_{\Gamma_g} \left(\delta\hat{u}^h \left(\boldsymbol{\nabla}(\bar{u}^h + \hat{u}^h) \cdot \boldsymbol{n} - \beta\left(\bar{u}^h + \hat{u}^h\right)\right) + \boldsymbol{\nabla}\delta\hat{u}^h \cdot \boldsymbol{n}\left(\bar{u}^h + \hat{u}^h\right)\right)\ \mathrm{d}\Gamma \\
&= \int_{\Gamma_h} \delta\hat{u}^h h\ \mathrm{d}\Gamma - \int_{\Gamma_g} \left(-\delta\hat{u}^h \beta g + \boldsymbol{\nabla}\delta\hat{u}^h \cdot \boldsymbol{n} g\right)\ \mathrm{d}\Gamma
\end{aligned} \tag{3.6b}$$

If the basis functions for the non-smooth part of the solution $\hat{u}^h$ are harmonic, i.e. $\Delta\hat{u}^h = 0$, the domain integral involving $\hat{u}^h$ can be expressed as a boundary integral by applying the integration by parts method, which reduces as follow

$$\int_{\Omega} \boldsymbol{\nabla} v \cdot \boldsymbol{\nabla}\hat{u}^h\ \mathrm{d}\Omega = \int_{\Gamma} v \boldsymbol{\nabla}\hat{u}^h \cdot \boldsymbol{n}\ \mathrm{d}\Gamma, \quad \forall v \in V \tag{3.7}$$

Consequently, equations (3.6a) and (3.6b) become

$$\begin{aligned}
&\int_{\Omega} \boldsymbol{\nabla}\delta\bar{u}^h \cdot \boldsymbol{\nabla}\bar{u}^h\ \mathrm{d}\Omega + \int_{\Gamma} \delta\bar{u}^h \boldsymbol{\nabla}\hat{u}^h \cdot \boldsymbol{n}\ \mathrm{d}\Gamma \\
&- \int_{\Gamma_g} \left(\delta\bar{u}^h \left(\boldsymbol{\nabla}(\bar{u}^h + \hat{u}^h) \cdot \boldsymbol{n} - \beta\left(\bar{u}^h + \hat{u}^h\right)\right) + \boldsymbol{\nabla}\delta\bar{u}^h \cdot \boldsymbol{n}\left(\bar{u}^h + \hat{u}^h\right)\right)\ \mathrm{d}\Gamma \\
&= \int_{\Gamma_h} \delta\bar{u}^h h\ \mathrm{d}\Gamma - \int_{\Gamma_g} \left(-\delta\bar{u}^h \beta g + \boldsymbol{\nabla}\delta\bar{u}^h \cdot \boldsymbol{n} g\right)\ \mathrm{d}\Gamma
\end{aligned} \tag{3.8a}$$

$$\begin{aligned}
&\int_{\Omega} \boldsymbol{\nabla}\delta\hat{u}^h \cdot \boldsymbol{\nabla}\bar{u}^h\ \mathrm{d}\Omega + \int_{\Gamma} \delta\hat{u}^h \boldsymbol{\nabla}\hat{u}^h \cdot \boldsymbol{n}\ \mathrm{d}\Gamma \\
&- \int_{\Gamma_g} \left(\delta\hat{u}^h \left(\boldsymbol{\nabla}(\bar{u}^h + \hat{u}^h) \cdot \boldsymbol{n} - \beta\left(\bar{u}^h + \hat{u}^h\right)\right) + \boldsymbol{\nabla}\delta\hat{u}^h \cdot \boldsymbol{n}\left(\bar{u}^h + \hat{u}^h\right)\right)\ \mathrm{d}\Gamma \\
&= \int_{\Gamma_h} \delta\hat{u}^h h\ \mathrm{d}\Gamma - \int_{\Gamma_g} \left(-\delta\hat{u}^h \beta g + \boldsymbol{\nabla}\delta\hat{u}^h \cdot \boldsymbol{n} g\right)\ \mathrm{d}\Gamma
\end{aligned} \tag{3.8b}$$

The requirement of harmonic property in the enrichment bases in $\hat{u}^h$ allows the replacement of the domain integral by a boundary integral in (3.8b). With the consideration of taking the leading terms of the asymptotic solution as the enrichment basis functions for $\hat{u}^h$, it enables both trial and test functions of the enriched non-smooth part of the numerical solution to satisfy the homogeneous boundary conditions on Γ_s. Define $\bar{\Gamma}_h = \Gamma_h \setminus \Gamma_s$ and $\bar{\Gamma}_g = \Gamma_g \setminus \Gamma_s$, the ISBFM Galerkin formulation (3.8) can be expressed as follows

$$\begin{aligned}
&\int_\Omega \boldsymbol{\nabla}\delta\bar{u}^h \cdot \boldsymbol{\nabla}\bar{u}^h \,\mathrm{d}\Omega - \int_{\Gamma_g} \left(\delta\bar{u}^h \left(\boldsymbol{\nabla}\bar{u}^h \cdot \boldsymbol{n} - \beta\bar{u}^h\right) + \boldsymbol{\nabla}\delta\bar{u}^h \cdot \boldsymbol{n}\bar{u}^h\right) \,\mathrm{d}\Gamma \\
&+ \int_{\bar{\Gamma}_h} \delta\bar{u}^h \boldsymbol{\nabla}\hat{u}^h \cdot \boldsymbol{n} \,\mathrm{d}\Gamma - \int_{\bar{\Gamma}_g} \left(-\delta\bar{u}^h \beta\hat{u}^h + \boldsymbol{\nabla}\delta\bar{u}^h \cdot \boldsymbol{n}\hat{u}^h\right) \,\mathrm{d}\Gamma \\
&= \int_{\bar{\Gamma}_h} \delta\bar{u}^h h \,\mathrm{d}\Gamma - \int_{\bar{\Gamma}_g} \left(-\delta\bar{u}^h \beta g + \boldsymbol{\nabla}\delta\bar{u}^h \cdot \boldsymbol{n}g\right) \,\mathrm{d}\Gamma
\end{aligned} \tag{3.9a}$$

$$\begin{aligned}
&\int_{\bar{\Gamma}_h} \boldsymbol{\nabla}\delta\hat{u}^h \cdot \boldsymbol{n}\bar{u}^h \,\mathrm{d}\Gamma - \int_{\bar{\Gamma}_g} \delta\hat{u}^h \left(\boldsymbol{\nabla}\bar{u}^h \cdot \boldsymbol{n} - \beta\bar{u}^h\right) \,\mathrm{d}\Gamma \\
&+ \int_{\bar{\Gamma}_h} \delta\hat{u}^h \boldsymbol{\nabla}\hat{u}^h \cdot \boldsymbol{n} \,\mathrm{d}\Gamma - \int_{\bar{\Gamma}_g} \left(-\delta\hat{u}^h \beta\hat{u}^h + \boldsymbol{\nabla}\delta\hat{u}^h \cdot \boldsymbol{n}\hat{u}^h\right) \,\mathrm{d}\Gamma \\
&= \int_{\bar{\Gamma}_h} \delta\hat{u}^h h \,\mathrm{d}\Gamma - \int_{\bar{\Gamma}_g} \left(-\delta\hat{u}^h \beta g + \boldsymbol{\nabla}\delta\hat{u}^h \cdot \boldsymbol{n}g\right) \,\mathrm{d}\Gamma
\end{aligned} \tag{3.9b}$$

In the above, the enrichment function $\hat{u}^h$ only appears on boundaries, which are away from the singularity point S where the bases functions for $\hat{u}^h$ can be smooth as will be discussed in the next sub-section. As such, the ISBFM Galerkin formulation in (3.9) can be numerically integrated using lower order quadrature than compared to a standard Galerkin formulation in (3.6). A comparison of the standard and ISBFM Galerkin formulations using different order of Gaussian quadrature rules will be presented in Section 3.3.

Remark 3.1. *The ISBFM Galerkin formulation can be obtained if the enrichment basis functions based on the local expansion bases of the solution can be derived. Those bases allow the simplification of some integral terms after integration by parts in the weak formulation.*

Remark 3.2. *Compared to a standard Galerkin formulation, the domain integral and the bound-*

ary integrals near the singularity point in the ISBFM formulation only contain the smooth approximation and can be numerically calculated with a significantly lower order quadrature rule for desired accuracy. Under the ISBFM formulation, the enrichment basis functions for $\hat{u}^h$ appear in boundary integrals away from the singularity point where those bases are much smoother, thus the quadrature order for the numerical integration of those terms can also be reduced.

3.2.3 Discretization of ISBFM Galerkin Formulation

Smooth approximation functions are unable to recover the solution of a singularity problem without special treatments, as described in the previous chapter, and adaptive refinement of the node distribution in the vicinity of a singularity can be very computationally expensive. For computational efficiency, enrichment functions may be added to the approximation based on the known local singular behavior, such as those derived from asymptotic expansion.

The RK approximation, presented in details in Chapter 2, is used as the approximation of the smooth part of the solution $\bar{u}^h$ in (3.4). The RK approximation of a function $\bar{u}$, denoted as $\bar{u}^h$, is expressed in (3.10) as a linear combination of $\bar{N}$ RK shape functions Ψ_i as follows

$$\bar{u}^h(\boldsymbol{x}) = \sum_{i=1}^{\bar{N}} \Psi_i(\boldsymbol{x})\bar{d}_i = \boldsymbol{\Psi}^{\mathrm{T}}(\boldsymbol{x})\bar{\boldsymbol{d}} \tag{3.10}$$

where $\bar{\boldsymbol{d}} \in \mathbb{R}^{\bar{N}\times 1}$ is the coefficient vector for the smooth part.

The approximation of the non-smooth part of the solution $\hat{u}^h$ in (3.4) is constructed by a linear combination of enrichment functions $\boldsymbol{F}$ as follows

$$\hat{u}^h(\boldsymbol{x}) = \sum_{i=1}^{\hat{N}} F_i(\boldsymbol{x})\hat{d}_i = \boldsymbol{F}^{\mathrm{T}}(\boldsymbol{x})\hat{\boldsymbol{d}} \tag{3.11}$$

where $\hat{N}$ is the number of enrichment functions F_i as discussed in Section 3.1.2 and $\hat{\boldsymbol{d}} \in \mathbb{R}^{\hat{N}\times 1}$ is the coefficient vector for the non-smooth part.

The discretization of ISBFM Galerkin formulation defined in (3.9) can be written in a matrix

form as follows

$$\boldsymbol{K}\boldsymbol{d} = \begin{bmatrix} \bar{\boldsymbol{K}} & \hat{\boldsymbol{K}} \\ \hat{\boldsymbol{K}}^{\mathrm{T}} & \hat{\boldsymbol{K}} \end{bmatrix} \begin{bmatrix} \bar{\boldsymbol{d}} \\ \hat{\boldsymbol{d}} \end{bmatrix} = \begin{bmatrix} \bar{\boldsymbol{f}} \\ \hat{\boldsymbol{f}} \end{bmatrix} = \boldsymbol{f} \tag{3.12}$$

The stiffness matrix $\boldsymbol{K} \in \mathbb{R}^{N \times N}$ is a positive definite matrix, where $N = \bar{N} + \hat{N}$. The sub-matrix $\bar{\boldsymbol{K}} \in \mathbb{R}^{\bar{N} \times \bar{N}}$ is a sparse matrix, $\hat{\boldsymbol{K}} \in \mathbb{R}^{\bar{N} \times \hat{N}}$ and $\hat{\boldsymbol{K}} \in \mathbb{R}^{\hat{N} \times \hat{N}}$ are the other sub-matrices from (3.9). The entries of those matrices are given by

$$\bar{K}_{ij} = \int_{\Omega} \boldsymbol{\nabla}\Psi_i \cdot \boldsymbol{\nabla}\Psi_j \, \mathrm{d}\Omega - \int_{\Gamma_g} \left(\Psi_i \boldsymbol{\nabla}\Psi_j \cdot \boldsymbol{n} + \boldsymbol{\nabla}\Psi_i \cdot \boldsymbol{n}\Psi_j\right) \, \mathrm{d}\Gamma + \beta \int_{\Gamma_g} \Psi_i \Psi_j \, \mathrm{d}\Gamma \tag{3.13}$$

$$\hat{K}_{ij} = \int_{\bar{\Gamma}_h} F_i \boldsymbol{\nabla} F_j \cdot \boldsymbol{n} \, \mathrm{d}\Gamma - \int_{\bar{\Gamma}_g} \boldsymbol{\nabla} F_i \cdot \boldsymbol{n} F_j \, \mathrm{d}\Gamma + \beta \int_{\bar{\Gamma}_g} F_i F_j \, \mathrm{d}\Gamma \tag{3.14}$$

and

$$\hat{K}_{ij} = \int_{\bar{\Gamma}_h} \Psi_i \boldsymbol{\nabla} F_j \cdot \boldsymbol{n} \, \mathrm{d}\Gamma - \int_{\bar{\Gamma}_g} \boldsymbol{\nabla}\Psi_i \cdot \boldsymbol{n} F_j \, \mathrm{d}\Gamma + \beta \int_{\bar{\Gamma}_g} \Psi_i F_j \, \mathrm{d}\Gamma \tag{3.15}$$

The right hand side vector $\boldsymbol{f} \in \mathbb{R}^{N \times 1}$ in (3.12) consists of two sub-vectors $\bar{\boldsymbol{f}} \in \mathbb{R}^{\bar{N} \times 1}$ and $\hat{\boldsymbol{f}} \in \mathbb{R}^{\hat{N} \times 1}$ defined as

$$\bar{f}_i = \int_{\bar{\Gamma}_h} \Psi_i h \, \mathrm{d}\Gamma - \int_{\bar{\Gamma}_g} \left(-\Psi_i \beta g + \boldsymbol{\nabla}\Psi_i \cdot \boldsymbol{n} g\right) \mathrm{d}\Gamma \tag{3.16}$$

$$\hat{f}_i = \int_{\bar{\Gamma}_h} F_i h \, \mathrm{d}\Gamma - \int_{\bar{\Gamma}_g} \left(-F_i \beta g + \boldsymbol{\nabla} F_i \cdot \boldsymbol{n} g\right) \mathrm{d}\Gamma \tag{3.17}$$

The discrete equation of ISBFM Galerkin formulation will be used to construct the MOR models in Chapter 4.

3.3 Numerical Example

The effectiveness of the ISBFM Galerkin method compared to a standard Galerkin method is tested numerically for problem with singularity. In the following study, RK functions with linear basis and cubic B-spline kernel function with a normalized support size of $a = 1.51$ are chosen for the smooth part of the solution. The enrichment functions described in Section 3.1.2 are employed to

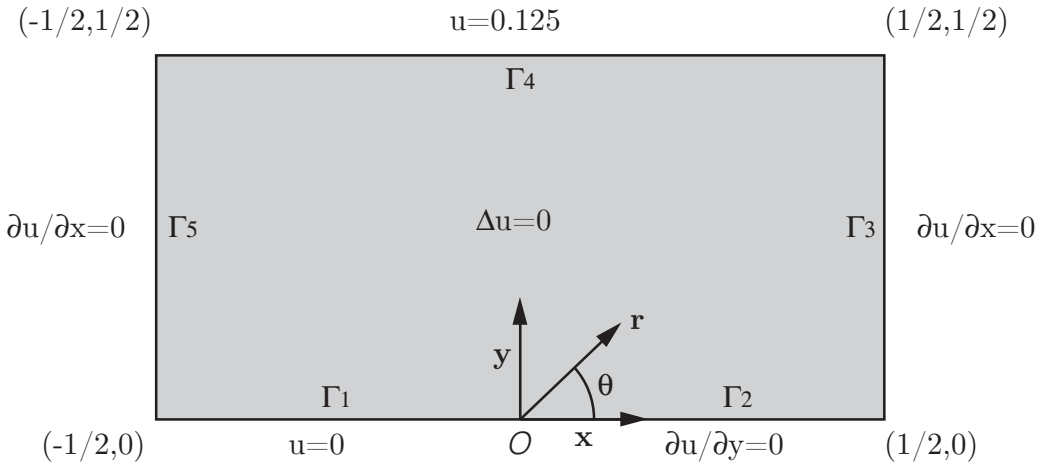

Figure 3.3: Model of cracked beam Poisson problem

represent the singularities in the solution. For Nitsche's treatment of essential boundary conditions, $\beta = 100/h$ is adopted, where h is the minimal spacing of the RK nodes.

To compare the approximated solutions obtained from standard Galerkin and ISBFM Galerkin formulations, we study a two-dimensional cracked beam Poisson problem as shown in Figure 3.3 in which the discontinuity of boundary conditions at $(0, 0)$ yields a singularity of order $\alpha = 1/2$, according to Table 3.1.

The problem statement of the cracked beam Poissonproblem is given as

$$\Delta u = 0 \quad \text{in } \Omega, \tag{3.18a}$$

subjected to the boundary conditions,

$$u|_{y=0,-1/2\leq x\leq 0} = 0, u|_{y=1/2,-1/2\leq x\leq 1/2} = 0.125, \tag{3.18b}$$

$$\frac{\partial u}{\partial y}|_{y=0,0\leq x\leq 1/2} = 0, \frac{\partial u}{\partial x}|_{x=1/2,0\leq y\leq 1/2} = 0, \frac{\partial u}{\partial x}|_{x=-1/2,0\leq y\leq 1/2} = 0 \tag{3.18c}$$

where $\Omega = [-1/2, 1/2] \times [0, 1/2]$. The singular basis functions of this problem are chosen from

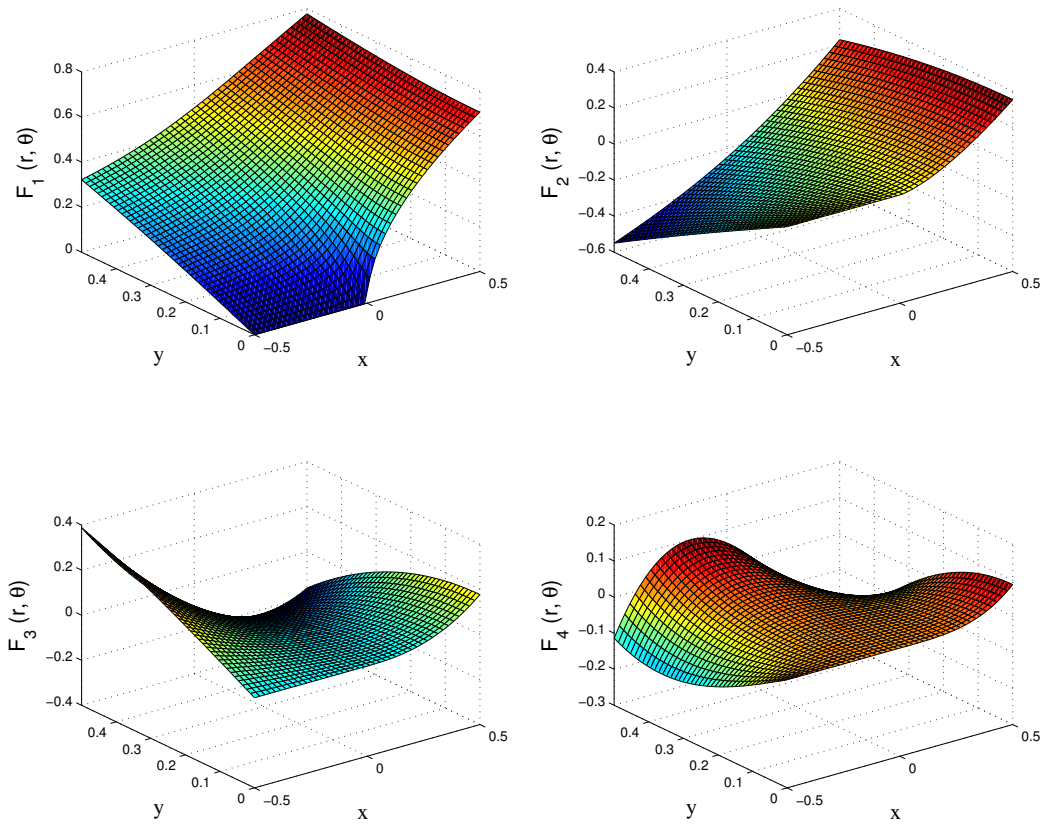

Figure 3.4: Cracked beam Poisson problem's enrichment functions F_i for $i = 1, 2, 3, 4$

the harmonic functions [Li et al., 2005]

$$F_i(r,\theta) = r^{\frac{2i-1}{2}} \cos\left(\frac{2i-1}{2}\theta\right), \quad i = 1, 2, \ldots \tag{3.19}$$

where $r = \sqrt{(x-x_0)^2 + (y-y_0)^2}$ and $\theta = \tan^{-1}\left((y-y_0)/(x-x_0)\right)$, which also satisfy the homogeneous essential and natural boundary conditions on Γ_1 and Γ_2 adjacent to the singularity point (x_0, y_0), respectively, see Figure 3.4.

For assessment of convergence, the relative errors in L^2 and H^1 norms are considered as follows

$$e_0 = \frac{\left\|u - u^h\right\|_{L^2}}{\|u\|_{L^2}}, \quad e_1 = \frac{\left\|u - u^h\right\|_{H^1}}{\|u\|_{H^1}} \tag{3.20}$$

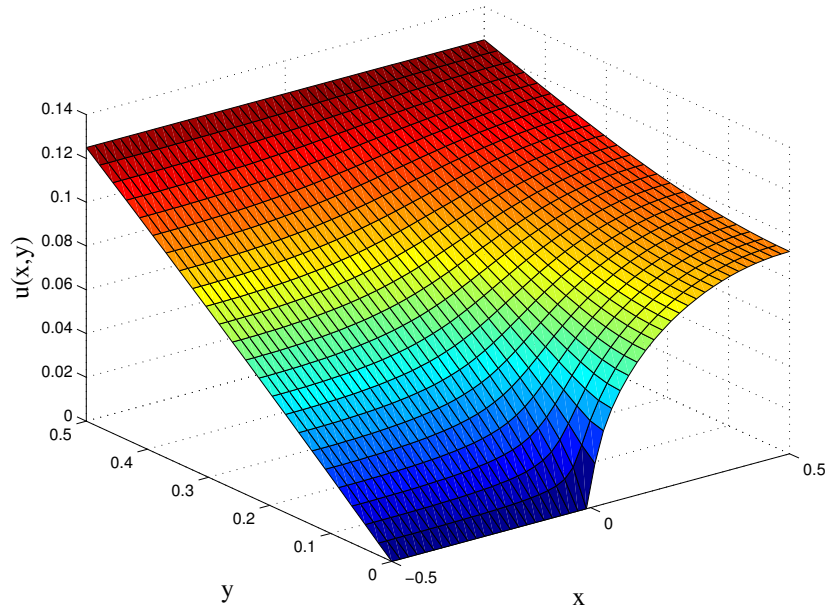

Figure 3.5: Exact solution of cracked beam Poisson problem

The exact solution u of the cracked beam Poisson problem is presented in Figure 3.5.

The solutions of standard Galerkin and ISBFM Galerkin formulations obtained by using a 48×24 uniform discretization with one enrichment function ($\hat{N} = 1$) are shown in Figure 3.6 and Figure 3.7, where different orders of Gaussian quadrature for the domain and boundary integrals have been used. The results indicate that, for the same Gaussian quadrature, the solution from ISBFM Galerkin formulation provides better accuracy in both L^2 and H^1 norms. The distributions of the absolute errors of solutions in the domain are compared in Figure 3.8 where an 8th order of Gaussian quadrature has been used in the Galerkin equations to properly integrate the singular functions. The error from the standard Galerkin formulation is localized around the singularity point and is much larger than the error from ISBFM Galerkin method.

The convergence plots of standard and ISBFM Galerkin formulations in relative L^2 error norm are shown in Figure 3.9 using different numbers of Gauss points (GP). The asymptotic rates of convergence of the approximation are presented in Table 3.3. The ISBFM Galerkin formulation improves the accuracy of the approximation and also its rate of convergence.

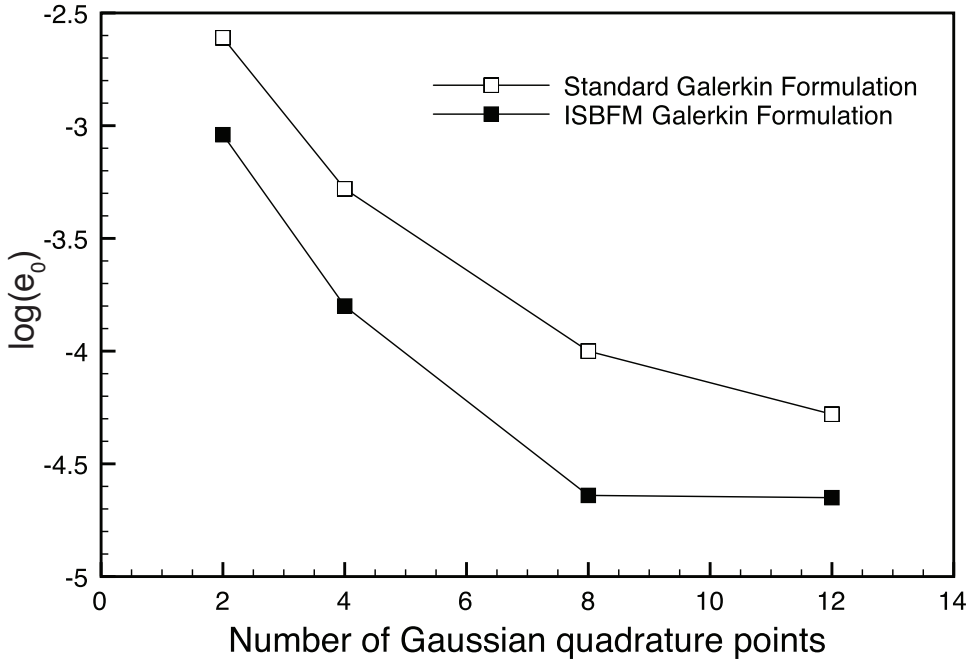

Figure 3.6: Relative error in L^2 norm of approximations of cracked beam Poisson problem under different Galerkin formulations and different orders of Gaussian quadrature

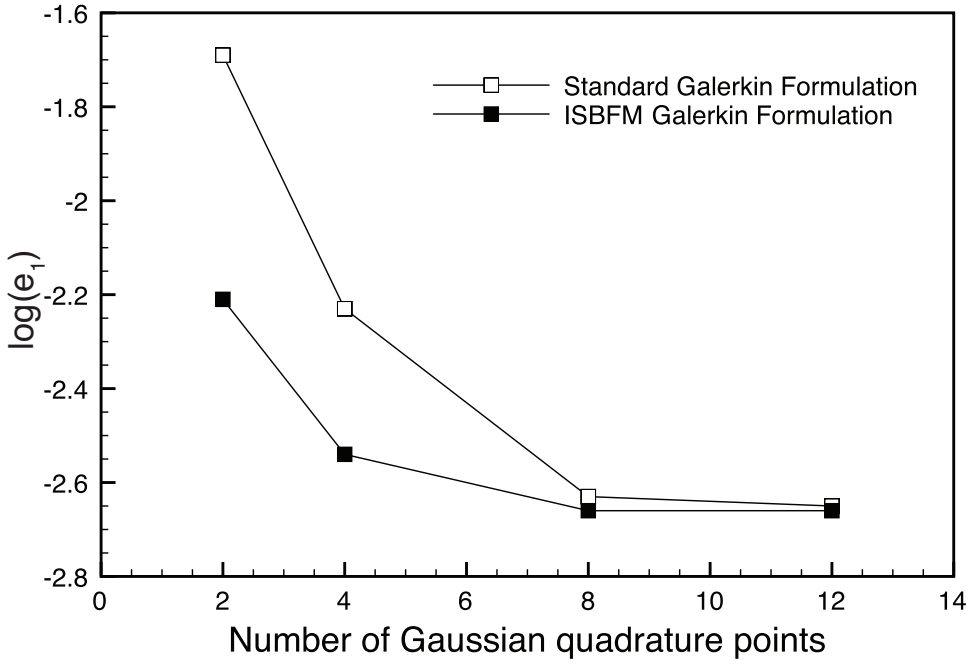

Figure 3.7: Relative error in H^1 norm of approximations of cracked beam Poisson problem under different Galerkin formulations and different orders of Gaussian quadrature

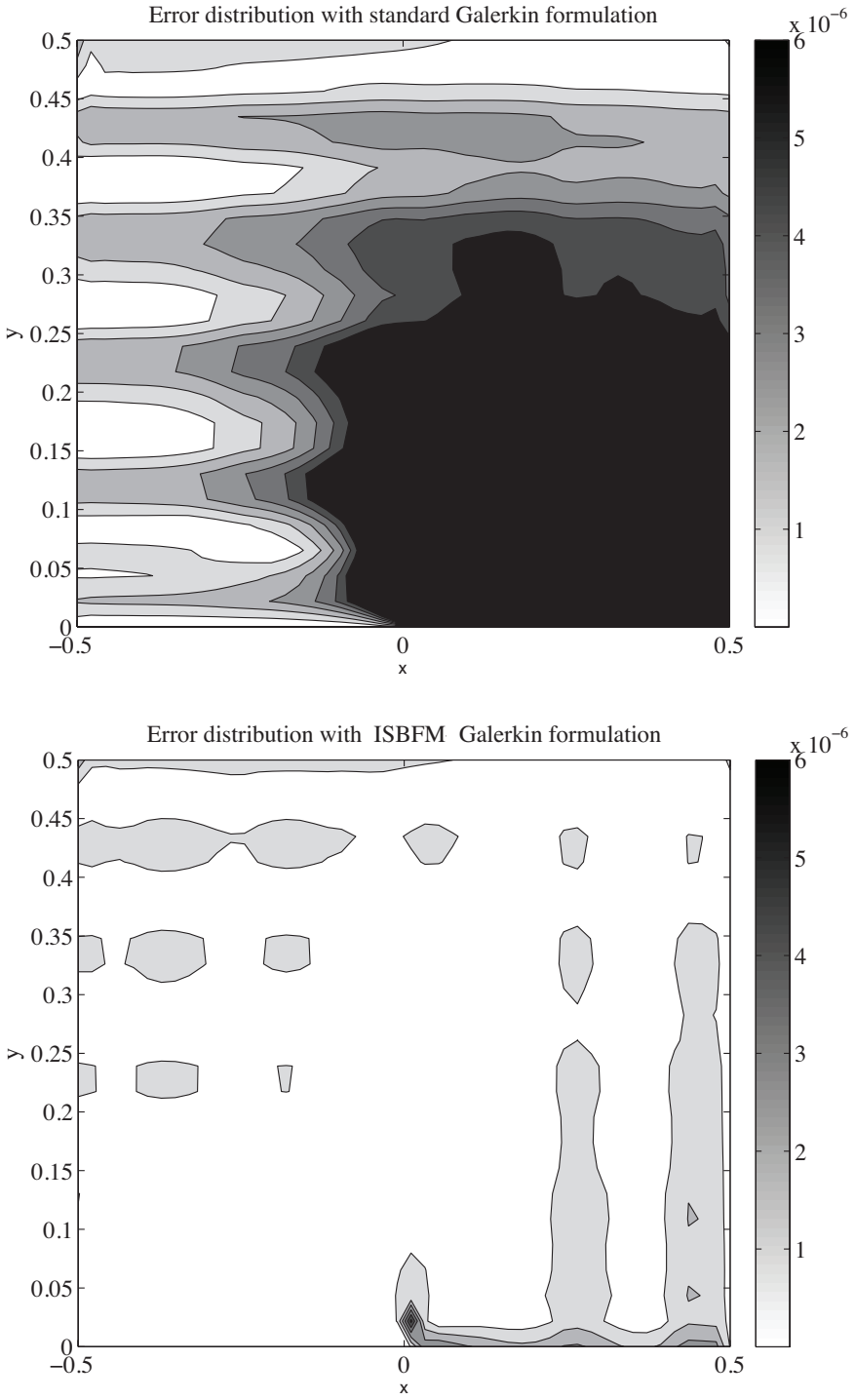

Figure 3.8: Absolute error distribution of solutions from standard and ISBFM Galerkin formulations

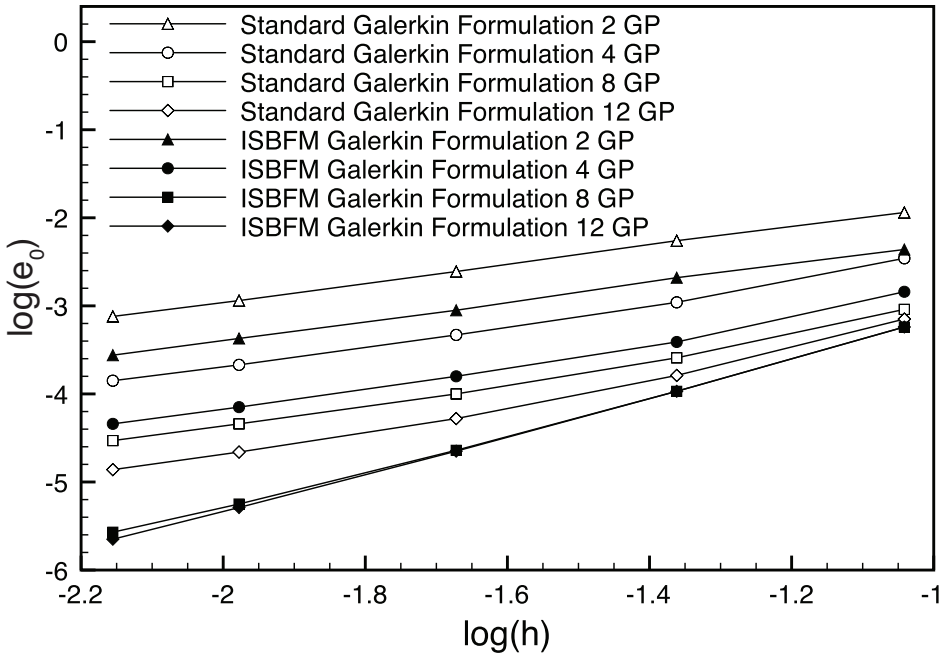

Figure 3.9: Convergence plot in relative L^2 error norm of standard and ISBFM Galerkin formulations with different orders of Gaussian quadrature

Table 3.3: Rate of Convergence in L^2 norm of standard and ISBFM Galerkin formulations with different orders of Gaussian quadrature

	Standard Galerkin				ISBFM Galerkin			
Orders of Gaussian Quadrature	2	4	8	12	2	4	8	12
Rate of Convergence	1.03	1.05	1.06	1.12	1.04	1.08	1.80	2.04

This cracked beam Poisson problem example demonstrates that ISBFM Galerkin method provides a more accurate approximation compared to the standard Galerkin method, and allows using lower order Gaussian quadrature for problems with singularity. The approximated solution from ISBFM Galerkin method is also better suited to the proposed MOR approaches, as the singularity behavior is better preserved than that of a standard Galerkin formulation in the reduced order space.

Chapter 4

ISFBM Galerkin based MOR Method for Poisson Problems with Singularities

4.1 Preliminaries

Two reduced order methods for Poisson problems with singularities are introduced in this chapter. The MOR methods are constructed for their application to the fine scale solution obtained from the ISBFM Galerkin formulation presented in Chapter 3. The following section will first introduce the SVD based MOR method, which is the starting point of the proposed MOR approaches. The reduced approximation methods are based on truncation of natural modes of the system and will be described in detail in the remaining. The efficiency of the MOR methods is discussed in the numerical examples presented at the end of this chapter.

4.1.1 Background

The SVD based MOR methods are methods based on eigenvector analysis. The POD method identifies the correlation between the vectors of a given set of sampled solutions and provides the modes, called POD modes, that represents this set of samples the best. The reduced approximation is obtained from the linear combination of truncated POD modes. For MOR, the POD method

usually constructs the reduced projection from POD modes based on collected snapshots of the full solution at certain times.

The POD method is based on the assumption that there is a correlation between successive snapshots of the original state vector; also one needs to select the snapshots in an appropriate way to ensure a relevant approximation of the original system. For elliptic problem, the snapshots can be replaced by eigenmodes of the system for the MOR by POD. After describing the SVD decomposition and the POD method based on snapshots of the solution, a POD method that considers eigenvectors of the stiffness matrix instead of snapshots is presented and serves as the starting point for deriving the uniform and the decomposed reduction methods presented in Section 4.2.

4.1.2 Singular Value Decomposition

In linear algebra, different techniques have been developed for matrix decomposition [Golub and van Van Loan, 1996] [Horn and Johnson, 2012]. SVD is a matrix diagonalization technique that has been employed in various MOR methods to separate the dominant modes of a system from the less important ones. The SVD of a matrix $\boldsymbol{A} \in \mathbb{R}^{M\times N}$ of rank r is defined as follow

$$\begin{gathered} \forall \boldsymbol{A} \in \mathbb{R}^{M\times N}, \text{rank}(\boldsymbol{A}) = r \leq M \leq N \\ \exists (\boldsymbol{U}, \boldsymbol{V}, \boldsymbol{\Sigma}) \in \mathbb{R}^{M\times M} \times \mathbb{R}^{N\times N} \times \mathbb{R}^{M\times N} \text{ such that } \boldsymbol{A} = \boldsymbol{U}\boldsymbol{\Sigma}\boldsymbol{V}^{\mathrm{T}} \end{gathered} \tag{4.1}$$

where $\boldsymbol{U} \in \mathbb{R}^{M\times M}$ and $\boldsymbol{V} \in \mathbb{R}^{N\times N}$ are orthogonal matrices that represent respectively the left and right singular matrices of $\boldsymbol{A}$. $\boldsymbol{\Sigma} = \text{diag}(\sigma_1 \dots \sigma_N) \in \mathbb{R}^{M\times N}$ is a pseudo diagonal matrix, composed of the singular values $\sigma_1 \geq \sigma_i \geq \sigma_N \geq 0$ of the matrix $\boldsymbol{A}$. The singular values of $\boldsymbol{A}$ are defined as $\sigma_i = \sqrt{\lambda_i}$, where λ_i are the eigenvalues of $\boldsymbol{A}\boldsymbol{A}^{\mathrm{T}}$, which are also the eigenvalues of $\boldsymbol{A}^{\mathrm{T}}\boldsymbol{A}$. If the rank of $\boldsymbol{A}$ is $r \leq M \leq N$, then the Hankel singular value $\sigma_i = 0$ for $i > r$. The columns of $\boldsymbol{U}$ and $\boldsymbol{V}$ are called respectively the left and right singular vectors of $\boldsymbol{A}$, and are respectively the orthonormal eigenvectors of $\boldsymbol{A}\boldsymbol{A}^{\mathrm{T}}$ and $\boldsymbol{A}^{\mathrm{T}}\boldsymbol{A}$. The SVD is unique when the matrix $\boldsymbol{A}$ is square.

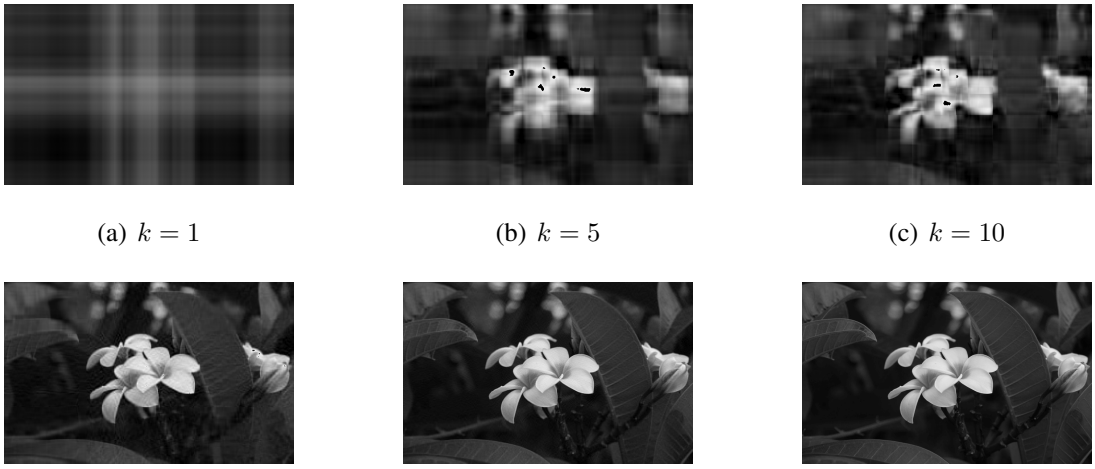

(a) $k = 1$ (b) $k = 5$ (c) $k = 10$

(d) $k = 40$ (e) $k = 100$ (f) Original

Figure 4.1: SVD decomposition of an image

The theorem of Schmidt-Mirsky states that

$$\begin{aligned} &\forall \boldsymbol{A} \in \mathbb{R}^{M\times N}, \text{rank}(\boldsymbol{A}) = r \leq M \leq N, \\ &\exists \boldsymbol{A}_k \in \{\boldsymbol{X} \in \mathbb{R}^{M\times N}, \text{rank}(\boldsymbol{X}) = k \leq r\} \text{ such that} \\ &\|\boldsymbol{A} - \boldsymbol{A}_k\|_F = \min\{\|\boldsymbol{A} - \boldsymbol{X}\|_F : \text{rank}(\boldsymbol{X}) = k \leq r\} = \sigma_{k+1}(\boldsymbol{A}) \end{aligned} \tag{4.2}$$

This theorem provides the existence of an optimal minimizer of rank $k \leq r$ that can be expressed as $\boldsymbol{A}_k = \boldsymbol{U}\text{diag}(\sigma_1 \dots \sigma_k 0 \dots 0)\boldsymbol{V}^{\mathrm{T}}$ in the Frobenius norm. The Frobenius norm for a matrix $\boldsymbol{X} = (X_{ij})_{1<i<M,1<j<N}$ is defined as

$$\|\boldsymbol{X}\|_F = \sqrt{\sum_{i=1}^{M}\sum_{j=1}^{N} |X_{ij}|^2} \tag{4.3}$$

SVD method can be applied for image compression. An example is provided in Figure 4.1, where the corresponding original image 4.1(f) can be represented as a matrix of dimension 499×800 and rank $r = 499$, containing the intensity of each pixel. The SVD decomposition provides lower rank approximations of this matrix. We can observe how the image is compressed using different number k of singular values.

This optimal minimizer feature of the SVD is well designed for MOR as it provides a lower rank optimal approximation of a matrix. The idea of truncating the dominant states to obtain a lower rank matrix approximation is driving the MOR methods by POD.

4.1.3 Proper Orthogonal Decomposition MOR

The POD method is a least square type approximation method, and it constructs a set of basis vectors that represents the dominant characteristics of the system. The POD method constructs an optimal projection $\mathbf{\Pi}_k$ of a given set of data $\boldsymbol{x}(t) \in \mathbb{R}^N$, where $0 < t < T$, onto a subspace of dimension $k \ll N$. The orthogonal projection $\mathbf{\Pi}_k \in \mathbb{R}^{N\times N}$ of rank k is obtained by minimizing the error $\int_0^T \|\boldsymbol{x}(t) - \mathbf{\Pi}_k \boldsymbol{x}(t)\|^2 \, \mathrm{d}t$.

Snapshots obtained from experimental data have been used to compute the POD modes of the system, which span the subspace of the projection. Define a set of N_s snapshots of the solution at discrete times t_s of a system. This set $\boldsymbol{X} = \sqrt{1/N_s}\,(\boldsymbol{x}(t_1)\dots\boldsymbol{x}(t_{N_s})) \in \mathbb{R}^{N\times N_s}$ lies in a vector space V of dimension $N_s \ll N$. The orthogonal projection $\mathbf{\Pi}_k \in \mathbb{R}^{N\times N}$ of rank k onto a subspace V_k of dimension $k \ll N$ is obtained such that it minimizes the error

$$\frac{1}{N_s}\sum_{s=1}^{N_s} \|\boldsymbol{x}(t_s) - \mathbf{\Pi}_k \boldsymbol{x}(t_s)\|^2 \tag{4.4}$$

which is equivalent to finding a basis $\{\mathbf{\Phi}_i\}_{i=1}^k$ that solves

$$\min_{\{\mathbf{\Phi}_i\}_{i=1}^k} \sum_{s=1}^{N_s} \left\| \boldsymbol{x}(t_s) - \sum_{j=1}^{k} \langle \boldsymbol{x}(t_s), \mathbf{\Phi}_j\rangle \mathbf{\Phi}_j \right\|^2 \quad \text{subjected to } \langle \mathbf{\Phi}_i, \mathbf{\Phi}_j\rangle = \delta_{ij} \tag{4.5}$$

where $\langle\cdot,\cdot\rangle$ denotes the inner product in Euclidean space and $\|\cdot\| = \langle\cdot,\cdot\rangle^{1/2}$ is the corresponding norm. We have the following relation

$$\left\| \boldsymbol{x}(t_s) - \sum_{j=1}^{k} \langle \boldsymbol{x}(t_s), \boldsymbol{\Phi}_j \rangle \boldsymbol{\Phi}_j \right\|^2 = \langle \boldsymbol{x}(t_s), \boldsymbol{x}(t_s) \rangle - 2 \sum_{j=1}^{k} \langle \boldsymbol{x}(t_s), \boldsymbol{\Phi}_j \rangle \langle \boldsymbol{x}(t_s), \boldsymbol{\Phi}_j \rangle + \sum_{i=1}^{k} \sum_{j=1}^{k} \langle \boldsymbol{x}(t_s), \boldsymbol{\Phi}_i \rangle \langle \boldsymbol{x}(t_s), \boldsymbol{\Phi}_j \rangle \langle \boldsymbol{\Phi}_i, \boldsymbol{\Phi}_j \rangle \tag{4.6}$$

As $\langle \boldsymbol{\Phi}_i, \boldsymbol{\Phi}_j \rangle = \delta_{ij}$, we obtain

$$\begin{aligned} \left\| \boldsymbol{x}(t_s) - \sum_{j=1}^{k} \langle \boldsymbol{x}(t_s), \boldsymbol{\Phi}_j \rangle \boldsymbol{\Phi}_j \right\|^2 &= \|\boldsymbol{x}(t_s)\|^2 - 2 \sum_{j=1}^{k} |\langle \boldsymbol{x}(t_s), \boldsymbol{\Phi}_j \rangle|^2 + \sum_{j=1}^{k} |\langle \boldsymbol{x}(t_s), \boldsymbol{\Phi}_j \rangle|^2 \\ &= \|\boldsymbol{x}(t_s)\|^2 - \sum_{j=1}^{k} |\langle \boldsymbol{x}(t_s), \boldsymbol{\Phi}_j \rangle|^2 \end{aligned} \tag{4.7}$$

From (4.7) and as the basis vectors $\boldsymbol{\Phi}_j$ are orthonormal to each other, the minimization problem in (4.5) is equivalent to

$$\max_{\{\boldsymbol{\Phi}_i\}_{i=1}^{k}} \sum_{s=1}^{N_s} \sum_{j=1}^{k} |\langle \boldsymbol{x}(t_s), \boldsymbol{\Phi}_j \rangle|^2 \quad \text{subjected to } \langle \boldsymbol{\Phi}_i, \boldsymbol{\Phi}_j \rangle = \delta_{ij} \tag{4.8}$$

where $|\cdot|$ is the complex norm [Volkwein, 2001]. This optimization problem can be expressed as a constrained variational formulation. Using Lagrange multipliers λ_{ij} to impose the orthonormality of the basis vectors, the corresponding Lagrange function is

$$L[\{\boldsymbol{\Phi}_m\}_{m=1}^{k}, \{\lambda_{mn}\}_{m,n=1}^{k}] = \sum_{s=1}^{N_s} \sum_{j=1}^{k} |\langle \boldsymbol{x}(t_s), \boldsymbol{\Phi}_j \rangle|^2 - \sum_{i,j=1}^{k} \lambda_{ij} \left(\langle \boldsymbol{\Phi}_i, \boldsymbol{\Phi}_j \rangle - \delta_{ij} \right) \tag{4.9}$$

The stationary condition leads to the following conditions

$$\frac{\partial L}{\partial \boldsymbol{\Phi}_m} = 0 \Rightarrow 2 \sum_{s=1}^{N_s} \sum_{j=1}^{k} \langle \boldsymbol{x}(t_s), \boldsymbol{\Phi}_j \rangle \delta_{jm} \boldsymbol{x}(t_s) - \left(\sum_{j=1}^{k} \lambda_{ij} \delta_{im} \boldsymbol{\Phi}_j^{\mathrm{T}} + \sum_{i=1}^{k} \lambda_{ij} \delta_{jm} \boldsymbol{\Phi}_i^{\mathrm{T}} \right) = 0 \tag{4.10a}$$

$$\frac{\partial L}{\partial \lambda_{mn}} = 0 \Rightarrow \langle \boldsymbol{\Phi}_i, \boldsymbol{\Phi}_j \rangle = \delta_{ij} \tag{4.10b}$$

which can be further reduced to

$$\frac{\partial L}{\partial \boldsymbol{\Phi}_m} = 0 \Rightarrow 2\sum_{s=1}^{N_s} \langle \boldsymbol{x}(t_s), \boldsymbol{\Phi}_m \rangle \boldsymbol{x}(t_s) - \left(\sum_{j=1}^{k} \lambda_{mj} \boldsymbol{\Phi}_j^{\mathrm{T}} + \sum_{i=1}^{k} \lambda_{im} \boldsymbol{\Phi}_i^{\mathrm{T}} \right) = 0 \tag{4.11a}$$

$$\frac{\partial L}{\partial \lambda_{mn}} = 0 \Rightarrow \langle \boldsymbol{\Phi}_i, \boldsymbol{\Phi}_j \rangle = \delta_{ij} \tag{4.11b}$$

From (4.11a), it is shown by induction that $\lambda_{ij} = \lambda_{ii}\delta_{ij}$, which leads that the basis $\{\boldsymbol{\Phi}_i\}_{i=1}^{k}$ that solves (4.8) satisfies the following condition

$$\frac{\partial L}{\partial \boldsymbol{\Phi}_m} = 0 \Rightarrow \sum_{s=1}^{N_s} \boldsymbol{x}(t_s) \langle \boldsymbol{x}(t_s), \boldsymbol{\Phi}_m \rangle = \lambda_{mm} \boldsymbol{\Phi}_m^{\mathrm{T}} \tag{4.12a}$$

$$\frac{\partial L}{\partial \lambda_{mn}} = 0 \Rightarrow \langle \boldsymbol{\Phi}_i, \boldsymbol{\Phi}_j \rangle = \delta_{ij} \tag{4.12b}$$

In (4.12a), we can recognize that $\boldsymbol{\Phi}_m$ is an eigenvector of the autocorrelation matrix $\boldsymbol{R} \in \mathbb{R}^{N \times N}$ of rank $r \leq N$ of the data defined as

$$\boldsymbol{R} = \frac{1}{N_s} \sum_{s=1}^{N_s} \boldsymbol{x}(t_s) \boldsymbol{x}(t_s)^{\mathrm{T}} = \boldsymbol{X}\boldsymbol{X}^{\mathrm{T}} \tag{4.13}$$

The r orthonormal eigenvectors $\boldsymbol{\Phi}_i$ of $\boldsymbol{R}$ are called the POD modes and correspond to the left singular vectors obtained from the SVD of the snapshot matrix $\boldsymbol{X}$. The POD modes satisfy both conditions in (4.12). The proper selection of k POD modes will provide an optimal minimizer of (4.4).

Define $\boldsymbol{P}_k = [\boldsymbol{\Phi}_1 \boldsymbol{\Phi}_2 \dots \boldsymbol{\Phi}_k] \in \mathbb{R}^{N \times k}$ from the POD modes $\boldsymbol{\Phi}_i$ related to the k-th eigenvalues λ_i of $\boldsymbol{R}$ of largest magnitude. The error of the projection $\boldsymbol{\Pi}_k \in \mathbb{R}^{N \times N}$ of rank $k < r \leq N$ defined as

$$\boldsymbol{\Pi}_k = \sum_{i=1}^{k} \boldsymbol{\Phi}_i \boldsymbol{\Phi}_i^{\mathrm{T}} = \boldsymbol{P}_k \boldsymbol{P}_k^{\mathrm{T}} \tag{4.14}$$

is given as

$$\frac{1}{N_s} \sum_{s=1}^{N_s} \| \boldsymbol{x}(t_s) - \boldsymbol{\Pi}_k \boldsymbol{x}(t_s) \|^2 = \sum_{j=k+1}^{r} \lambda_j \tag{4.15}$$

As $\lambda_1 \geq \lambda_j \geq \lambda_r \geq 0$, this projection provides the optimal minimizer of the error [Lall et al., 2003].

4.1.4 Application to Linear Static System

Consider a discrete system

$$\boldsymbol{K}\boldsymbol{d} = \boldsymbol{f} \tag{4.16}$$

where $\boldsymbol{K} \in \mathbb{R}^{N\times N}$, $\boldsymbol{f} \in \mathbb{R}^{N\times 1}$ and $\boldsymbol{d} \in \mathbb{R}^{N\times 1}$. When solving a linear system in (4.16), the coefficient vector $\boldsymbol{d}$ can be expressed as a linear combination of eigenvectors of the flexibility matrix $\boldsymbol{K}^{-1}$. A reduced projection can be constructed from the dominant SVD modes of the flexibility matrix directly. Since $\boldsymbol{K}$ is symmetric positive definite, its SVD decomposition is equal to its eigendecomposition. It results that the dominant SVD modes are the eigenvectors corresponding to the largest singular values $\sigma_i = 1/\lambda_i$ of $\boldsymbol{K}^{-1}$, where $\lambda_1 \leq \lambda_i \leq \lambda_N$ are the eigenvalues of $\boldsymbol{K}$. The reduced approximations proposed in the following are based on truncation of SVD modes of the system for their application to elliptic problems with singularities.

4.2 Reduced Model

The full discrete system obtained from ISBFM Galerkin based enriched meshfree approximation for problems with singularities, as derived in Chapter 3, will be the base secrete system for MOR. Recall the discrete system (3.12) derived in Chapter 3 of dimension $N = \bar{N} + \hat{N}$ as

$$\boldsymbol{K}\boldsymbol{d} = \begin{bmatrix} \bar{\boldsymbol{K}} & \hat{\boldsymbol{K}} \\ \hat{\boldsymbol{K}}^{\mathrm{T}} & \hat{\boldsymbol{K}} \end{bmatrix} \begin{bmatrix} \bar{\boldsymbol{d}} \\ \hat{\boldsymbol{d}} \end{bmatrix} = \begin{bmatrix} \bar{\boldsymbol{f}} \\ \hat{\boldsymbol{f}} \end{bmatrix} = \boldsymbol{f} \tag{4.17}$$

The general form of a reduced order model of dimension $k \ll N$ is given by

$$\boldsymbol{K}^r\boldsymbol{d}^r = \boldsymbol{f}^r \tag{4.18}$$

where k is called the order of reduction, $\boldsymbol{K}^r \in \mathbb{R}^{k\times k}$ denotes the reduced stiffness matrix, $\boldsymbol{f}^r \in \mathbb{R}^{k\times 1}$ is the reduced force vector and $\boldsymbol{d}^r \in \mathbb{R}^{k\times 1}$ is the reduced coefficient vector. The reduced system is obtained from a projection of the full system. We denote the projection by $\boldsymbol{P} \in \mathbb{R}^{N\times k}$, whose columns are orthonormal vectors and the coefficient vector $\boldsymbol{d}$ in (4.17) is approximated by $\boldsymbol{P}\boldsymbol{d}^r$, i.e.,

$$\boldsymbol{d} \approx \boldsymbol{P}\boldsymbol{d}^r \tag{4.19}$$

We will study two ways of forming the projection matrix using modal analysis.

The first MOR method introduces a uniform reduction (UR) of the fine scale discrete system constructed from the ISBFM Galerkin formulation, termed ISBFM-UR, where the projection $\boldsymbol{P}$ is applied to all degrees of freedom consisting of the smooth and non-smooth parts of the solution. The reduced system is of the form

$$\boldsymbol{K}^{ur}\boldsymbol{d}^{ur} = \boldsymbol{f}^{ur}, \quad \boldsymbol{K}^{ur} = \boldsymbol{P}^T\boldsymbol{K}\boldsymbol{P}, \quad \boldsymbol{f}^{ur} = \boldsymbol{P}^T\boldsymbol{f} \tag{4.20}$$

where the superscript "ur" in (4.20) signifies the uniform reduction concept, $\boldsymbol{d}^{ur} \in \mathbb{R}^{k\times 1}$ is the reduced coefficient vector, $\boldsymbol{K}^{ur} \in \mathbb{R}^{k\times k}$ is the reduced stiffness matrix and $\boldsymbol{f}^{ur} \in \mathbb{R}^{k\times 1}$ is the reduced force vector. The projection matrix $\boldsymbol{P}$ is constructed from the eigenvectors $\{\boldsymbol{\phi}_i\}_{i=1}^k$ corresponding to the k smallest eigenvalues $\lambda_1 \leq \lambda_i \leq \lambda_k$ of $\boldsymbol{K}$, that is, $\boldsymbol{P} = [\boldsymbol{\phi}_1\boldsymbol{\phi}_2 \ldots \boldsymbol{\phi}_k]$. The component of the reduced order coefficient vector is $d_i^{ur} = \boldsymbol{\phi}_i^{\mathrm{T}}\boldsymbol{f}/\lambda_i$, $i = 1, \ldots, k$, and the approximated solution is obtained by $\boldsymbol{d} \approx \boldsymbol{P}\boldsymbol{d}^{ur}$.

The second MOR approach considers decomposed reduction (DR) from the fine scale system via separate projections for the smooth and the non-smooth parts of the fine scale solution, named ISBFM-DR. Under this approach, the reduced coefficient vector $\boldsymbol{d}^{dr} \in \mathbb{R}^{k\times 1}$ constitutes of a reduced coefficient vector for the smooth part $\bar{\boldsymbol{d}}^{dr} \in \mathbb{R}^{\bar{k}\times 1}$ and a reduced coefficient vector for the non-smooth part $\hat{\boldsymbol{d}}^{dr} \in \mathbb{R}^{\hat{k}\times 1}$ that are obtained from a decomposed projection matrix with

superscript "dr" denoting the decomposed reduction approach, given as

$$\begin{bmatrix} \bar{\boldsymbol{P}} & \mathbf{0} \\ \mathbf{0} & \hat{\boldsymbol{P}} \end{bmatrix} \in \mathbb{R}^{(\bar{N}+\hat{N})\times(\bar{k}+\hat{k})} \tag{4.21}$$

where $\bar{\boldsymbol{P}} \in \mathbb{R}^{\bar{N}\times\bar{k}}$ and $\hat{\boldsymbol{P}} \in \mathbb{R}^{\hat{N}\times\hat{k}}$ are the sub-projections for the smooth and the non-smooth parts of the fine scale solution, respectively and the reduced dimension is $k = \bar{k} + \hat{k}$, with $\bar{k} \leq \bar{N}$ and $\hat{k} \leq \hat{N}$. The corresponding reduced system is given below

$$\begin{bmatrix} \bar{\boldsymbol{P}}^{\mathrm{T}} & \mathbf{0} \\ \mathbf{0} & \hat{\boldsymbol{P}}^{\mathrm{T}} \end{bmatrix} \begin{bmatrix} \bar{\boldsymbol{K}} & \hat{\boldsymbol{K}} \\ \hat{\boldsymbol{K}}^{\mathrm{T}} & \hat{\boldsymbol{K}} \end{bmatrix} \begin{bmatrix} \bar{\boldsymbol{P}} & \mathbf{0} \\ \mathbf{0} & \hat{\boldsymbol{P}} \end{bmatrix} \begin{bmatrix} \bar{\boldsymbol{d}}^{dr} \\ \hat{\boldsymbol{d}}^{dr} \end{bmatrix} = \begin{bmatrix} \bar{\boldsymbol{P}}^{\mathrm{T}} & \mathbf{0} \\ \mathbf{0} & \hat{\boldsymbol{P}}^{\mathrm{T}} \end{bmatrix} \begin{bmatrix} \bar{\boldsymbol{f}} \\ \hat{\boldsymbol{f}} \end{bmatrix} \tag{4.22}$$

We rewrite and denote above as follows

$$\boldsymbol{K}^{dr}\boldsymbol{d}^{dr} = \boldsymbol{f}^{dr} \tag{4.23}$$

where

$$\boldsymbol{K}^{dr} = \begin{bmatrix} \bar{\boldsymbol{K}}^{dr} & \hat{\boldsymbol{K}}^{dr} \\ \hat{\boldsymbol{K}}^{dr\mathrm{T}} & \hat{\boldsymbol{K}}^{dr} \end{bmatrix}, \quad \boldsymbol{d}^{dr} = \begin{bmatrix} \bar{\boldsymbol{d}}^{dr} \\ \hat{\boldsymbol{d}}^{dr} \end{bmatrix}, \quad \boldsymbol{f}^{dr} = \begin{bmatrix} \bar{\boldsymbol{f}}^{dr} \\ \hat{\boldsymbol{f}}^{dr} \end{bmatrix} \tag{4.24}$$

Here $\bar{\boldsymbol{K}}^{dr} = \bar{\boldsymbol{P}}^{T}\bar{\boldsymbol{K}}\bar{\boldsymbol{P}} \in \mathbb{R}^{\bar{k}\times\bar{k}}$, $\hat{\boldsymbol{K}}^{dr} = \bar{\boldsymbol{P}}^{T}\hat{\boldsymbol{K}}\hat{\boldsymbol{P}} \in \mathbb{R}^{\bar{k}\times\hat{k}}$ and $\hat{\boldsymbol{K}}^{dr} = \hat{\boldsymbol{P}}^{T}\hat{\boldsymbol{K}}\hat{\boldsymbol{P}} \in \mathbb{R}^{\hat{k}\times\hat{k}}$ are the sub-matrices of the reduced stiffness matrix $\boldsymbol{K}^{dr}$, $\bar{\boldsymbol{f}}^{dr} = \bar{\boldsymbol{P}}^{T}\bar{\boldsymbol{f}} \in \mathbb{R}^{\bar{k}\times 1}$ and $\hat{\boldsymbol{f}}^{dr} = \hat{\boldsymbol{P}}^{T}\hat{\boldsymbol{f}} \in \mathbb{R}^{\hat{k}\times 1}$ are the sub-vectors of the reduced force vector $\boldsymbol{f}^{dr}$. Here we assume that sub-matrices $\hat{\boldsymbol{K}}$ and $\hat{\boldsymbol{K}}^{dr}$ are nonsingular.

In ISBFM-DR, we first solve the coefficient vector of the smooth part and then compute the reduced coefficient vector of the non-smooth part. Consider the following decomposition of the fine scale equation in 4.17

$$\bar{\boldsymbol{K}}^{c}\bar{\boldsymbol{d}} = \bar{\boldsymbol{f}}^{c}, \quad \bar{\boldsymbol{K}}^{c} = \bar{\boldsymbol{K}} - \hat{\boldsymbol{K}}\hat{\boldsymbol{K}}^{-1}\hat{\boldsymbol{K}}^{\mathrm{T}}, \quad \bar{\boldsymbol{f}}^{c} = \bar{\boldsymbol{f}} - \hat{\boldsymbol{K}}\hat{\boldsymbol{K}}^{-1}\hat{\boldsymbol{f}} \tag{4.25a}$$

$$\hat{\boldsymbol{K}}\hat{\boldsymbol{d}} = \hat{\boldsymbol{f}}^c, \quad \hat{\boldsymbol{f}}^c = \hat{\boldsymbol{f}} - \hat{\boldsymbol{K}}^{\mathrm{T}}\bar{\boldsymbol{d}} \tag{4.25b}$$

The sub-projections matrices $\bar{\boldsymbol{P}}$ and $\hat{\boldsymbol{P}}$ in (4.21) are respectively obtained from the eigenanalysis of $\bar{\boldsymbol{K}}^c$ and $\hat{\boldsymbol{K}}$ from the condensed fine scale system in (4.25). That is, $\bar{\boldsymbol{P}} = [\boldsymbol{\varphi}_1\boldsymbol{\varphi}_2 \dots \boldsymbol{\varphi}_{\bar{k}}]$ and $\hat{\boldsymbol{P}} = [\boldsymbol{\xi}_1\boldsymbol{\xi}_2 \dots \boldsymbol{\xi}_{\hat{k}}]$, where $\{\boldsymbol{\varphi}_j, \mu_j\}_{j=1}^{\bar{k}}$ and $\{\boldsymbol{\xi}_l, \eta_l\}_{l=1}^{\hat{k}}$ are the smallest eigenpairs from matrices $\bar{\boldsymbol{K}}^c$ and $\hat{\boldsymbol{K}}$, respectively. The reduced coefficient vectors are obtained as $\bar{d}_j^{dr} = \boldsymbol{\varphi}_j^{\mathrm{T}}\bar{\boldsymbol{f}}^c/\mu_j$, $j = 1, \dots, \bar{k}$ and $\hat{d}_l^{dr} = \boldsymbol{\xi}_l^{\mathrm{T}}\hat{\boldsymbol{f}}^{cdr}/\eta_l$, $l = 1, \dots, \hat{k}$, where $\hat{\boldsymbol{f}}^{cdr} = \hat{\boldsymbol{f}} - \hat{\boldsymbol{K}}^{\mathrm{T}}\bar{\boldsymbol{P}}\bar{\boldsymbol{d}}^{dr}$. The approximation from the reduced order solution is then obtained as $\boldsymbol{d}^{\mathrm{T}} \approx [[\bar{\boldsymbol{P}}\bar{\boldsymbol{d}}^{dr}]^{\mathrm{T}}, [\hat{\boldsymbol{P}}\hat{\boldsymbol{d}}^{dr}]^{\mathrm{T}}]$.

Remark 4.1. *If global enrichment is used, the number of non-smooth DOF is relatively small compared to the number of smooth DOF. In this case one can consider to reduce only the smooth coefficients of the solution only and keep the enriched DOF to be unprojected. That is, in the ISBFM-DR method, the dimension $\hat{k} = \hat{N}$ and $\hat{\boldsymbol{P}} = \boldsymbol{I}_{\hat{N}}$. As a result, there is no projection of the non-smooth DOF, and $\hat{\boldsymbol{d}}^{dr} \in \mathbb{R}^{\hat{N}\times 1}$ is obtained directly from $\hat{\boldsymbol{K}}\hat{\boldsymbol{d}} = \hat{\boldsymbol{f}}^{cdr}$.*

4.3 Numerical Examples and Discussions

In this section, we present numerical examples of Poisson problems with singularities to verify and validate the proposed ISBFM-UR and ISBFM-DR MOR methods.

4.3.1 Reduced Order Modeling of a L-shaped Domain Poisson Problem

In the following example, the proposed ISBFM-UR and ISBFM-DR methods are considered for the reduced order modeling of a Poisson problem with mild singularity. The ISBFM-DR method is introduced with order reduction only on the smooth solution, and no order reduction on the enriched solution, i.e. $\hat{\boldsymbol{P}} = \boldsymbol{I}_{\hat{N}}$ and $k = \bar{k} + \hat{N}$. From the definition of singularity problem in Chapter 3, we understand that the Poisson problem on a L-shaped domain, shown in Figure 4.2, contains a singularity of order $\alpha = 2/3$.

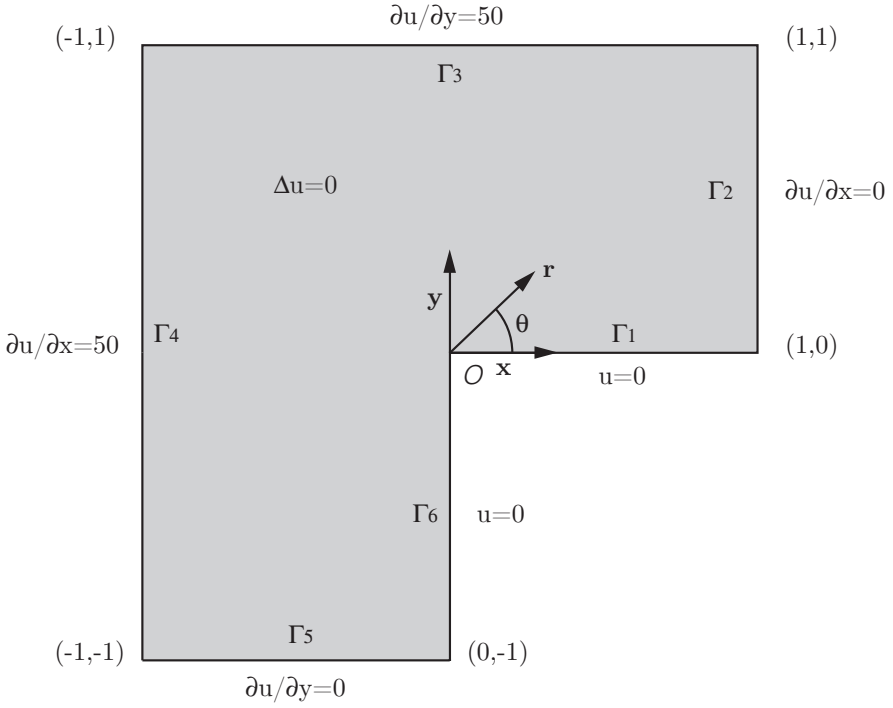

Figure 4.2: Model of L-shaped domain Poisson problem

The problem statement of this L-shaped domain Poisson problem is given as follows

$$\Delta u = 0 \quad \text{in } \Omega, \tag{4.26a}$$

subjected to the boundary conditions,

$$u|_{x=0,-1\leq y\leq 0} = 0, u|_{y=0,0\leq x\leq 1} = 0, \tag{4.26b}$$

$$\frac{\partial u}{\partial y}|_{y=-1,-1\leq x\leq 0} = 0, \frac{\partial u}{\partial x}|_{x=1,0\leq y\leq 1} = 0, \frac{\partial u}{\partial y}|_{y=1,-1\leq x\leq 1} = 50, \frac{\partial u}{\partial x}|_{x=-1,-1\leq y\leq 1} = 50 \tag{4.26c}$$

where $\Omega = [-1,1] \times [-1,1] \setminus [0,1] \times [0,1]$. The harmonic functions shown below are used as enrichment functions:

$$F_i(r,\theta) = r^{\frac{2}{3}i} \sin\left(\frac{2}{3}i\theta\right), \quad i = 1,2,\ldots \tag{4.27}$$

These enrichment functions, shown in Figure 4.3, satisfy the boundary conditions on Γ_1 and on

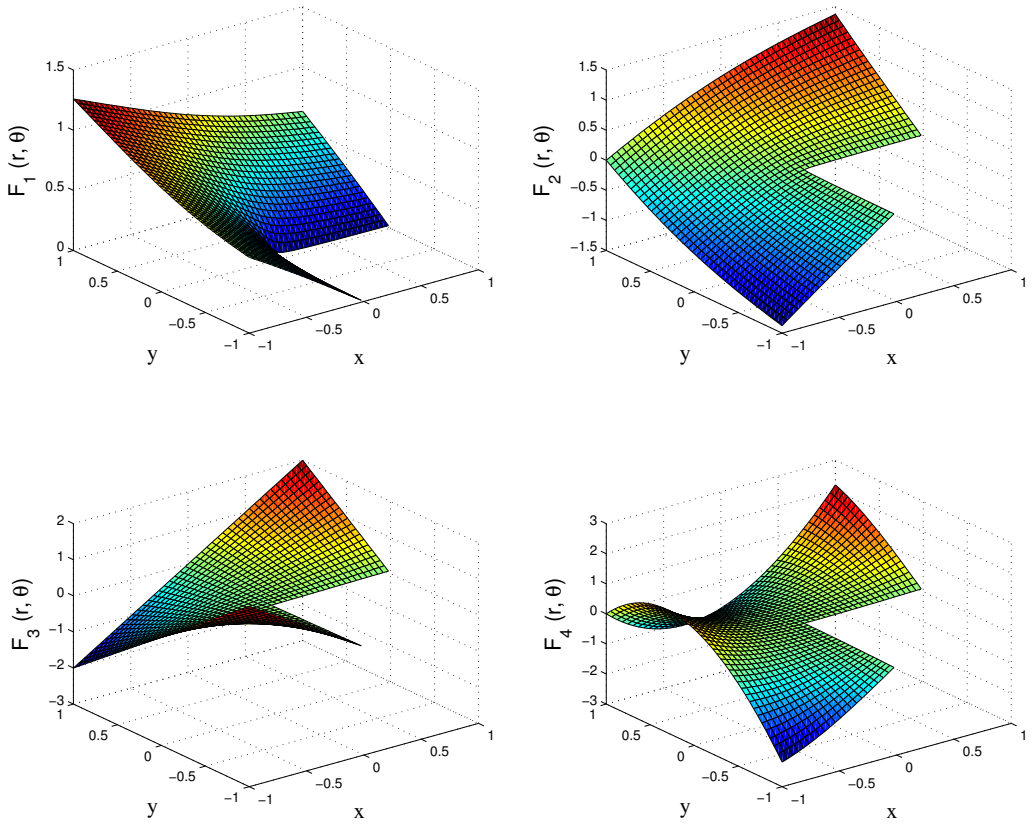

Figure 4.3: L-shaped domain Poisson problem's enrichment functions F_i for $i = 1, 2, 3, 4$

Γ_6 connected to the singularity point (x_0, y_0). In this numerical example, a uniform discretization 49×49 ($\bar{N} = 1825$) with one enrichment function ($\hat{N} = 1$) is used to obtain the fine scale solution.

The approximate solution of the fine scale model and its derivatives along $y = 0.001$ are shown in Figure 4.4. A comparison of the absolute error along $y = 0.001$ between the fine scale solution and the approximated reduced solutions obtained from ISBFM-UR and ISBFM-DR for a reduced dimension k, with different percentage of reduction $k/N = 5\%, 10\%, 20\%$, is presented in Figure 4.5. We first observe that ISBFM-UR approximates the fine scale solution poorly even when using a reduced model that contains 20% of the full DOF. On the other hand, the reduced order solution from ISBFM-DR yields a much smaller error, especially in the derivatives of the solution, where the error near the singularity points is not predominant.

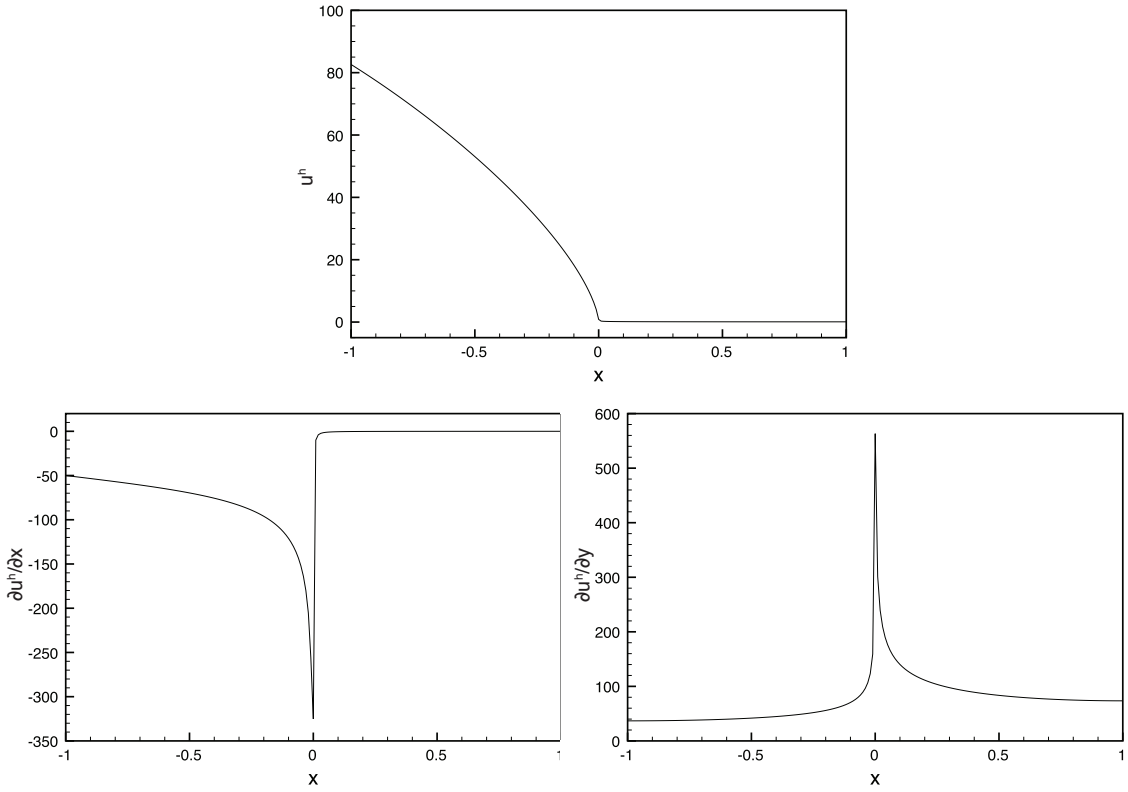

Figure 4.4: Fine scale approximation of the solution of the L-shaped domain Poisson problem along $y = 0.001$

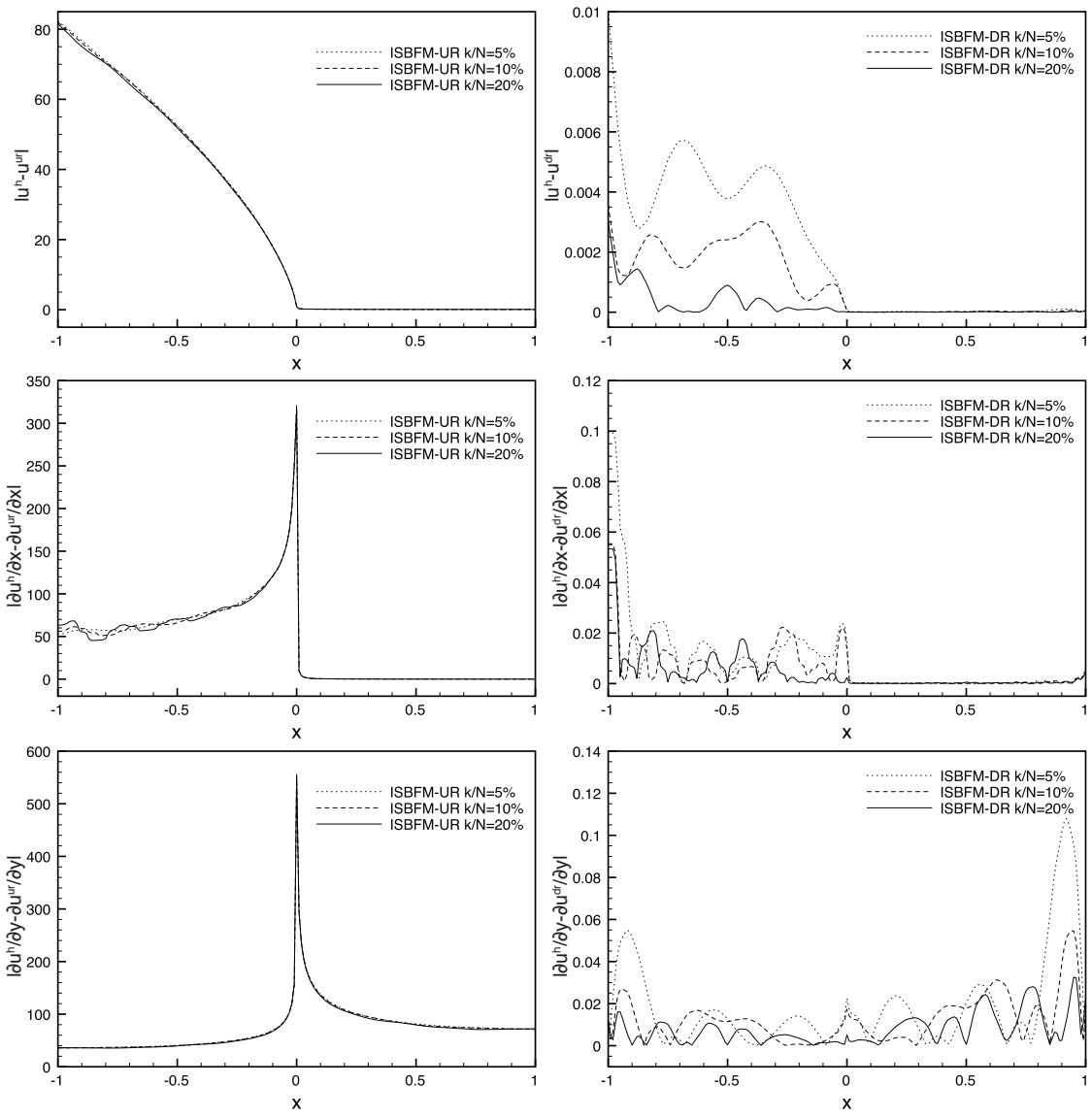

Figure 4.5: Absolute error distribution of the reduced solutions for the L-shaped domain Poisson problem with different percentage of k/N along $y = 0.001$

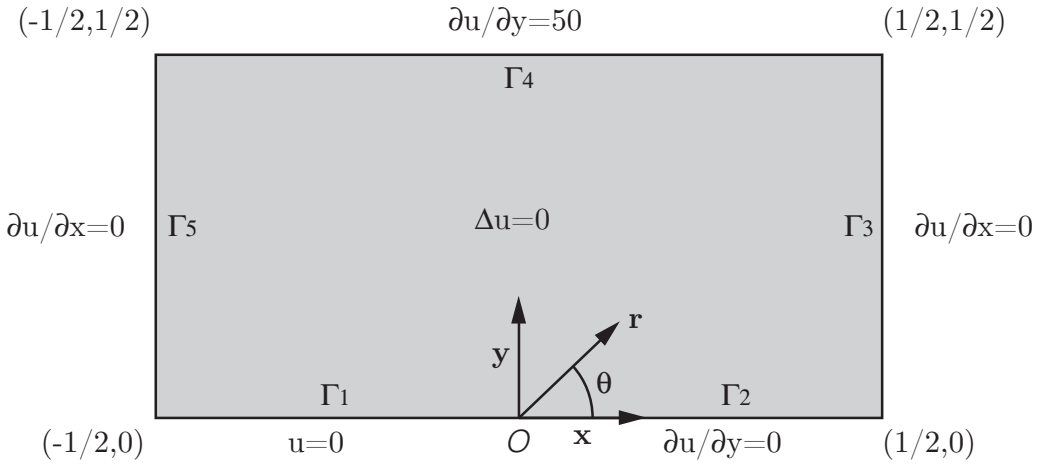

Figure 4.6: Model of cracked beam Poisson problem with prescribed traction

4.3.2 Reduced Order Modeling of a Cracked Beam Poisson Problem

The cracked beam Poisson problem with prescribed traction, described in Figure 4.6, possesses a stronger singularity than in the previous L-shaped domain Poisson problem. The proposed ISBFM-UR method and ISBFM-DR method with reduction only of the smooth part, are considered for the MOR.

The differential equation and boundary conditions of cracked beam Poisson problem is given below

$$\Delta u = 0 \quad \text{in } \Omega, \tag{4.28a}$$

subjected to the boundary conditions,

$$u|_{y=0,-1/2\leq x\leq 0} = 0, \tag{4.28b}$$

$$\begin{gathered} \tfrac{\partial u}{\partial y}|_{y=0,0\leq x\leq 1/2} = 0,\ \tfrac{\partial u}{\partial x}|_{x=-1/2,0\leq y\leq 1/2} = 0, \\ \tfrac{\partial u}{\partial y}|_{y=1/2,-1/2\leq x\leq 1/2} = 50,\ \tfrac{\partial u}{\partial x}|_{x=1/2,0\leq y\leq 1/2} = 0 \end{gathered} \tag{4.28c}$$

where $\Omega = [-1/2, 1/2] \times [0, 1/2]$. The harmonic singular basis functions F_i used in this problem are the same as in (3.19) of the cracked beam Poisson problem of Section 3.3. In this model

problem, the fine scale solution is obtained from a uniform nodal distribution 48×24 ($\bar{N} = 1152$) with one enrichment function ($\hat{N} = 1$).

The solution approximation of the full model and its approximate derivatives are shown along $y = 0.001$ near the singularity point in Figure 4.7. Figure 4.8 presents a comparison of the distribution of absolute errors of reduced solutions from ISBFM-UR and ISBFM-DR for different percentage of reduction $k/N = 5\%, 10\%, 20\%$, along $y = 0.001$. Compared to the ISBFM-UR approach, ISBFM-DR has a much smaller absolute error distribution for all reduced dimension k. For low reduced dimension $k/N = 5\%$, the reduced solution from ISBFM-UR poorly approximates the fine scale solution but the error does decrease when $k/N = 10\%$. Note that in the L-shaped domain case, the error of the ISBFM-UR solution does not reduce until much higher k/N is used. In this example, ISBFM-UR could be used for the reduction of the system, but the convergence behavior of this method seems to be problem dependent, whereas the ISBFM-DR method provides a fairly reliable reduced model for each examples.

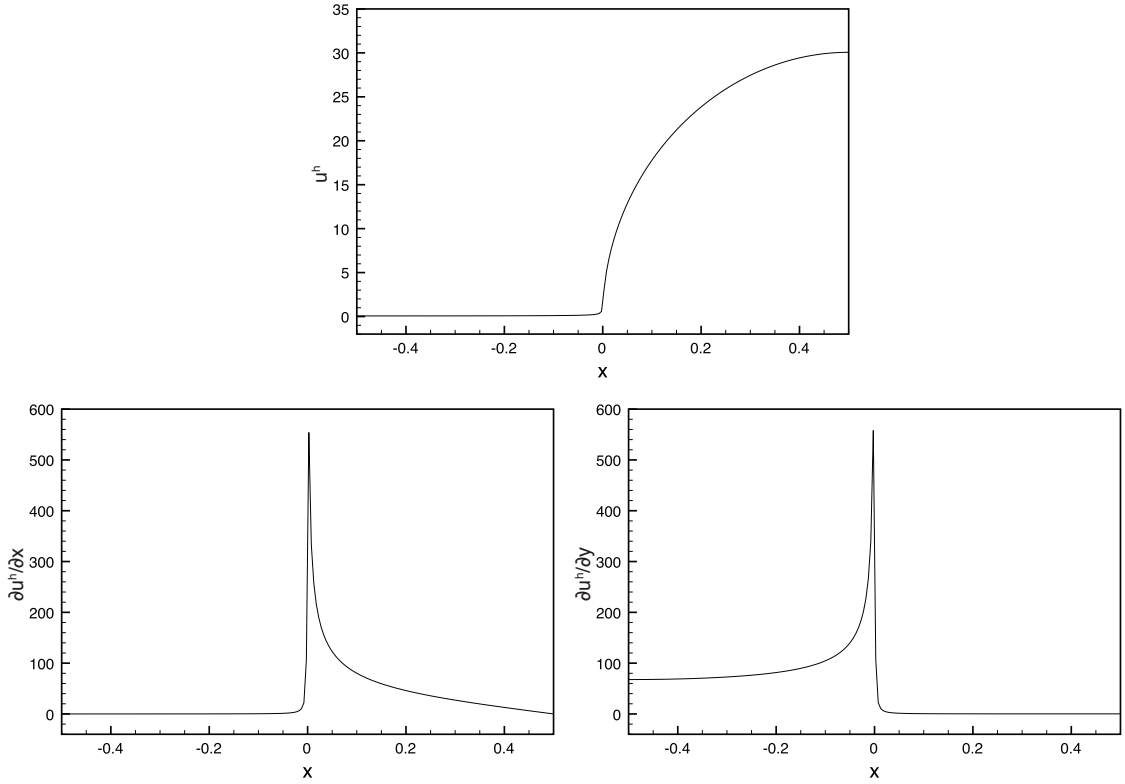

Figure 4.7: Fine scale approximation of the solution of the cracked beam Poisson problem along $y = 0.001$

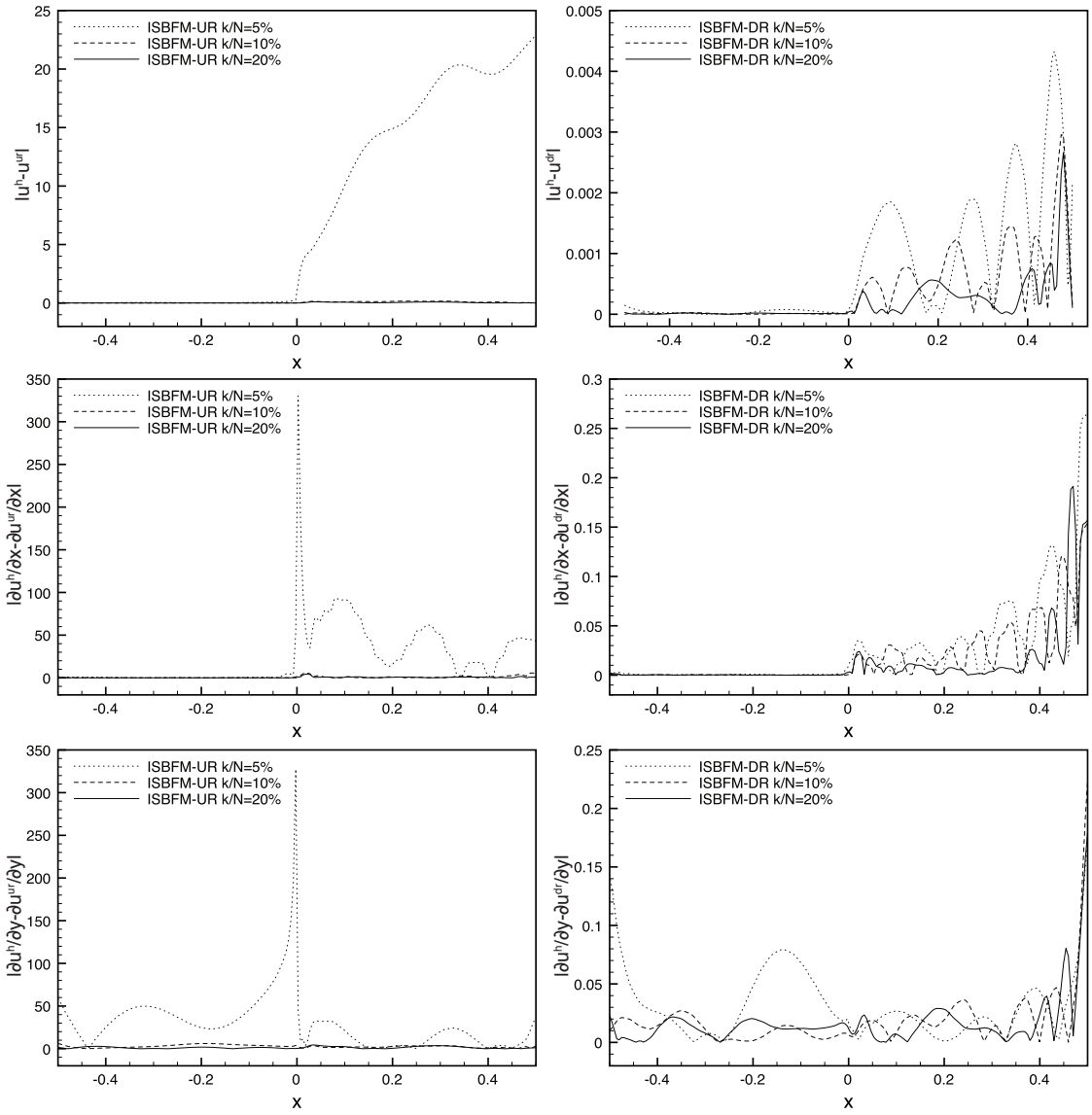

Figure 4.8: Absolute error distribution of the reduced solutions for the cracked beam Poisson problem with different percentage of k/N along $y = 0.001$

Chapter 5

Meshfree ISBFM Galerkin Formulation for Linear Elastic Fracture Mechanics

5.1 Preliminaries

Meshfree solution to linear elastic fracture mechanics (LEFM) under the ISBFM Galerkin framework is investigated in this chapter. We consider using the local asymptotic solution around the crack tip based on Airy's stress functions [Kanninen and Popelar, 1985] that satisfy the equilibrium equation and the traction free boundary condition on the crack surfaces as the enrichments to the RK approximation. This approximation is applied to the ISBFM Galerkin formulation to construct the discrete system for LEFM.

5.1.1 Basic Equations in Linear Elastic Fracture Mechanics

Consider a 2D linear elastic fracture mechanics problem defined as

$$\sigma_{ij,j} = 0 \quad \text{in } \Omega, \tag{5.1a}$$

subjected to the boundary conditions,

$$u_i = g_i \quad \text{on } \Gamma_{g_i}, \tag{5.1b}$$

$$\sigma_{ij} n_j = h_i \quad \text{on } \Gamma_{h_i} \tag{5.1c}$$

where Ω is a cracked domain bounded by $\partial\Omega = \Gamma = \Gamma_g \cup \Gamma_h \cup \Gamma_C$ as described in Figure 5.1, with $\Gamma_C = \Gamma_{C^+} \cup \Gamma_{C^-}$, in which the crack faces Γ_{C^+} and Γ_{C^-} are traction free.

The stress field $\boldsymbol{\sigma} = \{\sigma_{11}\ \sigma_{22}\ \sigma_{12}\}^{\mathrm{T}}$ and the strain field $\boldsymbol{\epsilon} = \{\epsilon_{11}\ \epsilon_{22}\ 2\epsilon_{12}\}^{\mathrm{T}} = \{u_{1,1}\, u_{2,2}\, (u_{1,2} + u_{2,1})\}^{\mathrm{T}}$ satisfy the constitutive relation $\boldsymbol{\sigma} = \boldsymbol{C}\boldsymbol{\epsilon}$, where $\boldsymbol{C}$ is the elastic tensor defined as

$$\boldsymbol{C} = \begin{cases} \dfrac{E}{(1+\nu)(1-2\nu)} \begin{bmatrix} 1-\nu & \nu & 0 \\ \nu & 1-\nu & 0 \\ 0 & 0 & \frac{1-2\nu}{2} \end{bmatrix} & \text{for plane strain} \\ \dfrac{E}{(1-\nu)^2} \begin{bmatrix} 1 & \nu & 0 \\ \nu & 1 & 0 \\ 0 & 0 & \frac{1-\nu}{2} \end{bmatrix} & \text{for plane stress} \end{cases} \tag{5.2}$$

where E is the Young modulus and ν is the Poisson's ratio.

In LEFM, Griffith [Griffith, 1921] defined the strain energy release rate G as the amount of energy released per unit of crack surface as the crack propagates as follows

$$G = \frac{dW}{dA} - \frac{dU}{dA} \tag{5.3}$$

where W is the external work done to the body, U is the internal strain energy and A is the crack surface area. A crack will grow when the strain energy release rate G reaches the critical value of the material's resistance to crack initiation G_C.

This energy balance approach was extended by Irwin's work for the fracture of ductile materials

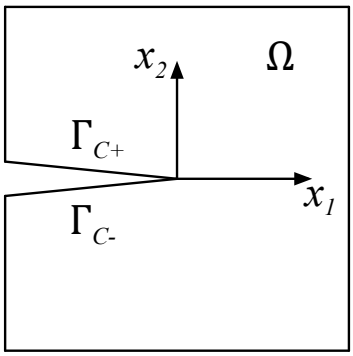

Figure 5.1: Model of a cracked domain

[Irwin, 1957] which relates the strain energy release rate which is a global measure to the stress intensity factor (SIF) K representing the local stress state near the crack tip [Irwin, 1958] by the following relationship

$$G = \frac{K^2}{E^*} \tag{5.4}$$

where $E^* = E/(1-\nu^2)$ for plane strain and $E^* = E$ for plane stress. The SIF K has also been used to indicate crack growth when it reaches the fracture toughness K_C of the material. The SIF is determined by the characteristics of the problem, such as the crack location and size, the loading and the domain geometry and can be evaluated using J-integrals [Rice, 1968]. The J-integral is a path-independent contour integral around the crack. The strain energy release rate G can be related to the J-integral as

$$J = \int_\Gamma \left(W n_1 - \sigma_{ij} n_i \frac{\partial u_j}{\partial x_1} \right) \, \mathrm{d}\Gamma = G \tag{5.5}$$

where Γ can be any path connecting the two crack surfaces, as in Figure 5.2, W is the strain energy density, n_i is the outward normal to Γ, σ_{ij} is the stress, u_j the displacement and x_1 is the direction of the crack.

The J-integral from (5.5) can also be expressed in the domain integral form [Li et al., 1985]

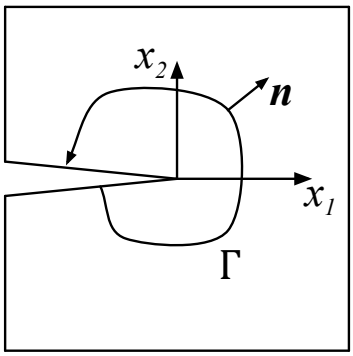

Figure 5.2: Arbitrary contour integral around the crack tip

[Shih et al., 1986] [Moran and Shih, 1987] as

$$J = \int_{\Omega_C} \left(\sigma_{ij} \frac{\partial u_j}{\partial x_1} - W \delta_{1j} \right) \frac{\partial q}{\partial x_j} \, \mathrm{d}\Omega \tag{5.6}$$

where Ω_C is an enclosed domain surrounding the crack tip, q is a smooth weight function that is zero outside of and Ω_C is constant on an area containing the crack tip.

The crack propagation is defined as the addition of a new crack surface formation, for which the crack propagation direction needs to be determined from different criteria. The strain energy release rate failure criterion states that the crack propagates along the direction of maximum energy release rate [Nuismer, 1975]. Other criteria include the direction normal to the one of maximum hoop stress [Erdogan and Sih, 1963] or normal to the one of minimum strain energy density [Sih, 1974].

The difficulty in modeling cracks is to represent both the discontinuity in the displacement field and the stress concentration at the crack tip. In the next section, enhancements of smooth approximations for crack modeling are discussed.

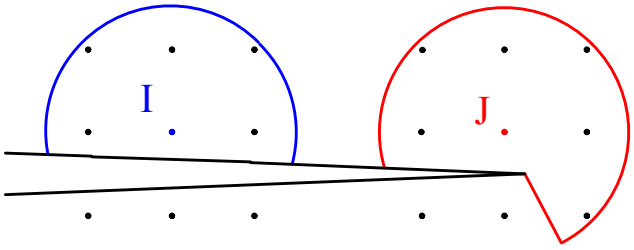

Figure 5.3: Truncation of the support of nodes I and J near the crack surface

5.1.2 Numerical Treatments of Cracks

The discontinuities across the crack surface have been modeled by modifying the kernel of the shape functions using the visibility criterion or Heaviside enrichment function. Both methods modify the domain of influence of nodes near the crack to introduce discontinuities across the crack surface into the approximation. In the visibility criterion technique [Belytschko et al., 1996b], the domain of influence for nodes near the crack is truncated whenever it intersects the crack surface as shown in Figure 5.3. In this manner, the approximation function associated with a node on one side of the crack does not influence the nodes on the opposite side of the crack.

As shown in 5.3, the visibility criterion leads to a spurious discontinuity in the kernel function as well as in the approximation function which can be relieved by the diffraction method [Organ et al., 1996] that wraps the support around the crack tip. In this study, enrichment techniques are proposed to represent both crack surface and stress singularity at the crack tip.

Enrichment functions based on the asymptotic displacement field near crack tip introduce a discontinuity across the crack facein the displacement field and a singularity in the strain and the stress fields at the crack tip. The local asymptotic solution for LEFM problems will be given in Section 5.2.2.

5.2 Extension of ISBFM to LEFM Problems

5.2.1 ISBFM Galerkin Formulation

ISBFM Galerkin formulation is derived in this section for the case of linear elastic fracture mechanics problem. Consider the following functional associated with the strong formulation given in (5.1):

$$\begin{aligned} I = &\frac{1}{2}\int_{\Omega}\left(\bar{u}^h_{(i,j)}+\hat{u}^h_{(i,j)}\right)C_{ijkl}\left(\bar{u}^h_{(k,l)}+\hat{u}^h_{(k,l)}\right)\,\mathrm{d}\Omega-\int_{\Gamma_{h_i}}\left(\bar{u}^h_i+\hat{u}^h_i\right)h_i\,\mathrm{d}\Gamma \\ &-\int_{\Gamma_{g_i}}\left(\bar{\sigma}^h_{ij}+\hat{\sigma}^h_{ij}\right)n_j\left(\bar{u}^h_i+\hat{u}^h_i-g_i\right)\,\mathrm{d}\Gamma+\frac{\beta}{2}\int_{\Gamma_{g_i}}\left(\bar{u}^h_i+\hat{u}^h_i-g_i\right)\left(\bar{u}^h_i+\hat{u}^h_i-g_i\right)\,\mathrm{d}\Gamma \end{aligned} \tag{5.7}$$

By minimizing of the functional (5.7), the standard Galerkin formulation is obtained as follows

$$\begin{aligned} &\int_{\Omega}\delta\bar{u}^h_{(i,j)}C_{ijkl}\left(\bar{u}^h_{(k,l)}+\hat{u}^h_{(k,l)}\right)\,\mathrm{d}\Omega \\ &-\int_{\Gamma_{g_i}}\left(\delta\bar{u}^h_i\left(C_{ijkl}\left(\bar{u}^h_{(k,l)}+\hat{u}^h_{(k,l)}\right)n_j-\beta\left(\bar{u}^h_i+\hat{u}^h_i\right)\right)+\delta\bar{\sigma}^h_{ij}n_j\left(\bar{u}^h_i+\hat{u}^h_i\right)\right)\,\mathrm{d}\Gamma \\ &=\int_{\Gamma_{h_i}}\delta\bar{u}^h_i h_i\,\mathrm{d}\Gamma-\int_{\Gamma_{g_i}}\left(-\delta\bar{u}^h_i\beta g_i+\delta\bar{\sigma}^h_{ij}n_j g_i\right)\,\mathrm{d}\Gamma \end{aligned} \tag{5.8a}$$

$$\begin{aligned} &\int_{\Omega}\delta\hat{u}^h_{(i,j)}C_{ijkl}\left(\bar{u}^h_{(k,l)}+\hat{u}^h_{(k,l)}\right)\,\mathrm{d}\Omega \\ &-\int_{\Gamma_{g_i}}\left(\delta\hat{u}^h_i\left(C_{ijkl}\left(\bar{u}^h_{(k,l)}+\hat{u}^h_{(k,l)}\right)n_j-\beta\left(\bar{u}^h_i+\hat{u}^h_i\right)\right)+\delta\hat{\sigma}^h_{ij}n_j\left(\bar{u}^h_i+\hat{u}^h_i\right)\right)\,\mathrm{d}\Gamma \\ &=\int_{\Gamma_{h_i}}\delta\hat{u}^h_i h_i\,\mathrm{d}\Gamma-\int_{\Gamma_{g_i}}\left(-\delta\hat{u}^h_i\beta g_i+\delta\hat{\sigma}^h_{ij}n_j g_i\right)\,\mathrm{d}\Gamma \end{aligned} \tag{5.8b}$$

where $\bar{\sigma}^h_{ij}=C_{ijkl}\bar{\epsilon}^h_{kl}=C_{ijkl}\bar{u}^h_{(k,l)}$ and $\hat{\sigma}^h_{ij}=C_{ijkl}\hat{\epsilon}^h_{kl}=C_{ijkl}\hat{u}^h_{(k,l)}$.

Under the ISBFM framework, the enrichment functions for the non-smooth solution $\hat{\boldsymbol{u}}^h$ are selected to satisfy the equilibrium equation, i.e. $\hat{\sigma}^h_{ij,j}=C_{ijkl}\hat{\epsilon}^h_{kl,j}=C_{ijkl}\hat{u}^h_{(k,l),j}=0$ on Ω. In this manner, the domain integral involving singular basis functions can be expressed as a boundary

integral using the integration by parts theorem below

$$\int_\Omega v_{(i,j)} C_{ijkl} \hat{u}^h_{(k,l)} \, \mathrm{d}\Omega = \int_\Gamma v_i C_{ijkl} \hat{u}^h_{(k,l)} n_j \, \mathrm{d}\Gamma - \int_\Omega v_i C_{ijkl} \hat{u}^h_{(k,l),j} \, \mathrm{d}\Omega, \quad \forall \boldsymbol{v} \in V \tag{5.9}$$

With the non-smooth approximation satisfying the equilibrium equation, we have

$$\int_\Omega v_{(i,j)} C_{ijkl} \hat{u}^h_{(k,l)} \, \mathrm{d}\Omega = \int_\Gamma v_i C_{ijkl} \hat{u}^h_{(k,l)} n_j \, \mathrm{d}\Gamma, \quad \forall \boldsymbol{v} \in V \tag{5.10}$$

Consequently, equation (5.8) becomes as

$$\begin{aligned}
&\int_\Omega \delta \bar{u}^h_{(i,j)} C_{ijkl} \bar{u}^h_{(k,l)} \, \mathrm{d}\Omega - \int_{\Gamma_{g_i}} \left(\delta \bar{u}^h_i \left(C_{ijkl} \bar{u}^h_{(k,l)} n_j - \beta \bar{u}^h_i \right) + \delta \bar{\sigma}^h_{ij} n_j \bar{u}^h_i \right) \, \mathrm{d}\Gamma \\
&+ \int_\Gamma \delta \bar{u}^h_i C_{ijkl} \hat{u}^h_{(k,l)} n_j \, \mathrm{d}\Gamma - \int_{\Gamma_{g_i}} \left(\delta \bar{u}^h_i \left(C_{ijkl} \hat{u}^h_{(k,l)} n_j - \beta \hat{u}^h_i \right) + \delta \bar{\sigma}^h_{ij} n_j \hat{u}^h_i \right) \, \mathrm{d}\Gamma \\
&= \int_{\Gamma_{h_i}} \delta \bar{u}^h_i h_i \, \mathrm{d}\Gamma - \int_{\Gamma_{g_i}} \left(-\delta \bar{u}^h_i \beta g_i + \delta \bar{\sigma}^h_{ij} n_j g_i \right) \, \mathrm{d}\Gamma
\end{aligned} \tag{5.11a}$$

$$\begin{aligned}
&\int_\Gamma \delta \hat{u}^h_{(i,j)} C_{ijkl} \bar{u}^h_k n_l \, \mathrm{d}\Gamma - \int_{\Gamma_{g_i}} \left(\delta \hat{u}^h_i \left(C_{ijkl} \bar{u}^h_{(k,l)} n_j - \beta \bar{u}^h_i \right) + \delta \hat{\sigma}^h_{ij} n_j \bar{u}^h_i \right) \, \mathrm{d}\Gamma \\
&+ \int_\Gamma \delta \hat{u}^h_i C_{ijkl} \hat{u}^h_{(k,l)} n_j \, \mathrm{d}\Gamma - \int_{\Gamma_{g_i}} \left(\delta \hat{u}^h_i \left(C_{ijkl} \hat{u}^h_{(k,l)} n_j - \beta \hat{u}^h_i \right) + \delta \hat{\sigma}^h_{ij} n_j \hat{u}^h_i \right) \, \mathrm{d}\Gamma \\
&= \int_{\Gamma_{h_i}} \delta \hat{u}^h_i h_i \, \mathrm{d}\Gamma - \int_{\Gamma_{g_i}} \left(-\delta \hat{u}^h_i \beta g_i + \delta \hat{\sigma}^h_{ij} n_j g_i \right) \, \mathrm{d}\Gamma
\end{aligned} \tag{5.11b}$$

If the enrichment basis functions are required to satisfy the homogeneous boundary conditions on Γ_C, i.e. $C_{ijkl} \hat{u}^h_{(k,l)} n_j = 0$ on $\Gamma_{h_i} \cup \Gamma_{C^+}$ and $\Gamma_{h_i} \cup \Gamma_{C^-}$. By defining $\bar{\Gamma}_{h_i} = \Gamma_{h_i} \setminus \Gamma_C$ and $\bar{\Gamma}_{g_i} = \Gamma_{g_i} \setminus \Gamma_C$, the ISBFM Galerkin formulation for LEFM becomes

$$\begin{aligned}
&\int_\Omega \delta \bar{u}^h_{(i,j)} C_{ijkl} \bar{u}^h_{(k,l)} \, \mathrm{d}\Omega - \int_{\bar{\Gamma}_{g_i}} \left(\delta \bar{u}^h_i \left(C_{ijkl} \bar{u}^h_{(k,l)} n_j - \beta \bar{u}^h_i \right) + \delta \bar{\sigma}^h_{ij} n_j \bar{u}^h_i \right) \, \mathrm{d}\Gamma \\
&+ \int_{\bar{\Gamma}_{h_i}} \delta \bar{u}^h_i C_{ijkl} \hat{u}^h_{(k,l)} n_j \, \mathrm{d}\Gamma - \int_{\bar{\Gamma}_{g_i}} \left(-\delta \bar{u}^h_i \beta \hat{u}^h_i + \delta \bar{\sigma}^h_{ij} n_j \hat{u}^h_i \right) \, \mathrm{d}\Gamma \\
&= \int_{\Gamma_{h_i}} \delta \bar{u}^h_i h_i \, \mathrm{d}\Gamma - \int_{\Gamma_{g_i}} \left(-\delta \bar{u}^h_i \beta g_i + \delta \bar{\sigma}^h_{ij} n_j g_i \right) \, \mathrm{d}\Gamma
\end{aligned} \tag{5.12a}$$

$$
\begin{aligned}
&\int_{\bar{\Gamma}_{h_i}} \delta\hat{u}^h_{(i,j)} C_{ijkl} \bar{u}^h_k n_l \, \mathrm{d}\Gamma - \int_{\bar{\Gamma}_{g_i}} \left(-\delta\hat{u}^h_i \beta \bar{u}^h_i + \delta\hat{\sigma}^h_{ij} n_j \bar{u}^h_i\right) \, \mathrm{d}\Gamma \\
&+ \int_{\bar{\Gamma}_{h_i}} \delta\hat{u}^h_i C_{ijkl} \hat{u}^h_{(k,l)} n_j \, \mathrm{d}\Gamma - \int_{\bar{\Gamma}_{g_i}} \left(-\delta\hat{u}^h_i \beta \hat{u}^h_i + \delta\hat{\sigma}^h_{ij} n_j \hat{u}^h_i\right) \, \mathrm{d}\Gamma \\
&= \int_{\Gamma_{h_i}} \delta\hat{u}^h_i h_i \, \mathrm{d}\Gamma - \int_{\Gamma_{g_i}} \left(-\delta\hat{u}^h_i \beta g_i + \delta\hat{\sigma}^h_{ij} n_j g_i\right) \, \mathrm{d}\Gamma
\end{aligned}
\tag{5.12b}
$$

In the next section, the enrichment functions which satisfy both the equilibrium equation and the traction free crack surface condition will be derived.

5.2.2 Discretization of ISBFM Galerkin Formulation

The RK approximation is introduced for the smooth approximation $\bar{\boldsymbol{u}}^h$ and the non-smooth approximation $\hat{\boldsymbol{u}}^h$ is obtained from a linear combination of enrichment functions $\boldsymbol{F}$ which satisfy equilibrium and the traction free boundary condition on the crack surface, i.e. $C_{ijkl} F_{M(k,l),j} = 0$ on Ω, $C_{ijkl} F_{M(k,l)} n_j = 0$ on $\Gamma_{h_i} \cup \Gamma_{C^+}$ and $\Gamma_{h_i} \cup \Gamma_{C^-}$.

The enrichment functions commonly used in fracture mechanic problems are four branch functions, defined as

$$
\boldsymbol{F} = \left\{ r^{1/2}\sin(\theta/2), \quad r^{1/2}\cos(\theta/2), \quad r^{1/2}\sin(\theta/2)\sin(\theta), \quad r^{1/2}\cos(\theta/2)\sin(\theta) \right\} \tag{5.13}
$$

Using those enrichment functions, the non-smooth approximation is $\hat{\boldsymbol{u}}^h = \sum_{M=1}^{4} F_M \hat{\boldsymbol{d}}_M$, i.e. $\hat{u}^h_i = \sum_{M=1}^{4} F_M \hat{d}_{Mi}$, where $\hat{\boldsymbol{d}}_M \in \mathbb{R}^{2\times 1}$. Although these enrichment functions compose the first symmetric and anti-symmetric part of the near crack tip asymptotic solution when used separately in both directions, each individual basis function does not satisfy the PDE on Ω by itself. Thus they are not adequate for the ISBFM Galerkin formulation in (5.12).

Instead, we introduce the local asymptotic solution derived from Williams' solution [Williams, 1952] [Williams, 1957]:

$$
\hat{u}^h_i = \sum_{M=1}^{\hat{N}} F^{\text{sym}}_{Mi} \hat{d}^{\text{sym}}_M + \sum_{M=1}^{\hat{N}} F^{\text{antisym}}_{Mi} \hat{d}^{\text{antisym}}_M \text{ or } \hat{\boldsymbol{u}}^h = \sum_{M=1}^{\hat{N}} \boldsymbol{F}_M \hat{\boldsymbol{d}}_M \tag{5.14}
$$

where $\hat{\boldsymbol{d}}_M = [\hat{d}_M^{\text{sym}} \ \hat{d}_M^{\text{antisym}}]^{\text{T}}$ and $\boldsymbol{F}_M = [F_{Mi}^{\text{sym}} \ F_{Mi}^{\text{antisym}}]$ where

$$\begin{cases} F_{M1}^{\text{sym}}(r,\theta) & = r^{M/2}\left[\left(\kappa + \frac{M}{2} + (-1)^m\right)\cos\left(\frac{M\theta}{2}\right) - \frac{M}{2}\cos\left(\left(\frac{M}{2}-2\right)\theta\right)\right] \\ F_{M2}^{\text{sym}}(r,\theta) & = r^{M/2}\left[\left(\kappa - \frac{M}{2} - (-1)^m\right)\sin\left(\frac{M\theta}{2}\right) + \frac{M}{2}\sin\left(\left(\frac{M}{2}-2\right)\theta\right)\right] \end{cases} \tag{5.15a}$$

$$\begin{cases} F_{M1}^{\text{antisym}}(r,\theta) & = -r^{M/2}\left[\left(\kappa + \frac{M}{2} - (-1)^M\right)\sin\left(\frac{M\theta}{2}\right) - \frac{M}{2}\sin\left(\left(\frac{M}{2}-2\right)\theta\right)\right] \\ F_{M2}^{\text{antisym}}(r,\theta) & = r^{M/2}\left[\left(\kappa - \frac{M}{2} + (-1)^M\right)\cos\left(\frac{M\theta}{2}\right) + \frac{M}{2}\cos\left(\left(\frac{M}{2}-2\right)\theta\right)\right] \end{cases} \tag{5.15b}$$

Here $\theta \in [-\pi, \pi]$ and κ is the Kolosov constant defined as $\kappa = 3 - 4\nu$ for plane strain and $\kappa = (3-\nu)/(1+\nu)$ for plane stress. These basis functions satisfy the equilibrium equation and the homogeneous boundary condition near the singularity points. Enrichment functions corresponding to even M can be recovered by polynomial basis and are not considered in the approximation if they are linearly dependent with the RK shape functions. Therefore, the selection of the enrichment basis function depends on the desired order of completeness of the RK shape functions. The first enrichment shape functions corresponding to odd values of M are shown in Figure 5.4 for the symmetric bases $\boldsymbol{F}_M^{sym}$ and in Figure 5.5 for the anti-symmetric bases $\boldsymbol{F}_M^{antisym}$. We can recognize that the first symmetric and anti-symmetric enrichment functions, for $M = 1$, correspond respectively to the basis of the analytical solution of the crack opening Mode I and sliding Mode II, illustrated in Figure 5.6.

The set of enrichment basis functions $\boldsymbol{F}_M$ defined in (5.14) is composed of both symmetric and anti-symmetric functions. If the symmetric or anti-symmetric behavior of the exact solution is known from the loading or the domain geometry, we may only select symmetric or anti-symmetric basis for the enriched part of the solution.

5.2.3 Discrete System

The discretization of ISBFM Galerkin formulation serves as a full scale model for the MOR approach, as will be described in the next chapter. The corresponding discrete system is detailed in

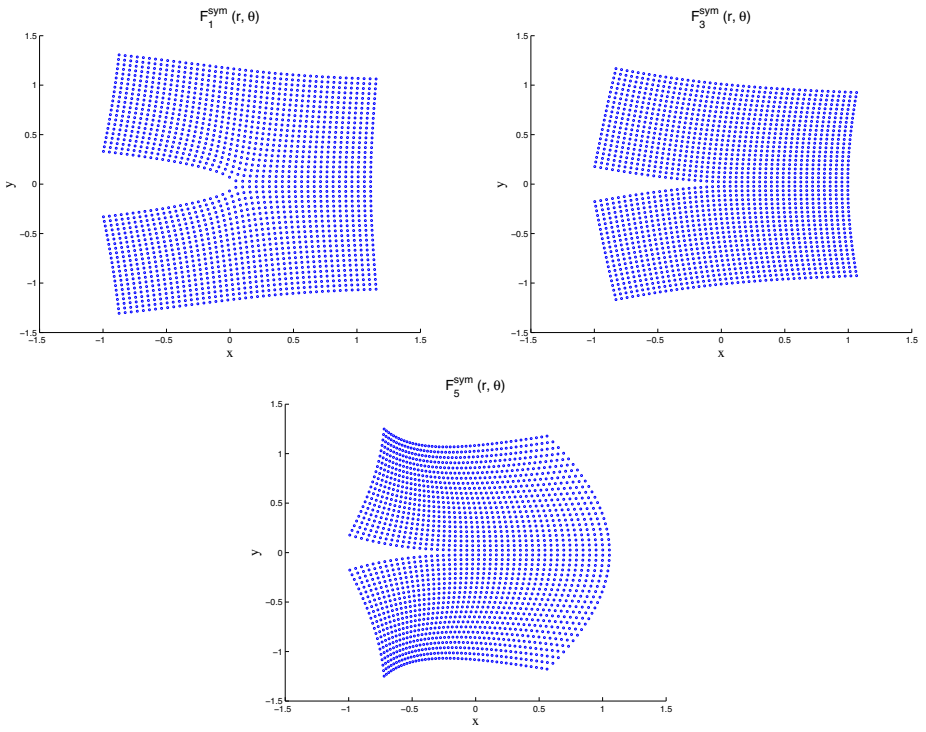

Figure 5.4: Symmetric enrichment functions $\boldsymbol{F}_M^{sym}$ for $M = 1, 3, 5$

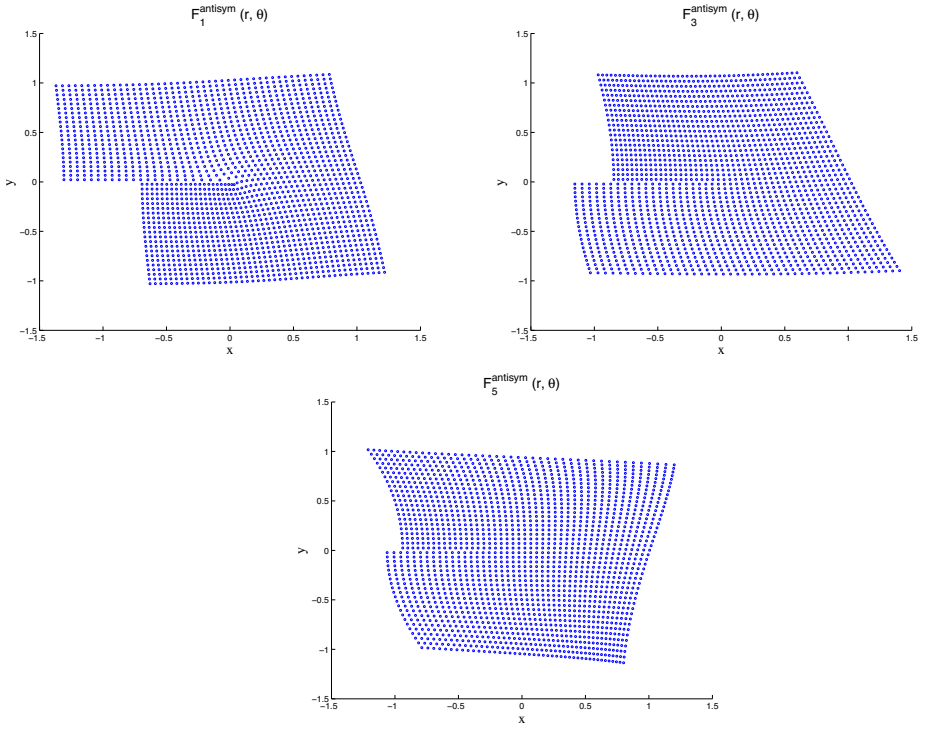

Figure 5.5: Anti-symmetric enrichment functions $\boldsymbol{F}_M^{antisym}$ for $M = 1, 3, 5$

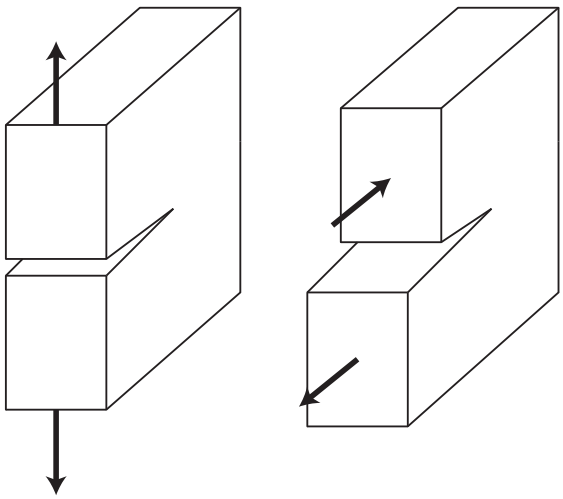

Mode I: Opening Mode II: Sliding

Figure 5.6: Crack opening Mode I and crack sliding Mode II

the following.

The smooth part of the solution is expressed as

$$\bar{\boldsymbol{u}}^h(\boldsymbol{x}) = \begin{bmatrix} \boldsymbol{\Psi}^{\mathrm{T}}(\boldsymbol{x}) & \mathbf{0} \\ \mathbf{0} & \boldsymbol{\Psi}^{\mathrm{T}}(\boldsymbol{x}) \end{bmatrix} \bar{\boldsymbol{d}} \tag{5.16}$$

i.e. $\bar{u}_i^h(\boldsymbol{x}) = \boldsymbol{\Psi}^{\mathrm{T}}(\boldsymbol{x})\bar{\boldsymbol{d}}_i = \sum_{J=1}^{\bar{N}} \Psi_J(\boldsymbol{x})\bar{d}_{iJ}$ where Ψ_J are RK shape functions, $\bar{\boldsymbol{d}} \in \mathbb{R}^{2\bar{N}\times 1}$, and $\bar{N}$ is the number of RK nodes. The smooth stress field is defined as $\bar{\boldsymbol{\sigma}} = \{\bar{\sigma}_{11}^h \ \bar{\sigma}_{22}^h \ \bar{\sigma}_{12}^h\}^{\mathrm{T}} = \boldsymbol{C}\bar{\boldsymbol{\epsilon}}^h$, and the smooth strain field as $\bar{\boldsymbol{\epsilon}}^h = \{\bar{\epsilon}_{11}^h \ \bar{\epsilon}_{22}^h \ 2\bar{\epsilon}_{12}^h\}^{\mathrm{T}} = \{\bar{u}_{1,1}^h \ \bar{u}_{2,2}^h \ (\bar{u}_{1,2}^h + \bar{u}_{2,1}^h)\}^{\mathrm{T}} = \bar{\boldsymbol{B}}\bar{\boldsymbol{d}}$, where $\bar{\boldsymbol{B}} = \{\bar{\boldsymbol{B}}_1 \ \ldots \ \bar{\boldsymbol{B}}_J \ \ldots \ \bar{\boldsymbol{B}}_{\bar{N}}\}$ is defined with

$$\bar{\boldsymbol{B}}_J = \begin{bmatrix} \Psi_{J,1} & 0 \\ 0 & \Psi_{J,2} \\ \Psi_{J,2} & \Psi_{J,1} \end{bmatrix} \tag{5.17}$$

The non-smooth part of solution is approximated using the enrichment basis functions defined

in (5.15) consisting a symmetric and an anti-symmetric pair by

$$\hat{\boldsymbol{u}}^h = \sum_{M=1}^{\hat{N}} \boldsymbol{F}_M \hat{\boldsymbol{d}}_M = \sum_{M=1}^{\hat{N}} \boldsymbol{F}_M^{\text{sym}} \hat{d}_M^{\text{sym}} + \sum_{M=1}^{\hat{N}} \boldsymbol{F}_M^{\text{antisym}} \hat{d}_M^{\text{antisym}} \tag{5.18}$$

where $\boldsymbol{F}_M = [\boldsymbol{F}_M^{\text{sym}} \ \boldsymbol{F}_M^{\text{antisym}}] \in \mathbb{R}^{2\times 2}$ are the enrichment functions defined in (5.15), the non smooth coefficients are $\hat{\boldsymbol{d}} = [\hat{\boldsymbol{d}}_1 \ \dots \ \hat{\boldsymbol{d}}_M \ \dots \ \hat{\boldsymbol{d}}_{\hat{N}}] \in \mathbb{R}^{2\hat{N}\times 1}$ with $\hat{\boldsymbol{d}}_M = [\hat{d}_M^{\text{sym}} \ \hat{d}_M^{\text{antisym}}]$, and $\hat{N}$ is the number of enrichment basis functions used. The numerical non-smooth stress field is discretized as $\hat{\boldsymbol{\sigma}} = \{\hat{\sigma}_{11}^h \ \hat{\sigma}_{22}^h \ \hat{\sigma}_{12}^h\}^{\text{T}} = \boldsymbol{C}\hat{\boldsymbol{\epsilon}}^h$, and the numerical non-smooth strain field as $\hat{\boldsymbol{\epsilon}}^h = \{\hat{\epsilon}_{11}^h \ \hat{\epsilon}_{22}^h \ 2\hat{\epsilon}_{12}^h\}^{\text{T}} = \{\hat{u}_{1,1}^h \ \hat{u}_{2,2}^h \ (\hat{u}_{1,2}^h + \hat{u}_{2,1}^h)\}^{\text{T}} = \hat{\boldsymbol{B}}\hat{\boldsymbol{d}}$, where $\hat{\boldsymbol{B}} = [\hat{\boldsymbol{B}}_1 \ \dots \ \hat{\boldsymbol{B}}_M \ \dots \ \hat{\boldsymbol{B}}_{\hat{N}}]$ is defined with

$$\hat{\boldsymbol{B}}_M = \begin{bmatrix} F_{M1,1}^{\text{sym}} & F_{M1,1}^{\text{antisym}} \\ F_{M2,2}^{\text{sym}} & F_{M2,2}^{\text{antisym}} \\ F_{M1,2}^{\text{sym}} + F_{M2,1}^{\text{sym}} & F_{M1,2}^{\text{antisym}} + F_{M2,1}^{\text{antisym}} \end{bmatrix} \tag{5.19}$$

The choice of symmetric and/or anti-symmetric bases for the enrichments depends on the geometry and the loading of each specific problem.

The discretization of ISBFM Galerkin formulation defined in 5.12 can be written in a matrix form as follows

$$\boldsymbol{K}\boldsymbol{d} = \begin{bmatrix} \bar{\boldsymbol{K}} & \hat{\boldsymbol{K}} \\ \hat{\boldsymbol{K}}^{\text{T}} & \hat{\boldsymbol{K}} \end{bmatrix} \begin{bmatrix} \bar{\boldsymbol{d}} \\ \hat{\boldsymbol{d}} \end{bmatrix} = \begin{bmatrix} \bar{\boldsymbol{f}} \\ \hat{\boldsymbol{f}} \end{bmatrix} = \boldsymbol{f} \tag{5.20}$$

where $\bar{\boldsymbol{d}} \in \mathbb{R}^{2\bar{N}\times 1}$ and $\hat{\boldsymbol{d}} \in \mathbb{R}^{2\hat{N}\times 1}$ are coefficient vectors to be determined. The stiffness matrix $\boldsymbol{K} \in \mathbb{R}^{N\times N}$ is a positive definite matrix, where $N = 2(\bar{N} + \hat{N})$. The sub-matrix $\bar{\boldsymbol{K}} \in \mathbb{R}^{2\bar{N}\times 2\bar{N}}$ is a sparse matrix, $\hat{\boldsymbol{K}} \in \mathbb{R}^{2\bar{N}\times 2\hat{N}}$ and $\hat{\boldsymbol{K}} \in \mathbb{R}^{2\hat{N}\times 2\hat{N}}$ are the other sub-matrices obtained by the

following,

$$\begin{aligned}\begin{bmatrix} \bar{\boldsymbol{K}}_{(2I-1)(2J-1)} & \bar{\boldsymbol{K}}_{(2I-1)(2J)} \\ \bar{\boldsymbol{K}}_{(2I)(2J-1)} & \bar{\boldsymbol{K}}_{(2I)(2J)} \end{bmatrix} &= \int_{\Omega} \bar{\boldsymbol{B}}_I^{\mathrm{T}} \boldsymbol{C} \bar{\boldsymbol{B}}_J \, \mathrm{d}\Omega \\ &\quad - \int_{\Gamma_{g_k}} \left(\Psi_I \boldsymbol{e}_k \boldsymbol{e}_k^{\mathrm{T}} \boldsymbol{N} \boldsymbol{C} \bar{\boldsymbol{B}}_J + \bar{\boldsymbol{B}}_I^{\mathrm{T}} \boldsymbol{C}^{\mathrm{T}} \boldsymbol{N}^{\mathrm{T}} \boldsymbol{e}_k \boldsymbol{e}_k^{\mathrm{T}} \Psi_J \right) \, \mathrm{d}\Gamma \\ &\quad + \beta \int_{\Gamma_{g_k}} \Psi_I \Psi_J \boldsymbol{e}_k \boldsymbol{e}_k^{\mathrm{T}} \, \mathrm{d}\Gamma \end{aligned} \tag{5.21}$$

$$\begin{aligned}\begin{bmatrix} \hat{\boldsymbol{K}}_{(2I-1)(2J-1)} & \hat{\boldsymbol{K}}_{(2I-1)(2J)} \\ \hat{\boldsymbol{K}}_{(2I)(2J-1)} & \hat{\boldsymbol{K}}_{(2I)(2J)} \end{bmatrix} &= \int_{\bar{\Gamma}_{h_k}} \boldsymbol{F}_I \boldsymbol{e}_k \boldsymbol{e}_k^{\mathrm{T}} \boldsymbol{N} \boldsymbol{C} \hat{\boldsymbol{B}}_J \, \mathrm{d}\Gamma - \int_{\bar{\Gamma}_{g_k}} \hat{\boldsymbol{B}}_I^{\mathrm{T}} \boldsymbol{C}^{\mathrm{T}} \boldsymbol{N}^{\mathrm{T}} \boldsymbol{e}_k \boldsymbol{e}_k^{\mathrm{T}} \boldsymbol{F}_J \, \mathrm{d}\Gamma \\ &\quad + \beta \int_{\bar{\Gamma}_{g_k}} \boldsymbol{F}_I \boldsymbol{e}_k \boldsymbol{e}_k^{\mathrm{T}} \boldsymbol{F}_J \, \mathrm{d}\Gamma \end{aligned} \tag{5.22}$$

and

$$\begin{aligned}\begin{bmatrix} \hat{\boldsymbol{K}}_{(2I-1)(2J-1)} & \hat{\boldsymbol{K}}_{(2I-1)(2J)} \\ \hat{\boldsymbol{K}}_{(2I)(2J-1)} & \hat{\boldsymbol{K}}_{(2I)(2J)} \end{bmatrix} &= \int_{\bar{\Gamma}_{h_k}} \Psi_I \boldsymbol{e}_k \boldsymbol{e}_k^{\mathrm{T}} \boldsymbol{N} \boldsymbol{C} \hat{\boldsymbol{B}}_J \, \mathrm{d}\Gamma - \int_{\bar{\Gamma}_{g_k}} \bar{\boldsymbol{B}}_I^{\mathrm{T}} \boldsymbol{C}^{\mathrm{T}} \boldsymbol{N}^{\mathrm{T}} \boldsymbol{e}_k \boldsymbol{e}_k^{\mathrm{T}} \boldsymbol{F}_J \, \mathrm{d}\Gamma \\ &\quad + \beta \int_{\bar{\Gamma}_{g_k}} \Psi_I \boldsymbol{e}_k \boldsymbol{e}_k^{\mathrm{T}} \boldsymbol{F}_J \, \mathrm{d}\Gamma \end{aligned} \tag{5.23}$$

where

$$\boldsymbol{N} = \begin{bmatrix} n_1 & 0 & n_2 \\ 0 & n_2 & n_1 \end{bmatrix} \tag{5.24}$$

Here, $\boldsymbol{N}$ is a matrix containing the components of the vector $\boldsymbol{n}$ normal to the boundary where the integral is evaluated and $\boldsymbol{e}_k$ is the unit vector in the direction of the imposition of the boundary condition, where k corresponds to the direction of the prescribed displacement at the essential boundary, $k = 1$ corresponds to the normal component and $k = 2$ corresponds to the tangential component. The sub-vectors in $\boldsymbol{f} \in \mathbb{R}^{N \times 1}$ in (25) are

$$\left\{ \bar{\boldsymbol{f}} \right\}_I = \int_{\bar{\Gamma}_{h_k}} \Psi_I \boldsymbol{e}_k h_k \, \mathrm{d}\Gamma - \int_{\bar{\Gamma}_{g_k}} \left(-\beta \Psi_I \boldsymbol{e}_k g_k + \bar{\boldsymbol{B}}_I^{\mathrm{T}} \boldsymbol{C}^{\mathrm{T}} \boldsymbol{N}^{\mathrm{T}} \boldsymbol{e}_k g_k \right) \, \mathrm{d}\Gamma \tag{5.25}$$

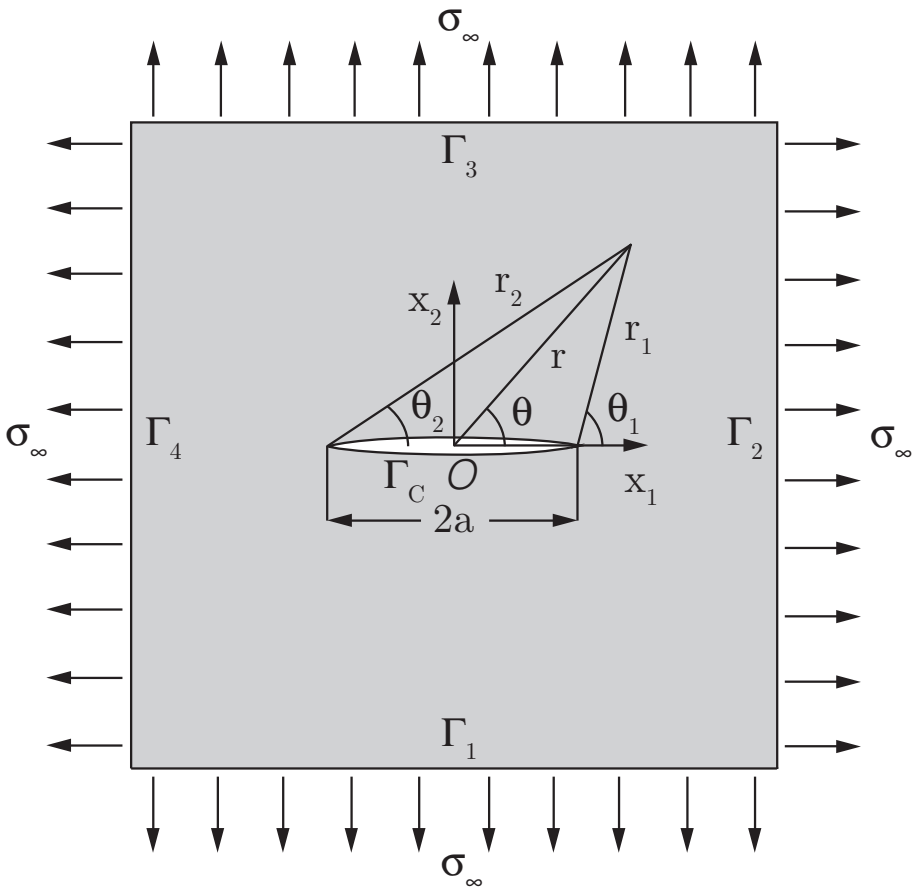

Figure 5.7: Loaded line crack model

and

$$\left\{\hat{\boldsymbol{f}}\right\}_I = \int_{\bar{\Gamma}_{h_k}} \boldsymbol{F}_I^{\mathrm{T}} \boldsymbol{e}_k h_k \, \mathrm{d}\Gamma - \int_{\bar{\Gamma}_{g_k}} \left(-\beta \boldsymbol{F}_I^{\mathrm{T}} \boldsymbol{e}_k g_k + \hat{\boldsymbol{B}}_I^{\mathrm{T}} \boldsymbol{C}^{\mathrm{T}} \boldsymbol{N}^{\mathrm{T}} \boldsymbol{e}_k g_k\right) \mathrm{d}\Gamma \tag{5.26}$$

5.2.4 Numerical Example

The following example is a line crack in an infinite medium subjected to hydrostatic tension at infinity, shown in Figure 5.7.

The exact solution of this problem is derived from the complex variable approach [England,

2003] with the use of Westergaard's stress function [Westergaard, 1997] given by

$$\boldsymbol{u} = \begin{cases} u_1 & = \frac{\kappa-1}{4\mu}\sigma_\infty \left(r_1 r_2\right)^{1/2} \cos\left(\frac{\theta_1+\theta_2}{2}\right) - \frac{\sigma_\infty r^2}{\left(r_1 r_2\right)^{1/2}} \sin\theta \sin\left(\theta - \frac{\theta_1+\theta_2}{2}\right) \\ u_2 & = \frac{\kappa+1}{4\mu}\sigma_\infty \left(r_1 r_2\right)^{1/2} \sin\left(\frac{\theta_1+\theta_2}{2}\right) - \frac{\sigma_\infty r^2}{\left(r_1 r_2\right)^{1/2}} \sin\theta \cos\left(\theta - \frac{\theta_1+\theta_2}{2}\right) \end{cases} \tag{5.27}$$

where κ is the Kolosov constant defined previously and $\mu = E/(2(1+\nu))$ is the shear modulus. The analytical stresses $\boldsymbol{\sigma} = \left\{ \sigma_{11} \quad \sigma_{22} \quad \sigma_{12} \right\}^{\mathrm{T}}$ can also be derived and are given as follows

$$\boldsymbol{\sigma} = \begin{cases} \sigma_{11} & = \sigma_\infty \left\{ \frac{r}{\left(r_1 r_2\right)^{1/2}} \cos\left(\theta - \frac{\theta_1+\theta_2}{2}\right) - \frac{a^2 r}{\left(r_1 r_2\right)^{3/2}} \sin\theta \sin\left(\frac{3(\theta_1+\theta_2)}{2}\right) \right\} \\ \sigma_{22} & = \sigma_\infty \left\{ \frac{r}{\left(r_1 r_2\right)^{1/2}} \cos\left(\theta - \frac{\theta_1+\theta_2}{2}\right) + \frac{a^2 r}{\left(r_1 r_2\right)^{3/2}} \sin\theta \sin\left(\frac{3(\theta_1+\theta_2)}{2}\right) \right\} \\ \sigma_{12} & = \sigma_\infty \frac{a^2 r}{\left(r_1 r_2\right)^{3/2}} \sin\theta \cos\left(\frac{3(\theta_1+\theta_2)}{2}\right) \end{cases} \tag{5.28}$$

The analytical value of the stress intensity factor K_I is given as

$$K_I = \sigma_0 \sqrt{\pi a} \tag{5.29}$$

The geometry and boundary condition of this problem are symmetrical about the crack surface. Therefore, only the symmetric enrichment basis functions $\boldsymbol{F}_m^{\mathrm{sym}}$ in (5.15a) from the local asymptotic solution is considered to avoid polluting the solution with the anti-symmetric basis functions. Considering the symmetry of this problem, a half model of this problem is modeled as shown in Figure 5.8. The penalty parameter in the Nitsche's method for imposition of essential boundary condition can influence the opening of the crack when displacement are prescribed near the crack surfaces. To limit the influence of the penalty parameter on the crack opening, traction is prescribed on $\Gamma_1 \cup \Gamma_3 \cup \Gamma_4$ and the displacement is imposed in both x_1 and x_2 directions on the boundary Γ_2 on the right. The value of these boundary conditions is obtained from the analytical solution from (5.27) and (5.28).

Consider the specimen with dimension $100\,\mathrm{mm} \times 100\,\mathrm{mm}$ with a middle crack of length

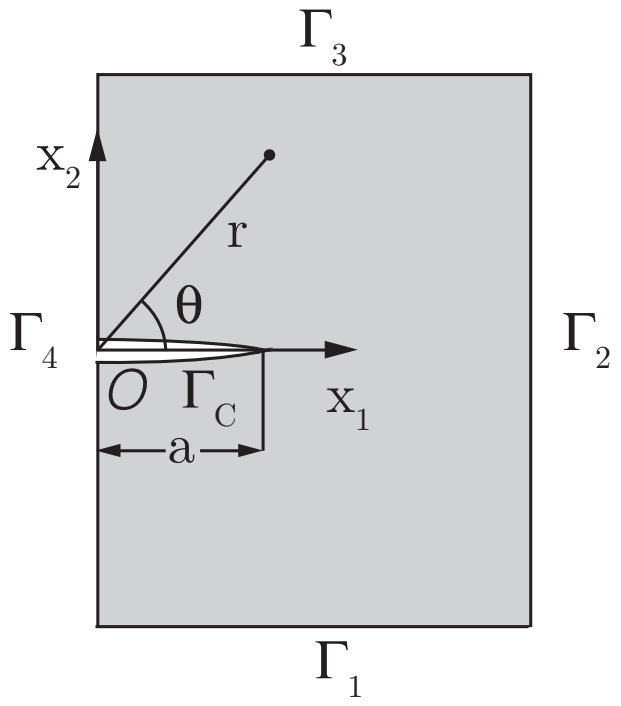

Figure 5.8: Half model for the study of the loaded line crack

$a = 50$ mm. The specimen is made of borosilicate glass, with properties $E = 64,000$ N/mm^2 and $\nu = 0.2$. The fracture toughness of the material considered in this example is obtained from experimental study [Wiederhorn, 1969] and is given as $K_C = 0.77$ N/m$^{3/2}$. The magnified deformed shape of the sample obtained from the exact solution in (5.27) is shown in Figure 5.9.

The relative errors in H^1 seminorm of $\boldsymbol{u}$ and the relative absolute error in SIF are respectively denoted as follows

$$e_{s1} = \frac{|\boldsymbol{u} - \boldsymbol{u}^h|_{H^1}}{|\boldsymbol{u}|_{H^1}}, \quad e_{KI} = \frac{|K_I - K_I^h|}{|K_I|} \tag{5.30}$$

Figures 5.10 and 5.11 present the errors in both L^2 norm and H^1 seminorm of the solutions from standard Galerkin and ISBFM Galerkin formulations. Those solutions are obtained using a 48×48 uniform discretization ($\bar{N} = 4608$) with one, two and three enrichment functions ($\hat{N} = 1, 2, 3$) and RK approximation with linear order basis and cubic-B spline kernel function. Different orders of Gaussian quadrature for the domain and boundary integrals are investigated. The ISBFM Galerkin formulation can achieve good accuracy by using lower order of Gaussian quadrature, such as 2×2

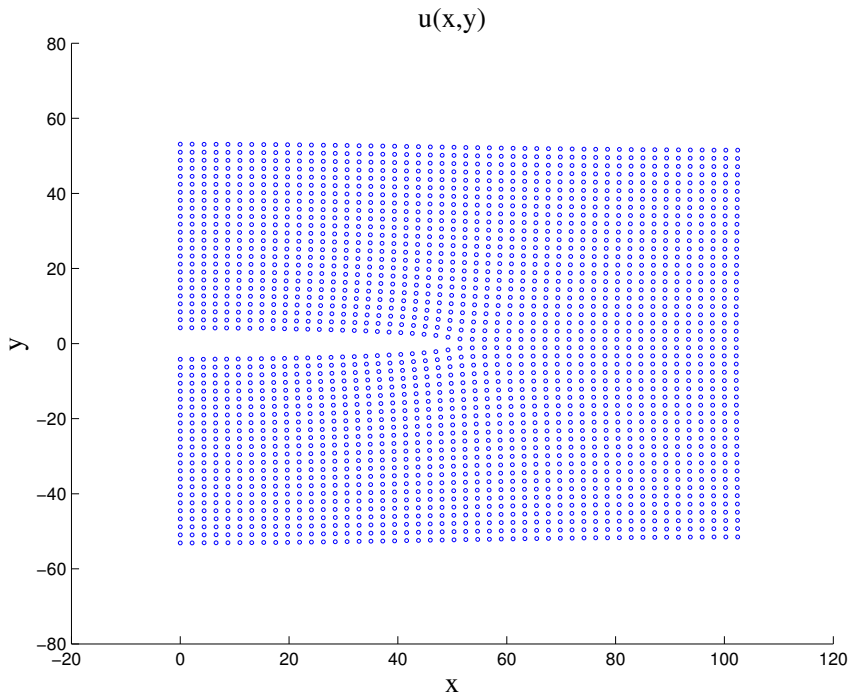

Figure 5.9: Magnified deformation obtained from the exact solution of the loaded line

or 4×4, while 12×12 Gaussian quadrature rule is needes in the standard Galerkin method for a similar accuracy.

The distributions of the absolute errors of solutions over the domain are compared in Figure 5.12 where 8th order of Gaussian quadrature has been used in the Galerkin formulations. The results show that the numerical solution is improved by the ISBFM Galerkin formulation in the entire domain compared to the standard Galerkin method. The error in the ISBFM Galerkin method is localized around the crack tip which can be further enhanced using more enrichment functions in the approximation.

The relative absolute errors in SIF from the standard and ISBFM Galerkin approximations are shown in Figure 5.13. The SIFs are calculated according to (5.4) where the strain energy release rate G is obtained from the evaluation of the numerical J-integral from (5.6). The exact SIF for this example given by (5.29) is $K = 12.53$ N/mm$^{3/2}$.

For different numbers of Gauss points (GP) for the numerical integrations, the convergence

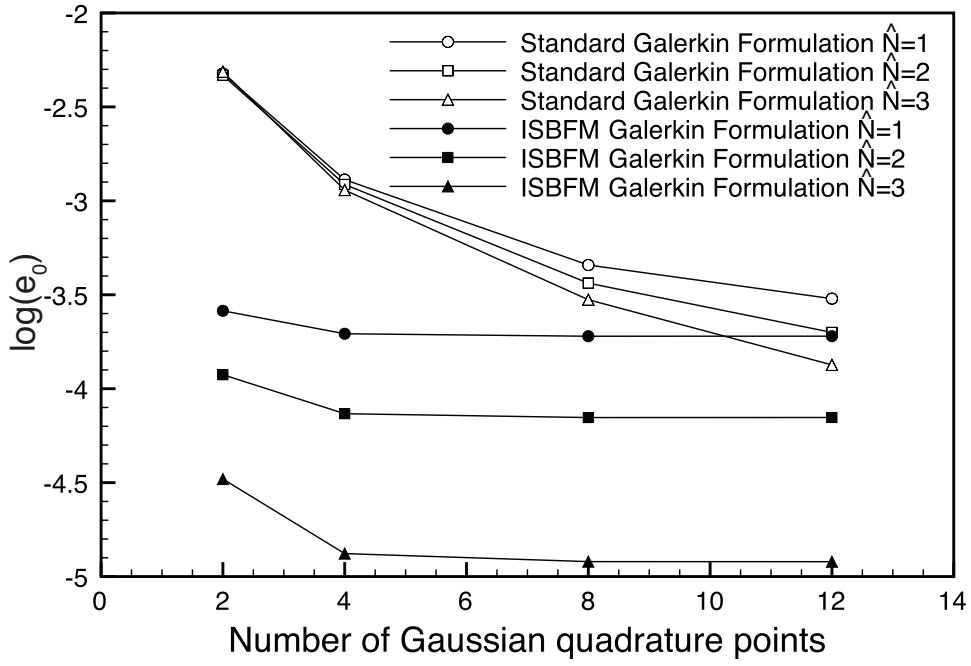

Figure 5.10: Relative error in L^2 norm of approximations of loaded line crack solution under different Galerkin formulations and different orders of Gaussian quadrature

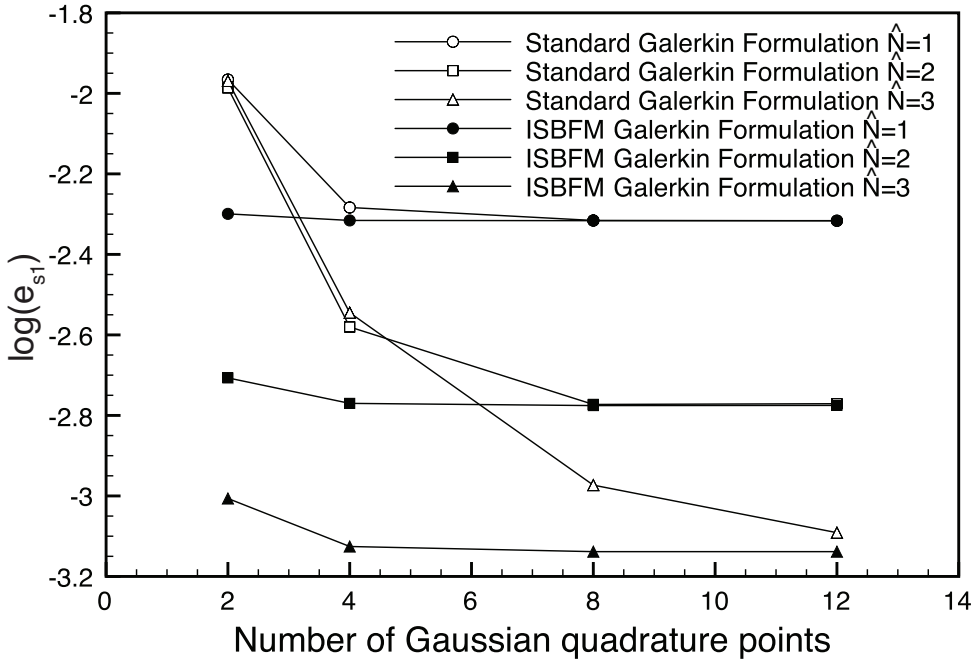

Figure 5.11: Relative error in H^1 seminorm of approximations of loaded line crack solution under different Galerkin formulations and different orders of Gaussian quadrature

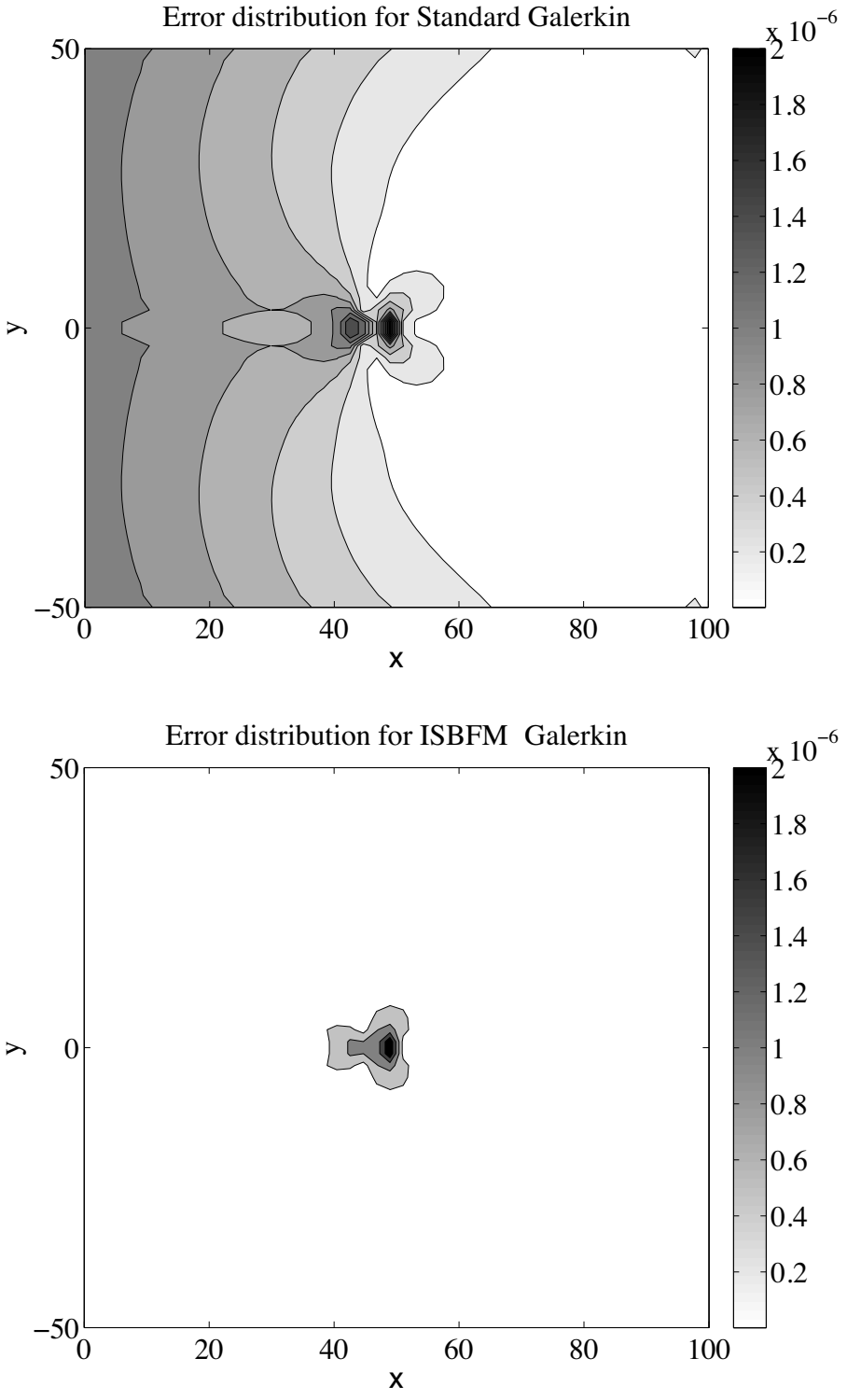

Figure 5.12: Absolute error distribution of solutions from standard and ISBFM Galerkin formulations

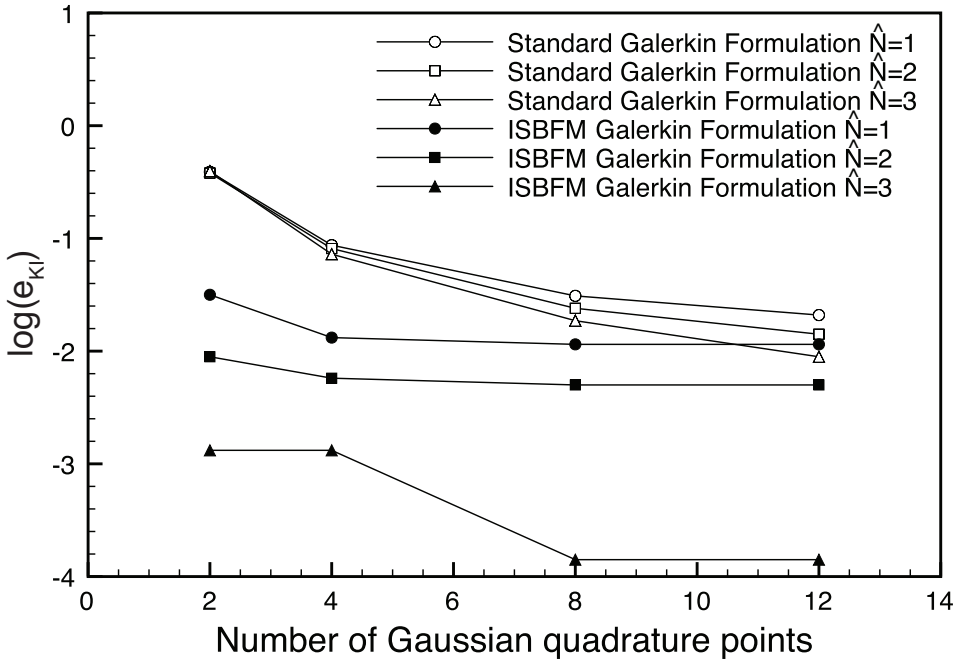

Figure 5.13: Relative absolute error of the stress intensity factors under different Galerkin formulations and different orders of Gaussian quadrature

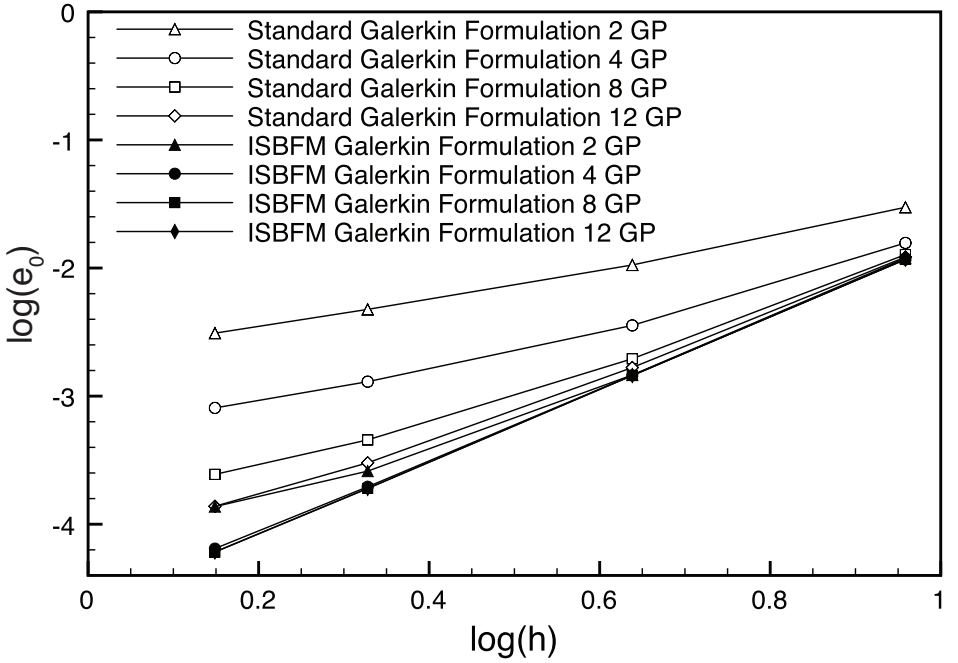

Figure 5.14: Convergence plot in relative L^2 error norm of standard and ISBFM Galerkin formulations with different orders of Gaussian quadrature

Table 5.1: Rate of Convergence in L^2 norm of standard and ISBFM Galerkin formulations with different orders of Gaussian quadrature

	Standard Galerkin				ISBFM Galerkin			
Orders of Gaussian Quadrature	2	4	8	12	2	4	8	12
Rate of Convergence	1.04	1.14	1.50	1.89	1.55	2.69	2.77	2.77

plots of standard and ISBFM Galerkin formulations in relative L^2 error norm are shown in Figure 5.14 and Table 5.1 shows the corresponding asymptotic rates of convergence. The ISBFM Galerkin formulation improve the accuracy of the approximation but also the rate of convergence.

This example demonstrates that the selection of proper enrichment basis and ISBFM Galerkin formulation are critical to the effectiveness of the numerical solution. The ISBFM Galerkin formulation will be considered to construct the full scale model for the proposed MOR methods for LEFM problems presented in the next chapter.

Chapter 6

ISBFM Galerkin based MOR Methods for Linear Elastic Fracture Mechanics

6.1 Preliminaries

The two MOR methods for problems with discontinuities introduced in Chapter 4 are extended to LEFM. The following section first extends the formulation of ISBFM-UR and ISBFM-DR methods to two-dimensional fracture problems. The performance of the reduced models is then investigated for a loaded line crack example at the end of this chapter. A detail analysis of the accuracy, stability and efficiency of the MOR approaches is presented in Chapter 7.

6.2 Reduced Models for LEFM

Consider a discrete system $\boldsymbol{K}\boldsymbol{d} = \boldsymbol{f}$ defined in (5.20) in Chapter 5, and recall the expression of a reduced order model of dimension $k \leq N = 2(\bar{N} + \hat{N})$, we have

$$\boldsymbol{K}^r \boldsymbol{d}^r = \boldsymbol{f}^r \tag{6.1}$$

where k is the order of reduction, $\boldsymbol{K}^r \in \mathbb{R}^{k\times k}$ is the reduced stiffness matrix, $\boldsymbol{f}^r \in \mathbb{R}^{k\times 1}$ is the reduced force vector and $\boldsymbol{d}^r \in \mathbb{R}^{k\times 1}$ is the reduced coefficient vector. ISBFM-UR and ISBFM-DR presented in 4 are extended for reduced order modeling of a 2D enriched solution for fracture problems in the followings.

Recall ISBFM-UR, where a single projection $\boldsymbol{P} \in \mathbb{R}^{N\times k}$ is applied to all DOF and the reduced system is defined as

$$\boldsymbol{K}^{ur}\boldsymbol{d}^{ur} = \boldsymbol{f}^{ur}, \quad \boldsymbol{K}^{ur} = \boldsymbol{P}^T\boldsymbol{K}\boldsymbol{P}, \quad \boldsymbol{f}^{ur} = \boldsymbol{P}^T\boldsymbol{f} \tag{6.2}$$

where $\boldsymbol{d}^{ur}$ is the reduced coefficient vector, $\boldsymbol{K}^{ur}$ is the reduced stiffness matrix and $\boldsymbol{f}^{ur}$ is the reduced force vector.

In ISBFM-DR, the reduced coefficient vector $\boldsymbol{d}^{dr} \in \mathbb{R}^{k\times 1}$ constitutes of $\bar{\boldsymbol{d}}^{dr} \in \mathbb{R}^{\bar{k}\times 1}$ and $\hat{\boldsymbol{d}}^{dr} \in \mathbb{R}^{\hat{k}\times 1}$. Similar to that of the Laplace problem, the decomposed projection matrix is defined as follows

$$\begin{bmatrix} \bar{\boldsymbol{P}} & \boldsymbol{0} \\ \boldsymbol{0} & \hat{\boldsymbol{P}} \end{bmatrix} \in \mathbb{R}^{(2\bar{N}+2\hat{N})\times(\bar{k}+\hat{k})} \tag{6.3}$$

where $\bar{\boldsymbol{P}} \in \mathbb{R}^{2\bar{N}\times\bar{k}}$ is the projection of all smooth DOF and $\hat{\boldsymbol{P}} \in \mathbb{R}^{2\hat{N}\times\hat{k}}$ is the projection of all non-smooth DOF by considering the separate enrichment functions in different directions for LEFM as discussed in Chapter 5. The reduced dimension is $k = \bar{k} + \hat{k}$, with $\bar{k} \leq 2\bar{N}$ and $\hat{k} \leq 2\hat{N}$. The reduced system is given as

$$\boldsymbol{K}^{dr}\boldsymbol{d}^{dr} = \boldsymbol{f}^{dr} \tag{6.4}$$

with

$$\boldsymbol{K}^{dr} = \begin{bmatrix} \bar{\boldsymbol{K}}^{dr} & \hat{\boldsymbol{K}}^{dr} \\ \hat{\boldsymbol{K}}^{dr\mathrm{T}} & \hat{\boldsymbol{K}}^{dr} \end{bmatrix}, \quad \boldsymbol{d}^{dr} = \begin{bmatrix} \bar{\boldsymbol{d}}^{dr} \\ \hat{\boldsymbol{d}}^{dr} \end{bmatrix}, \quad \boldsymbol{f}^{dr} = \begin{bmatrix} \bar{\boldsymbol{f}}^{dr} \\ \hat{\boldsymbol{f}}^{dr} \end{bmatrix} \tag{6.5}$$

where the sub-matrices are defined as $\bar{\boldsymbol{K}}^{dr} = \bar{\boldsymbol{P}}^T\bar{\boldsymbol{K}}\bar{\boldsymbol{P}} \in \mathbb{R}^{\bar{k}\times\bar{k}}$, $\hat{\boldsymbol{K}}^{dr} = \bar{\boldsymbol{P}}^T\hat{\boldsymbol{K}}\hat{\boldsymbol{P}} \in \mathbb{R}^{\bar{k}\times\hat{k}}$ and $\hat{\boldsymbol{K}}^{dr} = \hat{\boldsymbol{P}}^T\hat{\boldsymbol{K}}\hat{\boldsymbol{P}} \in \mathbb{R}^{\hat{k}\times\hat{k}}$ and the sub-vectors are $\bar{\boldsymbol{f}}^{dr} = \bar{\boldsymbol{P}}^T\bar{\boldsymbol{f}} \in \mathbb{R}^{\bar{k}\times 1}$ and $\hat{\boldsymbol{f}}^{dr} = \hat{\boldsymbol{P}}^T\hat{\boldsymbol{f}} \in \mathbb{R}^{\hat{k}\times 1}$.

The construction of the projection matrices $\boldsymbol{P}$, $\bar{\boldsymbol{P}}$ and $\hat{\boldsymbol{P}}$ involves modal analysis of the fine scale system and a statically reduced system. It has been described in detail in Chapter 4 and will not be repeated in this section. We note that the parameter for Nitsche's method for imposing essential boundary conditions has noticable influence on the eigen-spectrum of the fine system and thus affects the characteristics of the projected reduced order system as will be observed in the study of numerical examples.

6.3 Numerical Example and Discussions

In this section, the proposed MOR methods, ISBFM-UR and ISBFM-DR, are applied to the model order reduction of a medium with a line crack subjected to hydrostatic tension at infinity as presented in Section 5.2.4. This is the same problem as shown in Figure 5.8 in the previous chapter and symmetry is considered. A finite dimension of 100 mm $\times$ 100 mm of a brittle material with $E = 64,000$ N/mm^2, $\nu = 0.2$ and middle crack of length $a = 50$ mm is modeled using the proposed MOR methods. The boundary conditions on the boundaries of the finite domain are also identical to those defined in Section 5.2.4.

The fine scale solution is obtained from ISBFM Galerkin formulation using a 48×48 uniform discretization with one symmetric enrichment function $\boldsymbol{F}_1^{sym}$ from (5.15a) ($\hat{N} = 1$), composed of different basis for each displacement component, and the numerical integrals are evaluated using 8th order Gaussian quadrature. The numerical results of the fine scale solution were presented in Section 5.2.4. In this study, the reduced solutions from ISBFM-DR are obtained with $\hat{k} = \hat{N}$, where the projection is only applied to the smooth part of the approximation.

Figure 6.1 presents the distribution of the error in Euclidian norm between the fine scale solution and the approximated reduced solutions obtained from ISBFM-UR and ISBFM-DR, with different percentage of reduction $k/N = 1\%, 4\%, 9\%$. First, it is shown that the error of the reduced solutions from ISBFM-DR is smaller than the one from ISBFM-UR. It is observed that the error is concentrated near the boundary on the right, especially for the reduced solution of ISBFM-UR.

Table 6.1: Relative error in SIF of the reduced solutions for $k/N = 1\%, 4\%, 9\%, 20\%, 40\%$

	Relative error in SIF				
k/N	1%	4%	9%	20%	40%
ISBFM-UR	$1.16\ 10^{-1}$	$2.16\ 10^{-2}$	$2.80\ 10^{-2}$	$3.29\ 10^{-2}$	$4.81\ 10^{-2}$
ISBFM-DR	$2.77\ 10^{-2}$	$1.93\ 10^{-2}$	$1.41\ 10^{-2}$	$1.27\ 10^{-2}$	$1.18\ 10^{-2}$

This boundary corresponds to the boundary where non-homogeneous displacement is prescribed and it causes an issue for the reduced solution from ISBFM-UR. Indeed, the eigenmodes used for this projection correspond to the lowest eigenvalues of the fine scale system and are homogeneous on the essential boundary. The eigenmodes that are non-zero on this boundary correspond to higher eigenvalues. Therefore, the reduced solution from ISBFM-UR is obtained from only the lowest eigenmodes incapable of representing the non-homogeneous prescribed displacement. On the contrary, the reduced solution from ISBFM-DR is obtained from a decomposed projection. The combination of both reduced smooth solution and enriched solution are forced to meet the essential boundary condition. Under this ISBFM-DR MOR, the eigenmodes used to project the smooth part of solution are non-zero on the essential boundary, which allows the reduced solution to properly represent the prescribed non-homogeneous displacements. The deformation from the reduced solutions of both proposed MOR methods for a percentage of reduction $k/N = 9\%$ are compared to the deformation of the fine scale solution as shown in Figure 6.2. As expected from the error distribution plots in Figure 6.1, the reduced solution from ISBFM-UR does not perform as well as the one from ISBFM-DR, especially near the essential boundary on the right.

A comparison of SIF of both ISBFM-UR and ISBFM-DR methods with the analytical SIF $K = 12.53$ N/mm$^{3/2}$ from (5.29) is given in Table 6.1. This table presents the relative error in SIF of the reduced solutions from ISBFM-UR and ISBFM-DR with different percentage of reduction $k/N = 1\%, 4\%, 9\%, 20\%, 40\%$ and shows as the size of the reduced model is increased, the SIF from ISBFM-DR converges to the full SIF whereas the one from ISBFM-UR does not converge.

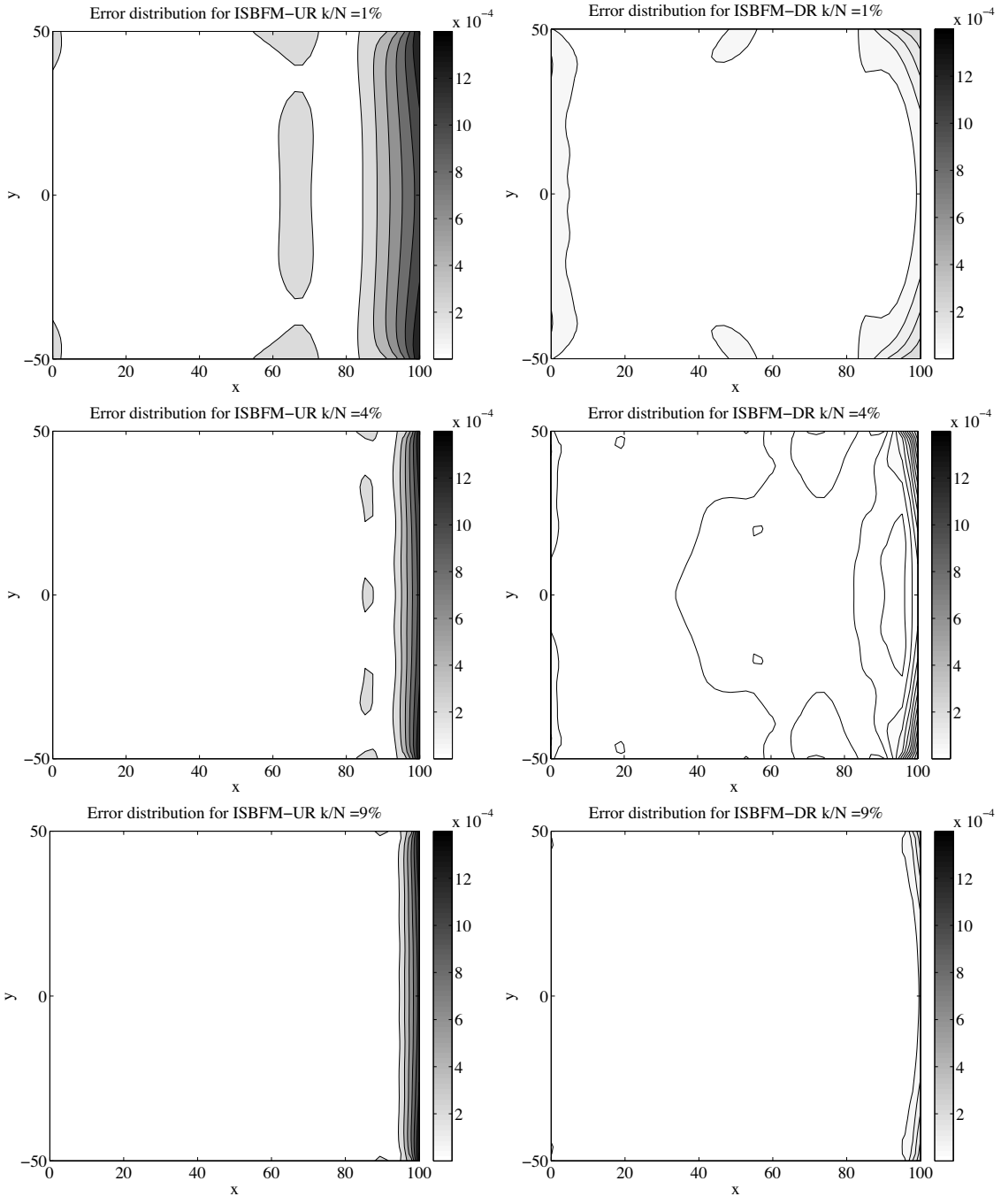

Figure 6.1: Error distribution in Euclidian norm of ISBFM-UR and ISBFM-DR for different percentage of reduction $k/N = 1\%, 4\%, 9\%$

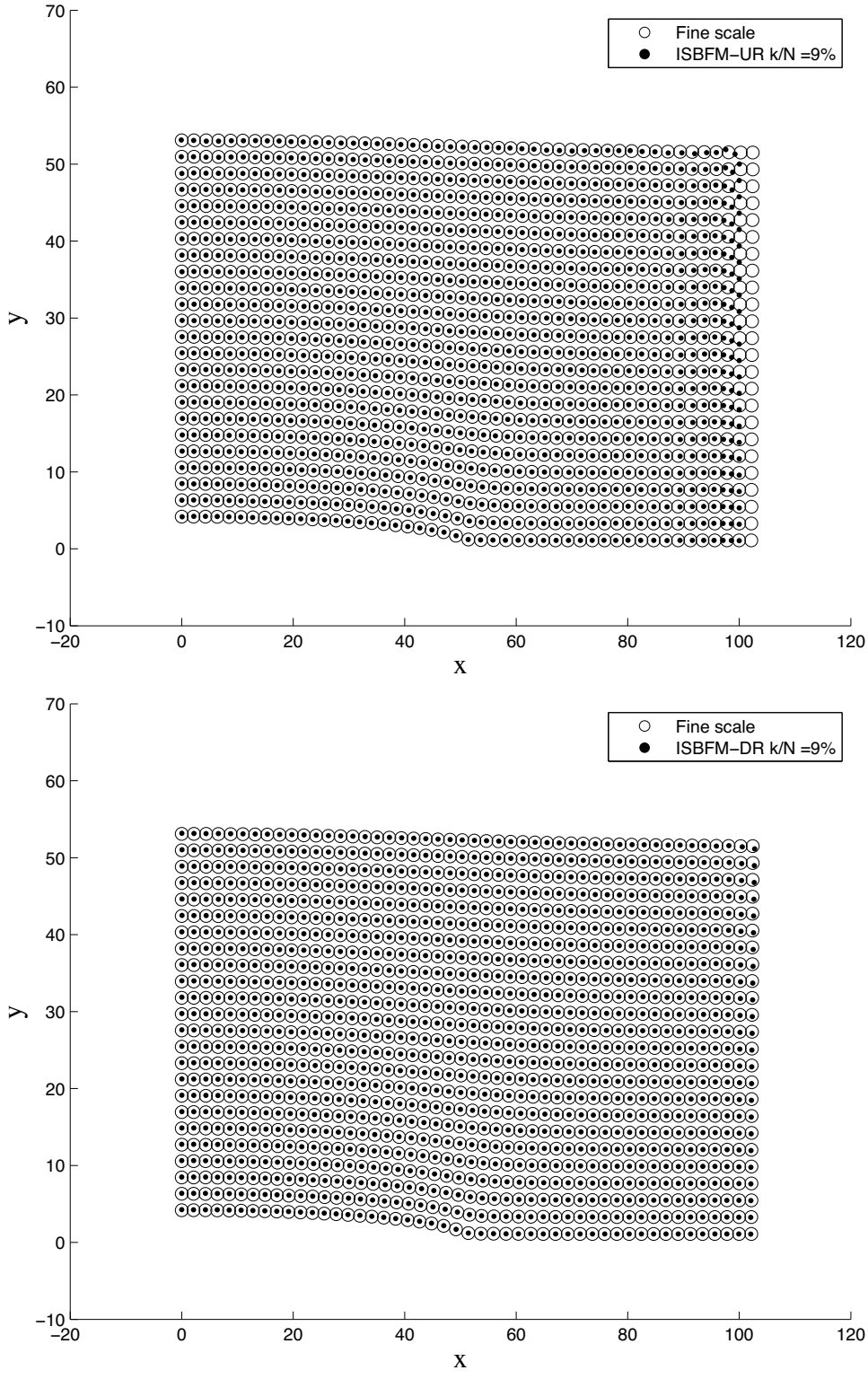

Figure 6.2: Deformations from fine scale and reduced solutions from ISBFM-UR and ISBFM-DR for a percentage of reduction $k/N = 9\%$

Chapter 7

Accuracy, Stability and Complexity Analysis of the Proposed ISBFM based MOR Methods

7.1 Preliminaries

The proposed ISBMF-UR and ISBGM-DR MOR methods presented in Chapters 4 and 6 are further investigated in this chapter A detailed error analysis of these MOR approaches is first provided, followed by the stability analysis of the reduced models. The operational counts of the two proposed MOR methods are also presented, and the efficiency comparison of the MOR methods is reported.

7.2 Error Bound Estimation of the Reduced Solutions

For ISBFM-UR, let $\boldsymbol{\Phi}^{\mathrm{T}} = \{\boldsymbol{\Psi}^{\mathrm{T}}, \boldsymbol{F}^{\mathrm{T}}\}$ be the collection of RK shape functions $\boldsymbol{\Psi}$ and enrichment functions $\boldsymbol{F}$, and let $\boldsymbol{\Phi}^{ur\mathrm{T}}$ be the projected basis functions from fine scale basis functions $\boldsymbol{\Phi}^{\mathrm{T}}$ i.e., $\boldsymbol{\Phi}^{ur\mathrm{T}} = \boldsymbol{\Phi}^{\mathrm{T}}\boldsymbol{P}$. It follows that the reduced solution is $u^{ur} = \boldsymbol{\Phi}^{ur\mathrm{T}}\boldsymbol{d}^{ur}$. The solution error in vector

sup-norm between the full model and the reduced model is given by

$$\begin{aligned}\left\|u^h - u^{ur}\right\|_\infty &= \left\|\boldsymbol{\Phi}^{\mathrm{T}}\boldsymbol{d} - \boldsymbol{\Phi}^{ur\mathrm{T}}\boldsymbol{d}^{ur}\right\|_\infty \\ &\leq \|\boldsymbol{\Phi}\|_\infty \left\|\boldsymbol{d} - \boldsymbol{P}\boldsymbol{d}^{ur}\right\|_\infty \\ &\leq \|\boldsymbol{\Phi}\|_\infty \max_{i\in G}\left|\frac{\boldsymbol{\phi}_i^{\mathrm{T}}\boldsymbol{f}}{\lambda_i}\right|\end{aligned} \tag{7.1}$$

where $G = \{k+1, \ldots, N\}$ is a set of indices of the eigenpairs in $\{\boldsymbol{\phi}_i, \lambda_i\}_{i=1}^N$ satisfying the eigensystem $\boldsymbol{K}\boldsymbol{\phi}_i = \lambda_i\boldsymbol{\phi}_i$ that have been truncated in the projection to the reduced system, and $\|\cdot\|_\infty$ is defined for a matrix $\boldsymbol{X} = (X_{ij})_{1<i<M, 1<j<N}$ as

$$\|\boldsymbol{X}\|_\infty = \max_{1\leq i\leq M}\sum_{j=1}^{N}|X_{ij}| \tag{7.2}$$

By using the Schwarz inequality and the pairwise orthonormal eigenvectors, we have

$$\begin{aligned}\max_{i\in G}\left|\frac{\boldsymbol{\phi}_i^{\mathrm{T}}\boldsymbol{f}}{\lambda_i}\right| &\leq \max_{i\in G}\frac{\|\boldsymbol{\phi}_i^{\mathrm{T}}\|_2\,\|\boldsymbol{f}\|_2}{|\lambda_i|} \\ &\leq \sqrt{N}\frac{\|\boldsymbol{f}\|_\infty}{\lambda_{k+1}}\end{aligned} \tag{7.3}$$

where λ_{k+1} is the smallest eigenvalue beyond the selected eigenpairs $\{\boldsymbol{\phi}_i, \lambda_i\}_{i=1}^k$ that form the projection matrix. The error bound for the ISBFM-UR is expressed as

$$\left\|u^h - u^{ur}\right\|_\infty \leq \sqrt{N}\lambda_{k+1}^{-1}\,\|\boldsymbol{\Phi}\|_\infty\,\|\boldsymbol{f}\|_\infty \tag{7.4}$$

It can be observed that the solution error is related to the smallest remaining eigenvalues not considered in the construction of the projection $\boldsymbol{P}$. Note that the error bound in (7.4) would vary when different numerical techniques for the imposition of boundary conditions are used.

Next, we present the error estimation for ISBFM-DR. Recall that the fine scale system $\boldsymbol{K}\boldsymbol{d} = \boldsymbol{f}$

is decoupled as

$$\bar{\boldsymbol{K}}^c\bar{\boldsymbol{d}} = \bar{\boldsymbol{f}}^c, \quad \bar{\boldsymbol{K}}^c = \bar{\boldsymbol{K}} - \hat{\boldsymbol{K}}\hat{\boldsymbol{K}}^{-1}\hat{\boldsymbol{K}}^{\mathrm{T}}, \quad \bar{\boldsymbol{f}}^c = \bar{\boldsymbol{f}} - \hat{\boldsymbol{K}}\hat{\boldsymbol{K}}^{-1}\hat{\boldsymbol{f}} \tag{7.5a}$$

$$\hat{\boldsymbol{K}}\hat{\boldsymbol{d}} = \hat{\boldsymbol{f}}^c, \quad \hat{\boldsymbol{f}}^c = \hat{\boldsymbol{f}} - \hat{\boldsymbol{K}}^{\mathrm{T}}\bar{\boldsymbol{d}} \tag{7.5b}$$

We have the relation between the smooth and non-smooth coefficient vectors:

$$\hat{\boldsymbol{d}} = \hat{\boldsymbol{K}}^{-1}\hat{\boldsymbol{f}}^c = \hat{\boldsymbol{K}}^{-1}(\hat{\boldsymbol{f}} - \hat{\boldsymbol{K}}^{\mathrm{T}}\bar{\boldsymbol{d}}) \tag{7.6}$$

The reduced system (4.23) from ISBFM-DR can be decoupled similarly to that in (4.25). After solving the coefficient vector of the smooth part $\bar{\boldsymbol{d}}^{dr}$, the coefficient vector of non-smooth part $\hat{\boldsymbol{d}}^{dr}$ can be obtained as well, i.e.,

$$\begin{aligned}
\hat{\boldsymbol{d}}^{dr} &= (\hat{\boldsymbol{K}}^{dr})^{-1}(\hat{\boldsymbol{f}}^{dr} - \hat{\boldsymbol{K}}^{dr\mathrm{T}}\bar{\boldsymbol{d}}^{dr}) \\
&= \hat{\boldsymbol{P}}^{+}\hat{\boldsymbol{K}}^{-1}(\hat{\boldsymbol{P}}^{\mathrm{T}})^{+}(\hat{\boldsymbol{P}}^{\mathrm{T}}\hat{\boldsymbol{f}} - \hat{\boldsymbol{P}}^{\mathrm{T}}\hat{\boldsymbol{K}}^{\mathrm{T}}\bar{\boldsymbol{P}}\bar{\boldsymbol{d}}^{dr}) \\
&= \hat{\boldsymbol{P}}^{+}\hat{\boldsymbol{K}}^{-1}\underbrace{(\hat{\boldsymbol{P}}^{\mathrm{T}})^{+}\hat{\boldsymbol{P}}^{\mathrm{T}}}_{1}(\hat{\boldsymbol{f}} - \hat{\boldsymbol{K}}^{\mathrm{T}}\bar{\boldsymbol{P}}\bar{\boldsymbol{d}}^{dr}) \\
&= \hat{\boldsymbol{P}}^{+}\hat{\boldsymbol{K}}^{-1}(\hat{\boldsymbol{f}} - \hat{\boldsymbol{K}}^{\mathrm{T}}\bar{\boldsymbol{P}}\bar{\boldsymbol{d}}^{dr})
\end{aligned} \tag{7.7}$$

where $\hat{\boldsymbol{P}}^{+}$ is the pseudo-inverse of non-square matrix $\hat{\boldsymbol{P}}$. Subtracting $\hat{\boldsymbol{P}}$ times (7.7) from (7.6), it follows that

$$\begin{aligned}
\hat{\boldsymbol{d}} - \hat{\boldsymbol{P}}\hat{\boldsymbol{d}}^{dr} &= \hat{\boldsymbol{K}}^{-1}(\hat{\boldsymbol{f}} - \hat{\boldsymbol{K}}^{\mathrm{T}}\bar{\boldsymbol{d}}) - \hat{\boldsymbol{P}}\hat{\boldsymbol{P}}^{+}\hat{\boldsymbol{K}}^{-1}(\hat{\boldsymbol{f}} - \hat{\boldsymbol{K}}^{\mathrm{T}}\bar{\boldsymbol{P}}\bar{\boldsymbol{d}}^{dr}) \\
&= \hat{\boldsymbol{K}}^{-1}\hat{\boldsymbol{K}}^{\mathrm{T}}(\bar{\boldsymbol{P}}\bar{\boldsymbol{d}}^{dr} - \bar{\boldsymbol{d}})
\end{aligned} \tag{7.8}$$

In a similar way, we have the error estimation for ISBFM-DR as follows

$$\begin{aligned}
\left\|u^h - u^{dr}\right\|_\infty &= \left\|\boldsymbol{\Psi}^{\mathrm{T}}\bar{\boldsymbol{d}} + \boldsymbol{F}^{\mathrm{T}}\hat{\boldsymbol{d}} - (\boldsymbol{\Psi}^{\mathrm{T}}\bar{\boldsymbol{P}}\bar{\boldsymbol{d}}^{dr} + \boldsymbol{F}^{\mathrm{T}}\hat{\boldsymbol{P}}\hat{\boldsymbol{d}}^{dr})\right\|_\infty \\
&\le \|\boldsymbol{\Psi}\|_\infty \left\|\bar{\boldsymbol{d}} - \bar{\boldsymbol{P}}\bar{\boldsymbol{d}}^{dr}\right\|_\infty + \|\boldsymbol{F}\|_\infty \left\|\hat{\boldsymbol{d}} - \hat{\boldsymbol{P}}\hat{\boldsymbol{d}}^{dr}\right\|_\infty \\
&\le \left\{\|\boldsymbol{\Psi}\|_\infty + \|\boldsymbol{F}\|_\infty \left\|\hat{\boldsymbol{K}}^{-1}\hat{\boldsymbol{K}}^{\mathrm{T}}\right\|_\infty\right\} \left\|\bar{\boldsymbol{d}} - \bar{\boldsymbol{P}}\bar{\boldsymbol{d}}^{dr}\right\|_\infty
\end{aligned} \tag{7.9}$$

We can estimate the order of $\|\hat{\boldsymbol{K}}^{-1}\hat{\boldsymbol{K}}^{\mathrm{T}}\|_\infty$ from the definition of entries of sub-matrices given in Chapter 3 for Laplace problems with singularities and from the properties of RK shape functions, $\|\Psi_i\|_\infty \leq C$ and $\|\boldsymbol{\nabla}\Psi_i\|_\infty \leq Ca^{-1}$, where a is the support size of the kernel function. We also consider the regularity of enrichment functions to yield

$$\left[\hat{\boldsymbol{K}}^{-1}\hat{\boldsymbol{K}}^{\mathrm{T}}\right]_{ij} \approx O\left(r^{-\alpha_i}\right) \tag{7.10}$$

where $i = 1, \ldots, \hat{N}$ and

$$\alpha_i = \begin{cases} 2i/3 & \text{for } \Theta = 3\pi/2 \\ i - 1/2 & \text{for } \Theta = 2\pi \end{cases} \tag{7.11}$$

Consequently, we have a bound as follows

$$\left\|\hat{\boldsymbol{K}}^{-1}\hat{\boldsymbol{K}}^{\mathrm{T}}\right\|_\infty \leq \hat{C} \tag{7.12}$$

where $\hat{C}$ is a bounded constant independent to eigenvalues and discretization length scale. Equation (7.9) is further manipulated to yield

$$\begin{aligned} \left\|u^h - u^{dr}\right\|_\infty &\leq \left(\|\boldsymbol{\Psi}\|_\infty + \hat{C}\,\|\boldsymbol{F}\|_\infty\right) \left\|\bar{\boldsymbol{d}} - \bar{\boldsymbol{P}}\bar{\boldsymbol{d}}^{dr}\right\|_\infty \\ &\leq \left(\|\boldsymbol{\Psi}\|_\infty + \hat{C}\,\|\boldsymbol{F}\|_\infty\right) \max_{j\in\bar{G}} \left|\frac{\boldsymbol{\varphi}_j^{\mathrm{T}}\bar{\boldsymbol{f}}^c}{\mu_j}\right| \\ &\leq \sqrt{\bar{N}}\mu_{\bar{k}+1}^{-1}(C + \hat{C}\,\|\boldsymbol{F}\|_\infty) \left\|\bar{\boldsymbol{f}}^c\right\|_\infty \end{aligned} \tag{7.13}$$

where $\bar{G} = \{\bar{k}+1, \ldots, \bar{N}\}$ is the set of indices of the eigenpairs in $\{\boldsymbol{\varphi}_j, \mu_j\}_{j=1}^{\bar{N}}$ associated with the eigensystem $\bar{\boldsymbol{K}}^c\boldsymbol{\varphi}_j = \mu_j\boldsymbol{\varphi}_j$ that are truncated in the construction of the projection matrix $\bar{\boldsymbol{P}}$.

By inclusion principle and interlacing properties [Golub and van Van Loan, 1996], we have the relationship between two sets of eigenvalues λ_i and μ_j for $\boldsymbol{K}$ and $\bar{\boldsymbol{K}}^c$, respectively, as follows

$$\mu_i \leq \lambda_{i+\hat{k}}, \quad \forall i \in \{1, 2, \ldots, \bar{N}\} \tag{7.14}$$

We have the property that $\mu_{\bar{k}+1} \leq \lambda_{k+1}$ and that the values λ_{k+1} and $\mu_{\bar{k}+1}$ are very close when the number of enrichment function $\hat{N}$ is small. The magnitude of $\|\boldsymbol{\Phi}\|_\infty$ and $\hat{C}\|\boldsymbol{F}\|_\infty$ are dependent on the number of enrichment basis used and are usually bounded. In summary, we have error bounds for ISBFM-UR and ISBFM-DR as follows

$$\left\|u^h - u^{ur}\right\|_\infty \leq \bar{C}_1 \sqrt{N} \lambda_{k+1}^{-1} \left\|\boldsymbol{f}\right\|_\infty \tag{7.15}$$

$$\left\|u^h - u^{dr}\right\|_\infty \leq \bar{C}_2 \sqrt{\bar{N}} \mu_{\bar{k}+1}^{-1} \left\|\bar{\boldsymbol{f}}^c\right\|_\infty \tag{7.16}$$

where $\bar{C}_1 = \|\boldsymbol{\Phi}\|_\infty$ and $\bar{C}_2 = C + \hat{C}\|\boldsymbol{F}\|_\infty$. This estimate suggests that the errors of the proposed reduced approximations are greatly influenced by the values of $\|\boldsymbol{f}\|_\infty$ and $\|\bar{\boldsymbol{f}}^c\|_\infty$. The numerical results compared with these error analysis are presented in Section 4.3.

7.3 Stability Analysis of the Reduced Systems

In this section, the stability of the discrete systems obtained from both ISBFM-UR and ISBFM-DR approaches is studied. We first discuss the perturbation properties of the reduced system $\boldsymbol{K}^r \boldsymbol{d}^r = \boldsymbol{f}^r$. If both matrix and right-hand side vector are perturbed, then the solution of reduced system may be expressed as $\boldsymbol{d}^r + \delta \boldsymbol{d}^r$ and satisfies the following equation

$$(\boldsymbol{K}^r + \delta \boldsymbol{K}^r)(\boldsymbol{d}^r + \delta \boldsymbol{d}^r) = (\boldsymbol{f}^r + \delta \boldsymbol{f}^r) \tag{7.17}$$

The following relative perturbation bound relates the perturbation of the solution to the perturbation of the left-hand side matrix and the right-hand side vector as

$$\frac{\|\delta \boldsymbol{d}^r\|}{\|\boldsymbol{d}^r\|} \leq \frac{\left(1 + \frac{\|\delta \boldsymbol{f}^r\|}{\|\boldsymbol{f}^r\|}\right) \frac{\|\delta \boldsymbol{K}^r\|}{\|\boldsymbol{K}^r\|} + \text{cond}(\boldsymbol{K}^r) \frac{\|\delta \boldsymbol{f}^r\|}{\|\boldsymbol{f}^r\|}}{1 - \left(\frac{\|\delta \boldsymbol{K}^r\|^2}{\|\boldsymbol{K}^r\|^2} + (1 + \text{cond}(\boldsymbol{K}^r)) \frac{\|\delta \boldsymbol{K}^r\|}{\|\boldsymbol{K}^r\|}\right)} \tag{7.18}$$

Herein the vector 2-norm is considered, i.e., $\|\cdot\| = \|\cdot\|_2$, and the condition number is defined as

$$\text{cond}(\boldsymbol{K}^r) = \|\boldsymbol{K}^r\| \left\|(\boldsymbol{K}^r)^{-1}\right\| = \frac{\lambda_{\max}(\boldsymbol{K}^r)}{\lambda_{\min}(\boldsymbol{K}^r)} \tag{7.19}$$

We can observe from (7.18) that this condition number plays a key role in the sensitivity of the solution subjected to small perturbations. If the left-hand side matrix is not perturbed i.e. $\delta\boldsymbol{K}^r = 0$, then the bound in (7.18) becomes

$$\frac{\|\delta\boldsymbol{d}^r\|}{\|\boldsymbol{d}^r\|} \leq \text{cond}(\boldsymbol{K}^r)\frac{\|\delta\boldsymbol{f}^r\|}{\|\boldsymbol{f}^r\|} \tag{7.20}$$

A sharper measure of condition numbers has been proposed by Chan and Foulser [Chan and Foulser, 1988], called effective condition number, in which the right-hand side vector is taken into account in defining the conditioning of a linear system, and is given as follows

$$\text{cond}_{\text{eff}}(\boldsymbol{K}^r) = \text{cond}(\boldsymbol{K}^r)\frac{\|\boldsymbol{f}^r\|}{\sqrt{\|\boldsymbol{f}^r\|^2 + (\text{cond}(\boldsymbol{K}^r)^2 - 1)\,\beta_{\min}^2}} \tag{7.21}$$

where $\beta_{\min}$ is an inner product of the eigenvector with respect to smallest eigenvalue $\lambda_{\min}(\boldsymbol{K}^r)$ and the right-hand side vector $\boldsymbol{f}^r$. The corresponding perturbation property has the following bound

$$\frac{\|\delta\boldsymbol{d}^r\|}{\|\boldsymbol{d}^r\|} \leq \frac{1}{1 - \|\boldsymbol{K}^r\|^{-1}\|\delta\boldsymbol{K}^r\|}\left\{\text{cond}(\boldsymbol{K}^r)\frac{\|\delta\boldsymbol{K}^r\|}{\|\boldsymbol{K}^r\|} + \text{cond}_{\text{eff}}(\boldsymbol{K}^r)\frac{\|\delta\boldsymbol{f}^r\|}{\|\boldsymbol{f}^r\|}\right\} \tag{7.22}$$

Similarly, if $\delta\boldsymbol{K}^r = 0$, then we obtain

$$\frac{\|\delta\boldsymbol{d}^r\|}{\|\boldsymbol{d}^r\|} \leq \text{cond}(\boldsymbol{K}^r)\frac{\|\delta\boldsymbol{f}^r\|}{\|\boldsymbol{f}^r\|} \tag{7.23}$$

The investigations of the stability of problems with singularities in terms of effective conditioning number [Huang and Li, 2006] [Hu et al., 2011] reveal that the traditional condition number overestimates the ill-conditioning of the system.

In the following, we investigate the relation between condition numbers of the full system (4.17) and the reduced system (4.18). It can be easily derived that

$$\begin{aligned}\text{cond}(\boldsymbol{K}^r) &= \text{cond}(\boldsymbol{P}^{\mathrm{T}}\boldsymbol{K}\boldsymbol{P}) \\ &= \left\|\boldsymbol{P}^{\mathrm{T}}\boldsymbol{K}\boldsymbol{P}\right\| \left\|(\boldsymbol{P}^{\mathrm{T}}\boldsymbol{K}\boldsymbol{P})^{-1}\right\| \\ &\leq \left\|\boldsymbol{P}^{\mathrm{T}}\right\| \|\boldsymbol{K}\| \|\boldsymbol{P}\| \left\|\boldsymbol{P}^{+}\right\| \left\|\boldsymbol{K}^{-1}\right\| \left\|(\boldsymbol{P}^{+})^{-1}\right\| \\ &\leq \|\boldsymbol{K}\| \left\|\boldsymbol{K}^{-1}\right\| = \text{cond}(\boldsymbol{K})\end{aligned} \tag{7.24}$$

In the above inequality, $\|\boldsymbol{P}\| = \|\boldsymbol{P}^{\mathrm{T}}\| = 1$ has been considered, as the matrix $\boldsymbol{P}$ has orthonormal columns. Similarly, the effective condition numbers of both full and reduced system have the following relation

$$\text{cond}_{\text{eff}}(\boldsymbol{K}^r) \leq \text{cond}_{\text{eff}}(\boldsymbol{K}) \tag{7.25}$$

Next, we consider the reduced matrix $\boldsymbol{K}^r$ in (4.18) obtained from the two MOR methods:

1. ISBFM-UR: $\boldsymbol{K}^r = \boldsymbol{K}^{ur}$ given in (4.20), where the projection $\boldsymbol{P}$ is obtained from $\boldsymbol{K}$ with the eigenpairs $\{\boldsymbol{\phi}_i, \lambda_i\}_{i=1}^{N}$.

2. ISBFM-DR: $\boldsymbol{K}^r = \boldsymbol{K}^{dr}$ given in (4.24), where the sub-projections $\bar{\boldsymbol{P}}$ and $\hat{\boldsymbol{P}}$ are constructed based on $\bar{\boldsymbol{K}}^c$ and $\hat{\boldsymbol{K}}$, with the eigenpairs $\{\boldsymbol{\varphi}_j, \mu_j\}_{j=1}^{\bar{N}}$ and $\{\boldsymbol{\xi}_l, \eta_l\}_{l=1}^{\hat{N}}$, respectively for the decomposed smooth and non-smooth discrete equations.

By means of the Rayleigh quotient [Golub and van Van Loan, 1996] of the reduced stiffness matrix $\boldsymbol{K}^r$, we can derive the bound of condition number for both ISBFM-UR and ISBFM-DR. For ISBFM-UR, the condition number is given by

$$\text{cond}(\boldsymbol{K}^{ur}) = \frac{\lambda_k^{ur}}{\lambda_1^{ur}} = \frac{\lambda_k}{\lambda_1} \tag{7.26}$$

where $\{\lambda_i^{ur}\}_{i=1}^{k}$ are the eigenvalues of $\boldsymbol{K}^{ur}$. For ISBFM-DR, after some manipulations of the Rayleigh quotient, a bound of the condition number is obtained using eigenvalues of sub-matrices

of $\boldsymbol{K}$. It is expressed as

$$\text{cond}(\boldsymbol{K}^{dr}) = \frac{\lambda_k^{dr}}{\lambda_1^{dr}} \leq \frac{\mu_{\bar{k}} + \eta_{\hat{k}} + \epsilon_N}{\lambda_1} \tag{7.27}$$

where $\{\lambda_i^{dr}\}_{i=1}^k$ are the eigenvalues of $\boldsymbol{K}^{dr}$, which are bounded by the minimum and maximum eigenvalues of $\boldsymbol{K}$, i.e. $\lambda_1 \leq \lambda_i^{dr} \leq \lambda_N, \forall i \in \{1, 2, \ldots, k\}$. We can deduce the property $\lambda_1 \leq \lambda_1^{dr}$. Besides, ϵ_N is the maximal eigenvalue of matrix $\boldsymbol{K}'$ defined as follows

$$\boldsymbol{K}' = \begin{bmatrix} \hat{\boldsymbol{K}}\hat{\boldsymbol{K}}^{-1}\hat{\boldsymbol{K}}^{\mathrm{T}} & \hat{\boldsymbol{K}} \\ \hat{\boldsymbol{K}}^{\mathrm{T}} & \boldsymbol{0} \end{bmatrix} \tag{7.28}$$

The values of ϵ_N and $\eta_{\hat{k}}$ are dependent on the type and the number of enrichment bases that have been used. From the interlacing property in (7.14), we obtain the relationship between the condition numbers of the reduced systems from ISBFM-UR and ISBFM-DR as follows

$$\text{cond}(\boldsymbol{K}^{dr}) \leq \frac{\mu_{\bar{k}}}{\lambda_1} + \frac{\eta_{\hat{k}} + \epsilon_N}{\lambda_1} \leq \frac{\lambda_k}{\lambda_1} + \frac{\eta_{\hat{k}} + \epsilon_N}{\lambda_1} \leq \text{cond}(\boldsymbol{K}^{ur}) + B \tag{7.29}$$

where the term $B > 0$ is affected by the value of $\eta_{\hat{N}}$ due to the use of enrichment bases.

From the theoretical analysis of the stability for these two reduced systems, we can conclude that the ISBFM-DR has a larger bound of condition number than that in ISBFM-UR. The detail of the eigenspectrum of the different matrices will be presented for the numerical examples studied at the end of this chapter.

7.4 Complexity Analysis of the MOR Procedures

The total operation counts in applying each of the two proposed MOR methods are presented in this section and are compared to the operation count in solving the fine scale system. We assume that the full solution is obtained when Cholesky decomposition is directly applied to the full system. The operation counts for the two proposed MOR methods are obtained using additions/subtractions

(A/S) and multiplications/divisions (M/D) comparisons [Hu et al., 2009] [Press et al., 1986]. It is known that

$$1(\text{op}) = 1(\text{A/S}) + 1(\text{M/D}) \tag{7.30}$$

For solving the full system $\boldsymbol{K}\boldsymbol{d} = \boldsymbol{f}$ by Cholesky method, the cost will be

$$\frac{N^3}{6} + N^2 = \frac{(\bar{N} + \hat{N})^3}{6} + (\bar{N} + \hat{N})^2 \text{ op} \tag{7.31}$$

The operation count of model order reduction method from ISBFM-UR can be obtained. We first need to find the eigenvectors of the k smallest eigenvalues of $\boldsymbol{K}$, this is done by using implicitly restarted Lanczos method (IRLM) [Calvetti et al., 1994] [Lehoucq and Sorensen, 1996]. This technique is very efficient when only a few eigenvalues need to be computed, which is the case in model order reduction as reduced models of dimension as small as possible are desired [Bergamaschi and Putti, 2002] [Bai, 2000].

The costs of the IRLM can be decomposed into different steps. The matrix vector products cost γpN, where the parameter γ denotes twice the average number of non-zero entries per row of matrix $\boldsymbol{K}$ in (4.17) and p is the number of additional steps in Lanczos method. The basic Lanczos steps cost $9pN$, the orthogonalization corrections cost $4(kp + p^2)N$ and the application of the implicit restart has a cost of $2N(kp + p^2) + (k + p)^3$. In summary, the overall cost of the IRLM is $(4p + 6k + 9 + \gamma)pN + 2k^2N + (k + p)^3$. In ISBFM-UR, finding the k coefficients $d_i^{ur} = \boldsymbol{\phi}_i^{\mathrm{T}}\boldsymbol{f}/\lambda_i$ costs $(N + 1)k$ and computing $\boldsymbol{P}\boldsymbol{d}^{ur}$ costs kN. The total cost for ISBFM-UR is

$$\begin{aligned} &(4p + 6k + 9 + \gamma) + 2k^2N + (k + p)^3 \\ &+ (N + 1)\,k + kN \end{aligned} \tag{7.32}$$

For the computational count of ISBFM-DR method, we first need to find the operation count for the inverse of $\hat{\boldsymbol{K}}$, which is $\hat{N}^3$, for the construction of $\bar{\boldsymbol{K}}^c = \bar{\boldsymbol{K}} - \hat{\boldsymbol{K}}\hat{\boldsymbol{K}}^{-1}\hat{\boldsymbol{K}}^{\mathrm{T}}$, which is $\bar{N}\hat{N}^2 + \bar{N}^2\hat{N} + \bar{N}^2$ and for the construction of the vector $\bar{\boldsymbol{f}}^c = \bar{\boldsymbol{f}} - \hat{\boldsymbol{K}}\hat{\boldsymbol{K}}^{-1}\hat{\boldsymbol{f}}$ is $\hat{N}^2 + \bar{N}\hat{N} + \bar{N}$.

Then the eigenvectors of the $\bar{k}$ smallest eigenvalues of $\bar{\boldsymbol{K}}^c$ and the eigenvectors of the $\hat{k}$ smallest eigenvalues of $\hat{\boldsymbol{K}}$ are obtained, this is done by using by using IRLM, for which the cost has been detailed in the previous paragraph for ISBFM-UR. In the case of ISBFM-DR, the cost is given by $(4\bar{p}+6k+9+\bar{\gamma})\bar{p}\bar{N}+2\bar{k}^2\bar{N}+(\bar{k}+\bar{p})^3+(\hat{p}+6k+9+\hat{\gamma})\hat{p}\hat{N}+2\hat{k}^2\hat{N}+(\hat{k}+\hat{p})^3$, where $\bar{\gamma}$ is twice the average number of non-zero entries per row of $\bar{\boldsymbol{K}}^c$, and $\hat{\gamma}$ is twice the average number of non-zero entries per row of $\hat{\boldsymbol{K}}$ and $\bar{p}$ and $\hat{p}$ are the numbers of additional steps in Lanczos methods. Finding the $\bar{k}$ coefficients $\bar{d}_j^{dr} = \boldsymbol{\varphi}_j^{\mathrm{T}}\bar{\boldsymbol{f}}^c/\mu_j$ costs $(\bar{N}+1)\bar{k}$ and the computation of $\bar{\boldsymbol{P}}\bar{\boldsymbol{d}}^{dr}$ costs $\bar{k}\bar{N}$. The construction of the vector $\hat{\boldsymbol{f}}^{cdr} = \hat{\boldsymbol{f}} - \hat{\boldsymbol{K}}^{\mathrm{T}}\bar{\boldsymbol{P}}\bar{\boldsymbol{d}}^{dr}$ needs to be considered and its cost is $\bar{N}\hat{N}+\hat{N}$. Finding the $\hat{k}$ coefficients $\hat{d}_l^{dr} = \boldsymbol{\xi}_l^{\mathrm{T}}\hat{\boldsymbol{f}}^{cdr}/\eta_l$ costs $(\hat{N}+1)\hat{k}$ and the computation of $\hat{\boldsymbol{P}}\hat{\boldsymbol{d}}^{dr}$ leads to a cost of $\hat{k}\hat{N}$. In summary, the total cost of ISBFM-DR is

$$\begin{gathered}
(4\bar{p}+6\bar{k}+9+\bar{\gamma})+2\bar{k}^2\bar{N}+\left(\bar{k}+\bar{p}\right)^3 \\
(4\hat{p}+6\hat{k}+9+\hat{\gamma})+2\hat{k}^2\hat{N}+\left(\hat{k}+\hat{p}\right)^3 \\
+\hat{N}^3+\hat{N}^2+\bar{N}\hat{N}^2+\bar{N}^2\hat{N}+\bar{N}^2 \\
+2\bar{N}\hat{N}+\bar{N}+\hat{N} \\
+2\bar{k}\bar{N}+2\hat{k}\hat{N}+\hat{k}+\bar{k}
\end{gathered} \tag{7.33}$$

In the case of $\hat{k}=\hat{N}$, when the enriched part is unreduced, the cost is

$$\begin{gathered}
(4\bar{p}+6\bar{k}+9+\bar{\gamma})+2\bar{k}^2\bar{N}+\left(\bar{k}+\bar{p}\right)^3 \\
+\hat{N}^3+\bar{N}\hat{N}^2+\bar{N}^2\hat{N}+\bar{N}^2 \\
+2\hat{N}^2+2\bar{N}\hat{N}+\bar{N} \\
+2\bar{k}\bar{N}+\bar{k}+\hat{N}
\end{gathered} \tag{7.34}$$

The operation counts for the solving the full system, and the reduced systems from ISBFM-UR and ISBFM-DR are listed in Table 7.1.

From Table 7.1, it appears that the computational cost in ISBFM-DR is slightly lower than that in ISBFM-UR from the fact that $\bar{k}^2+\hat{k}^2 < k^2$ and $\bar{k}^3+\hat{k}^3 < k^3$. Both of these two MOR approaches

Table 7.1: Operation counts

Procedure	Operation counts (op)
Full system	$\frac{N^3}{6} + N^2$
ISBFM-UR	$(4p + 6k + 9 + \gamma)pN$ $+2k^2N + (k+p)^3$ $+(N+1)k + kN$
ISBFM-DR	$(4\bar{p} + 6\bar{k} + 9 + \bar{\gamma})\bar{p}\bar{N}$ $+2\bar{k}^2\bar{N} + (\bar{k}+\bar{p})^3$ $+(4\hat{p} + 6\hat{k} + 9 + \hat{\gamma})\hat{p}\hat{N}$ $+2\hat{k}^2\hat{N} + (\hat{k}+\hat{p})^3$ $+2\hat{N}^2 + \bar{N}\hat{N}^2 + \bar{N}^2\hat{N} + \bar{N}^2$ $+2\bar{N}\hat{N} + \bar{N} + \hat{N}$ $+2\bar{k}\bar{N} + 2\hat{k}\hat{N} + \bar{k} + \hat{k}$

are more efficient than solving the fine scale system directly, due to the fact that $\bar{N}^2 < N^3$ and $\hat{N}^2 < N^3$.

7.5 Numerical Examples and Discussions

In this section, we recall the numerical examples of Chapters 4 and 6 to verify and validate the proposed MOR method, ISBFM-UR and ISBFM-DR.

7.5.1 L-shaped Domain Poisson Problem

The L-shaped domain Poisson problem presented in Section 4.3.1 is further studied on the convergence and the conditioning of the reduced systems. The relative errors in L^∞, in L^2 and in H^1 norms between the reduced solution u^r and the full solution u^h , defined as

$$e_\infty = \frac{\left\|u^h - u^r\right\|_{L^\infty}}{\left\|u^h\right\|_{L^\infty}}, \quad e_0 = \frac{\left\|u^h - u^r\right\|_{L^2}}{\left\|u^h\right\|_{L^2}}, \quad e_1 = \frac{\left\|u^h - u^r\right\|_{H^1}}{\left\|u^h\right\|_{H^1}} \tag{7.35}$$

, are considered for comparison with the theoretical results from Section 7.2.

We use these error measures to study of the accuracy of the reduced models obtained from ISBFM-UR and ISBFM-DR. The relative error in L^∞, in L^2 and in H^1 norm are shown in Figure 7.1, Figure 7.2 and Figure 7.3 where we observe that ISBFM-DR provides a significantly better accuracy than that of ISBFM-UR. Even in the case of using a relatively large reduced system with a percentage of reduction k/N close to 80%, the error of the reduced solution from ISBFM-UR is still of the order $O(10^{-1})$. On the other hand, the solution from ISBFM-DR is much more accurate, where even at a percentage of reduction $k/N = 5\%$, the relative error is of the order $O(10^{-2})$ when one and two enrichment functions are used ($\hat{N} = 1$ and 2). The error is further reduced to $O(10^{-3})$ for $k/N = 5\%$ when five enrichment functions are used ($\hat{N} = 5$). This property in ISBFM-DR can be understood from the fact that when more enrichment basis functions are used, the need for the smooth part of the approximation to approximate the singularity is minimized, and thus leads to a more effective reduced order approximation. This is not the case for ISBFM-UR, where the projection of both singular and smooth parts of the approximation significantly reduces its ability to approximate the singularity behavior in the reduced order space as evidenced in Figures 7.1 - 7.3.

The error bounds provided in Equations (7.15) and (7.16) show that the errors in sup-norm are related to the right-hand side vector of the reduced discrete system with dimension k according to (4.25). The numerical results described above demonstrate that the error from ISBFM-DR is dominated by the smooth part of the solution while the error from ISBFM-UR is dominated by the singular solution. Table 7.2 compares the error bounds of ISBFM-UR and ISBFM-DR for the case when $\bar{N} = 1825$ and $\hat{N} = 1$ based on the analytical derivation in (7.15) and (7.16), respectively. The ratio of errors from these two reduced order approaches is influenced by the eigenvalues λ_{k+1} of $\boldsymbol{K}$ and $\mu_{\bar{k}+1}$ of $\bar{\boldsymbol{K}}^c$, which are also shown in Table 7.2, and as expected from (7.14), are quite close when the same reduced dimension k is used. The ratio of error bounds also depends on the ratio $\sqrt{N/\bar{N}}$, which is nonessential when a small number of enrichment functions is used. Essentially, the error is strongly affected by the norms of the right-hand side vector of the full scale and the reduced systems. In this case, we have the values $\|\boldsymbol{f}\|_\infty = 178.86$ and $\|\bar{\boldsymbol{f}}^c\|_\infty = 0.60$,

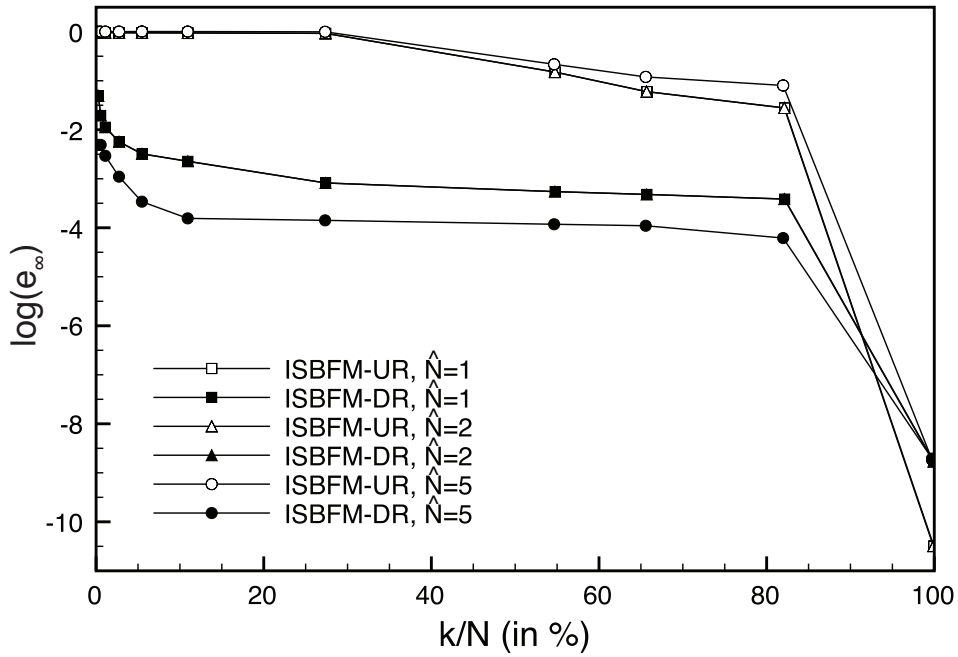

Figure 7.1: Relative error in L^∞ norm for the L-shaped domain Poisson problem

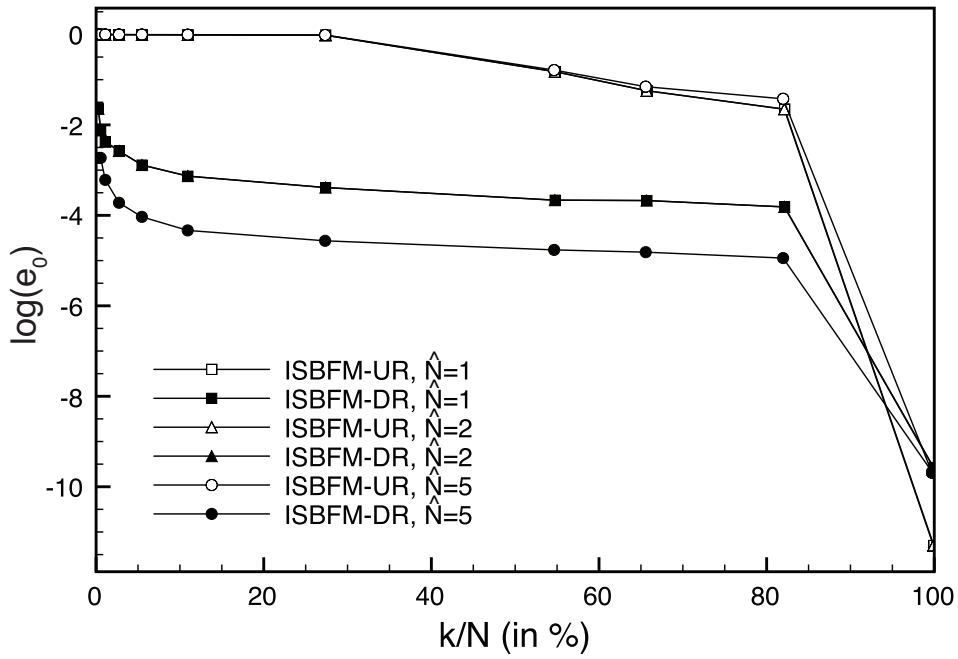

Figure 7.2: Relative error in L^2 norm for the L-shaped domain Poisson problem

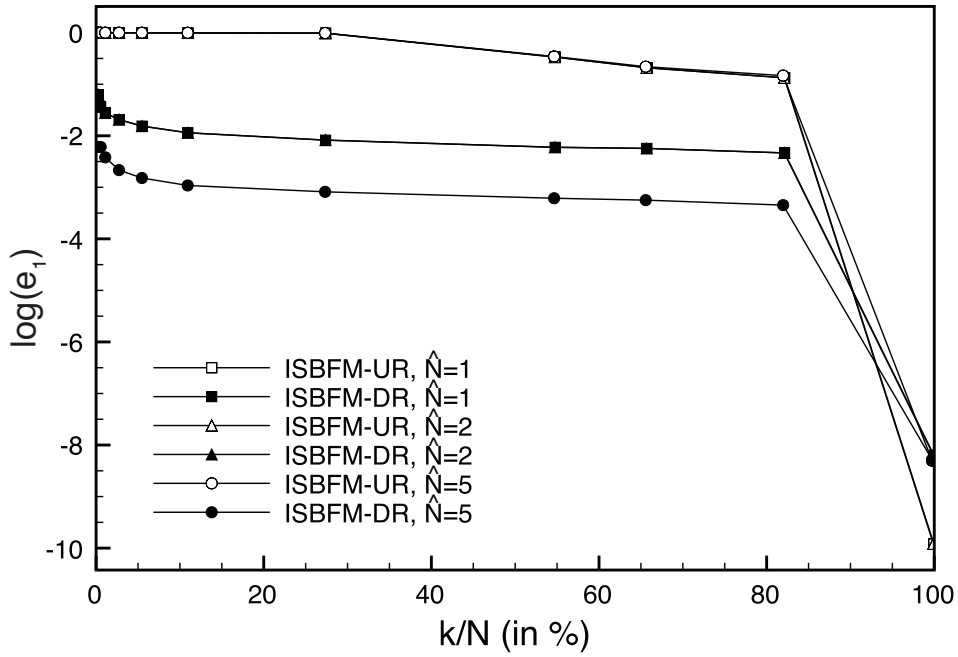

Figure 7.3: Relative error in H^1 norm for the L-shaped domain Poisson problem

where the sup-norm of vector $\bar{\boldsymbol{f}}^c$ is much smaller than the sup-norm of vector $\boldsymbol{f}$. It can be shown that the right-hand side vector dominates the error bound and consequently ISBFM-DR has a much smaller error. Note that the ratio of the error bounds of the two MOR methodscomputed from the numerical solution is around the order of $O(10^{-3})$, which agrees well with the theoretical results given in (7.15) and (7.16) as shown in Table 7.2.

Next, we perform a stability analysis of the reduced systems from ISBFM-DR and ISBFM-UR. The numerical traditional and effective condition numbers of those reduced systems are presented in Figure 7.4 and in Figure 7.5 respectively, while the ones of the fine scale system are displayed in Table 7.3. From the theoretical predictions in (7.24) and (7.25), the reduced systems from both MOR methods are better conditioned than the fine scale system, which is in good agreement with the numerical results shown in Figure 7.4 , Figure 7.5 and Table 7.3. It is worthy to note that the reduced system from ISBFM-UR has a slightly smaller condition number than from ISBFM-DR shown in the numerical results in Figures 7.4 and 7.5, which was also predicted from our estimation of the traditional condition numbers given in (7.29) in Section 7.3 when $(\eta_{\hat{k}}+\epsilon_N)/\lambda_1$ is sufficiently

Table 7.2: Ratio of error bounds of ISBFM-DR and ISBFM-UR for L-shaped domain Poisson problem obtained from numerical results

k/N	0.5%	1%	5%	10%	20%
λ_{k+1}	$4.50\ 10^{-2}$	$9.92\ 10^{-2}$	$5.16\ 10^{-1}$	$9.01\ 10^{-1}$	$1.27\ 10^{0}$
$\mu_{\bar{k}+1}$	$3.91\ 10^{-2}$	$9.89\ 10^{-2}$	$5.01\ 10^{-1}$	$8.98\ 10^{-1}$	$1.27\ 10^{0}$
$\frac{\bar{C}_2\sqrt{\bar{N}}\mu_{\bar{k}+1}^{-1}\|\|\bar{\boldsymbol{f}}^c\|\|_\infty}{\bar{C}_1\sqrt{N}\lambda_{k+1}^{-1}\|\|\boldsymbol{f}\|\|_\infty}$	$1.75\ 10^{-3}$	$1.53\ 10^{-3}$	$1.57\ 10^{-3}$	$1.53\ 10^{-3}$	$1.52\ 10^{-3}$

Table 7.3: Numerical traditional and effective condition numbers of the full system for the L-shaped domain Poisson problem

	$\bar{N}=1825, \hat{N}=1$	$\bar{N}=1825, \hat{N}=2$	$\bar{N}=1825, \hat{N}=5$
Cond($\boldsymbol{K}$)	$3.73\ 10^{7}$	$6.98\ 10^{8}$	$1.43\ 10^{11}$
$\text{Cond}_{\text{Eff}}(\boldsymbol{K})$	$5.73\ 10^{6}$	$6.93\ 10^{8}$	$7.30\ 10^{10}$

large.

The traditional condition numbers for both reduced systems ISBFM-UR and ISBFM-DR are further investigated in details. Taking three cases of reduced systems as examples, the traditional condition numbers of both reduced models were computed numerically and are compared in Table 7.4. The bound of condition number for ISBFM-DR is obtained from (7.27) and shown in Table 7.5. It can be observed that the reduced system from ISBFM-UR has a smaller condition number than that from ISBFM-DR, and this agrees well with the theoretical prediction provided in (7.29). The theoretical results on eigenvalues provided in Section 7.3 can be verified numerically such that $\lambda_1^{ur} = \lambda_1$ and $\lambda_1^{dr} \geq \lambda_1$, where λ_1 is the smallest eigenvalue of $\boldsymbol{K}$ and $\lambda_k^{ur} = \lambda_k$, where λ_k is the k-th eigenvalue of $\boldsymbol{K}$. The interlacing property in (7.14) is also validated, where the eigenvalue $\mu_{\bar{k}}$ of $\bar{\boldsymbol{K}}^c$ is less than or equal to λ_k^{ur}. From Table 7.4, we see that the smallest eigenvalues λ_1^{ur} and λ_1^{dr}

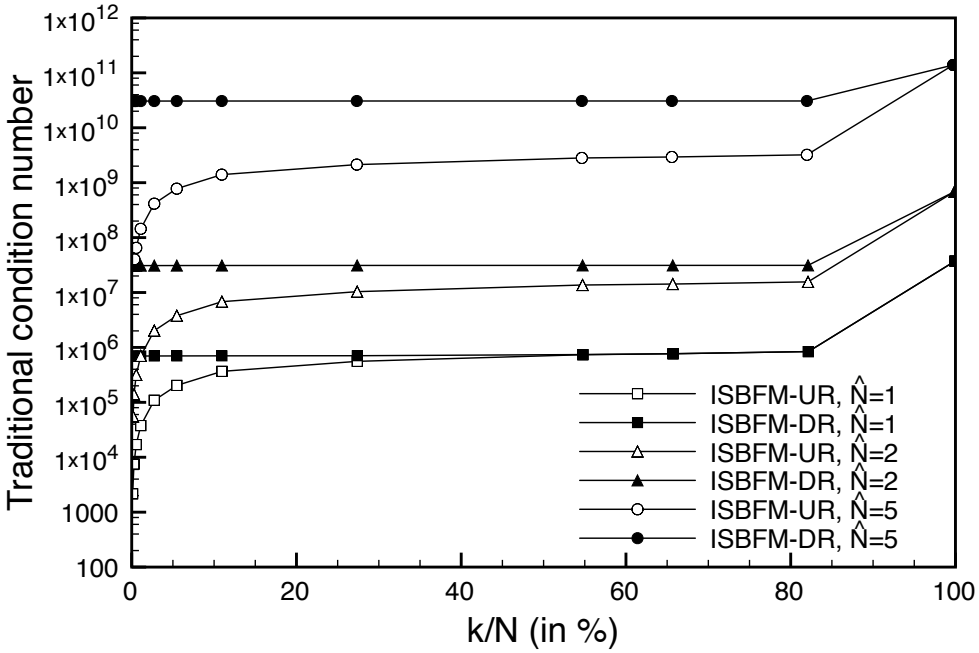

Figure 7.4: Traditional condition number for the L-shaped domain Poisson problem

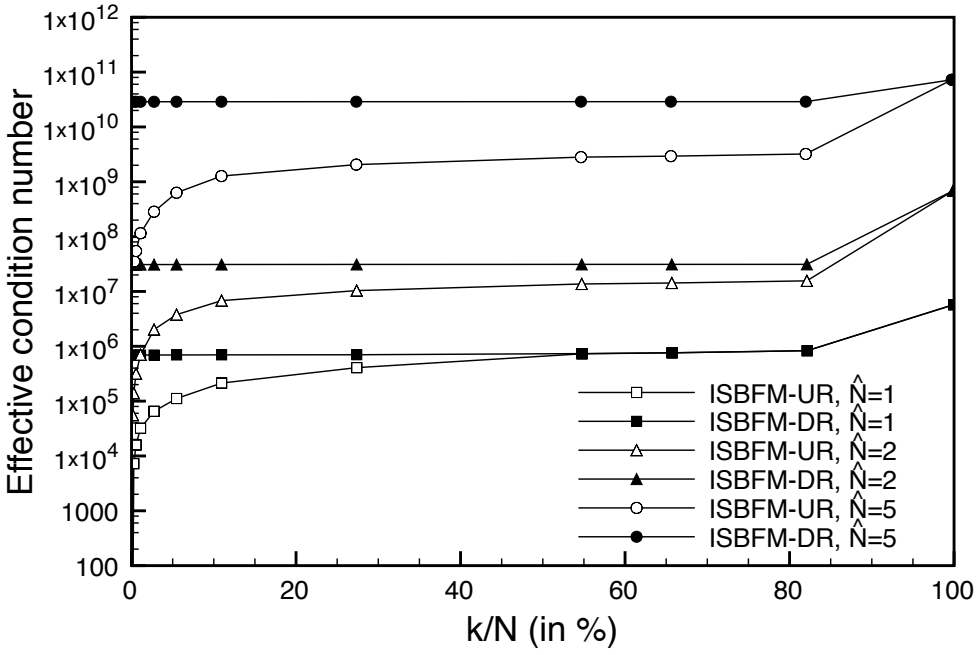

Figure 7.5: Effective condition number for the L-shaped domain Poisson problem

Table 7.4: Numerical traditional condition numbers for ISBFM-UR and ISBFM-DR for the L-shaped domain Poisson problem

$k = \bar{k} + \hat{N}$	λ_1^{ur}	λ_k^{ur}	λ_1^{dr}	λ_k^{dr}	$\lambda_k^{ur}/\lambda_1^{ur}$	$\lambda_k^{dr}/\lambda_1^{dr}$
$k = 5$ $\bar{k} = 4, \hat{N} = 1$	$2.64\ 10^{-6}$	$1.98\ 10^{-2}$	$2.64\ 10^{-6}$	1.84	$7.49\ 10^{3}$	$6.96\ 10^{5}$
$k = 10$ $\bar{k} = 8, \hat{N} = 2$	$1.42\ 10^{-7}$	$4.50\ 10^{-2}$	$1.42\ 10^{-7}$	4.39	$3.16\ 10^{5}$	$3.09\ 10^{7}$
$k = 20$ $\bar{k} = 15, \hat{N} = 5$	$6.91\ 10^{-10}$	$9.97\ 10^{-2}$	$6.91\ 10^{-10}$	21.15	$1.44\ 10^{8}$	$3.06\ 10^{10}$

Table 7.5: Theoretical bounds of the traditional condition number from ISBFM-DR for the L-shaped domain Poisson problem

$k = \bar{k} + \hat{N}$	$\mu_{\bar{k}}$	$\eta_{\hat{N}}$	ϵ_N	$\frac{\mu_{\bar{k}} + \eta_{\hat{N}} + \epsilon_N}{\lambda_1}$
$k = 5$ $\bar{k} = 4, \hat{N} = 1$	$1.83\ 10^{-2}$	1.84	$2.39\ 10^{-1}$	$7.92\ 10^{5}$
$k = 10$ $\bar{k} = 8, \hat{N} = 2$	$3.89\ 10^{-2}$	4.38	$5.18\ 10^{-1}$	$3.47\ 10^{7}$
$k = 20$ $\bar{k} = 15, \hat{N} = 5$	$8.80\ 10^{-2}$	21.11	1.76	$3.32\ 10^{10}$

of both reduced systems ISBFM-UR and ISBFM-DR are very close, which is a result we predicted from Section 7.3. The main difference in condition number from the two reduced models is due to the difference of their maximal eigenvalues λ_k^{ur} and λ_k^{dr}. The eigenvalue λ_k^{dr} is bigger than λ_k^{ur}, which can be explained by the fact that $\hat{\boldsymbol{K}}$ has not been reduced in ISBFM-DR, and the stability of the system from ISBFM-DR is greatly affected by the largest eigenvalue $\eta_{\hat{N}}$ of $\hat{\boldsymbol{K}}$. In Table 7.5, we see that the estimations of the bound of condition numbers in ISBFM-DR are in good agreement with the numerical values of the condition numbers listed in the last column of Table 7.4.

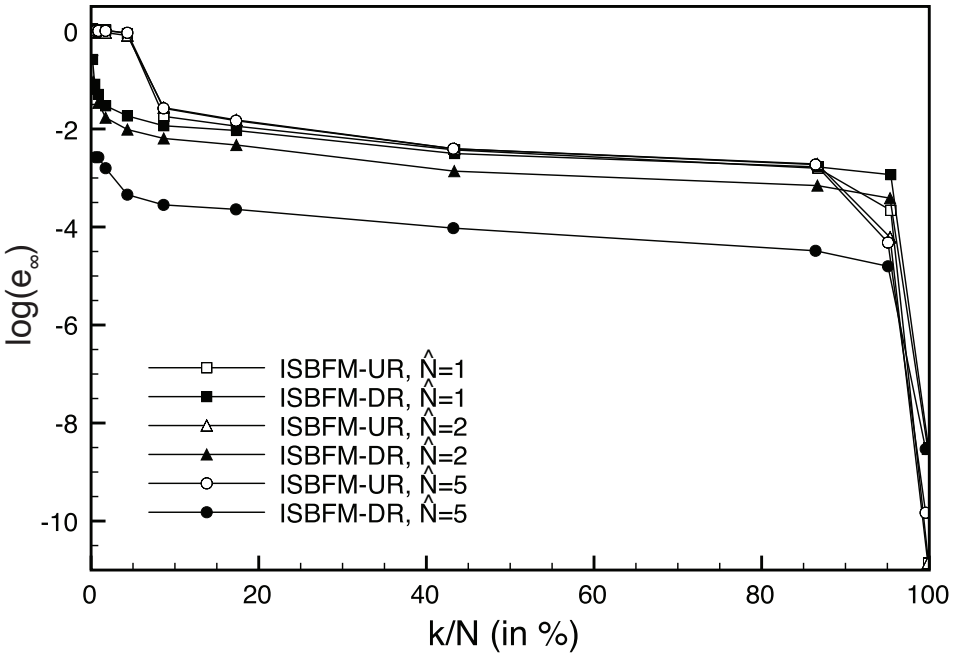

Figure 7.6: Relative error in L^∞ norm for the cracked beam Poisson problem

7.5.2 Cracked Beam Poisson Problem

The accuracy and stability of the proposed MOR methods are also investigated for the cracked beam Poisson problem as described in Section 4.3.2. The relative errors in L^∞, in L^2 and in H^1 norms from (7.35) are also considered in the discussion of convergence.

From Figure 7.6, Figure 7.7 and Figure 7.8, it again shows that ISBFM-DR provides the best accuracy measured in L^∞, L^2 and H^1 norms, especially in the cases where the dimension of the fine scale system is greatly reduced. In this test, the reduced solution from ISBFM-UR starts to recover the full model with an order of accuracy close to $O(10^{-2})$ when the reduced dimension k is greater than 20% of the full dimension N. However, for a lower percentage of k/N, for example, less than 10%, the solution from ISBFM-UR still doesn't capture the overall behavior of the full model. Note that the accuracy of the reduced solution from ISBFM-DR is improved when more enrichment functions are used.

The ratio of analytical error bound for ISBFM-DR from 7.16 to the one for ISBFM-UR from 7.15 is given in Table 7.6 for the case of $\bar{N} = 1152$ and $\hat{N} = 1$. Again, we see from the results

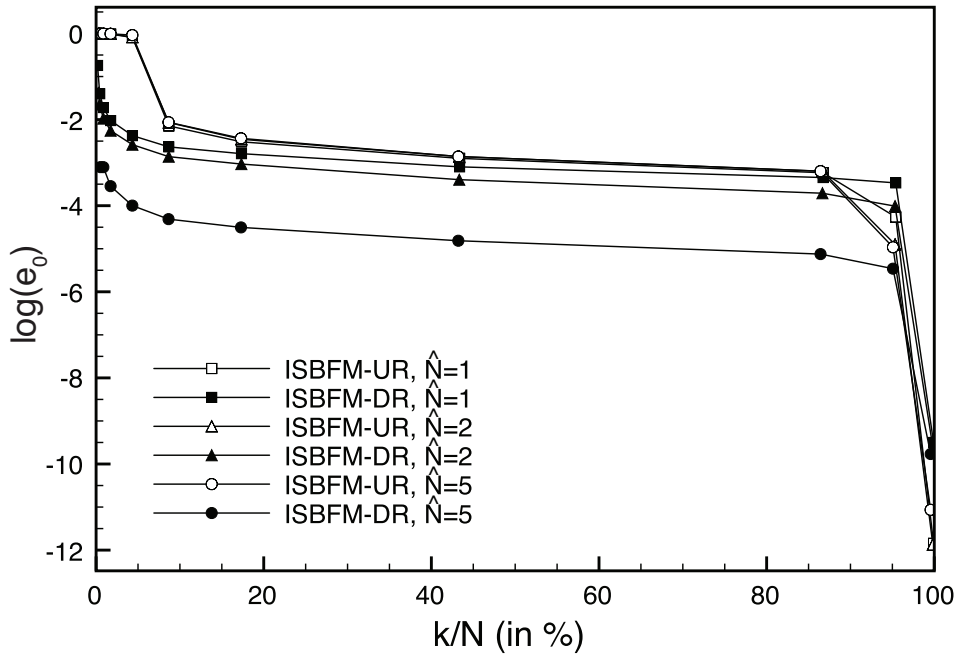

Figure 7.7: Relative error in L^2 norm for the cracked beam Poisson problem

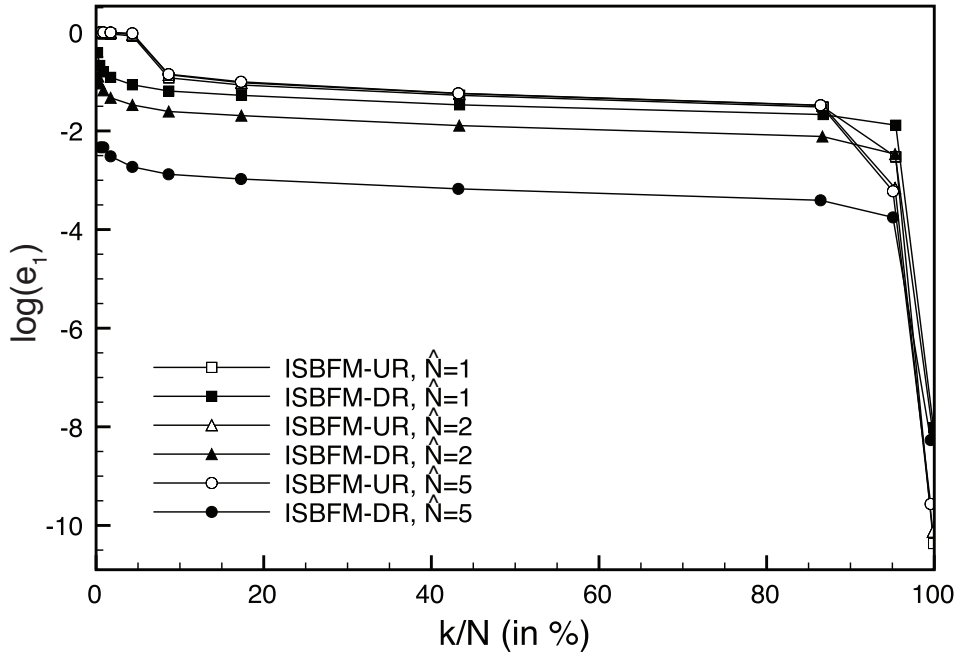

Figure 7.8: Relative error in H^1 norm for the cracked beam Poisson problem

Table 7.6: Ratio of error bounds of ISBFM-DR and ISBFM-UR for cracked beam Poisson problem obtained from numerical results

k/N	0.5%	1%	5%	10%	20%
λ_{k+1}	$4.46\ 10^{-2}$	$1.05\ 10^{-2}$	$4.85\ 10^{-1}$	$8.65\ 10^{-1}$	$1.22\ 10^{0}$
$\mu_{\bar{k}+1}$	$4.02\ 10^{-2}$	$9.27\ 10^{-2}$	$4.84\ 10^{-1}$	$8.65\ 10^{-1}$	$1.22\ 10^{0}$
$\frac{\bar{C}_2\sqrt{\bar{N}}\mu_{\bar{k}+1}^{-1}\|\|\bar{\boldsymbol{f}}^c\|\|_\infty}{\bar{C}_1\sqrt{N}\lambda_{k+1}^{-1}\|\|\boldsymbol{f}\|\|_\infty}$	$2.23\ 10^{-2}$	$2.28\ 10^{-2}$	$2.02\ 10^{-2}$	$2.02\ 10^{-2}$	$2.02\ 10^{-2}$

that the error in ISBFM-DR is smaller than that in ISBFM-UR, with the ratio of error bounds of the order $O(10^{-2})$. These analytical results on error prediction agree quite well with the numerical results in Figure 7.6. In this test, the comparison of the computed norms $\|\boldsymbol{f}\|_\infty = 25.90$ and $\|\bar{\boldsymbol{f}}^c\|_\infty = 0.90$ confirms that the right-hand side of reduced system dominates the estimates of error bounds.

The traditional and effective condition numbers of the reduced systems for this cracked beam Poisson problem can also be observed in Figure 7.9 and Figure 7.10 and similar observations as that in the L-shaped domain Poisson problem can be made. Compared to the condition numbers of the fine scale system shown in Table 7.7, we can see that the reduced systems are better conditioned. In this case, the condition numbers of both reduced models ISBFM-UR and ISBFM-DR are close, even though the reduced system from ISBFM-UR is slightly better conditioned than the one from ISBFM-DR.

A comparison of the condition numbers from ISBFM-UR and ISBFM-DR is presented in Table 7.8 for three different cases of reduced models and the theoretical bound of condition number for ISBFM-DR is given in Table 7.9. Again, numerical results agree with the theoretical prediction given in (7.29), which confirms that the reduced system from ISBFM-UR has a smaller condition number than that from ISBFM-DR. Similar to the observation from the L-shaped domain Poisson problem, the eigenvalue $\eta_{\hat{N}}$ from the non-smooth stiffness sub-matrix $\hat{\boldsymbol{K}}$ is the dominant term that

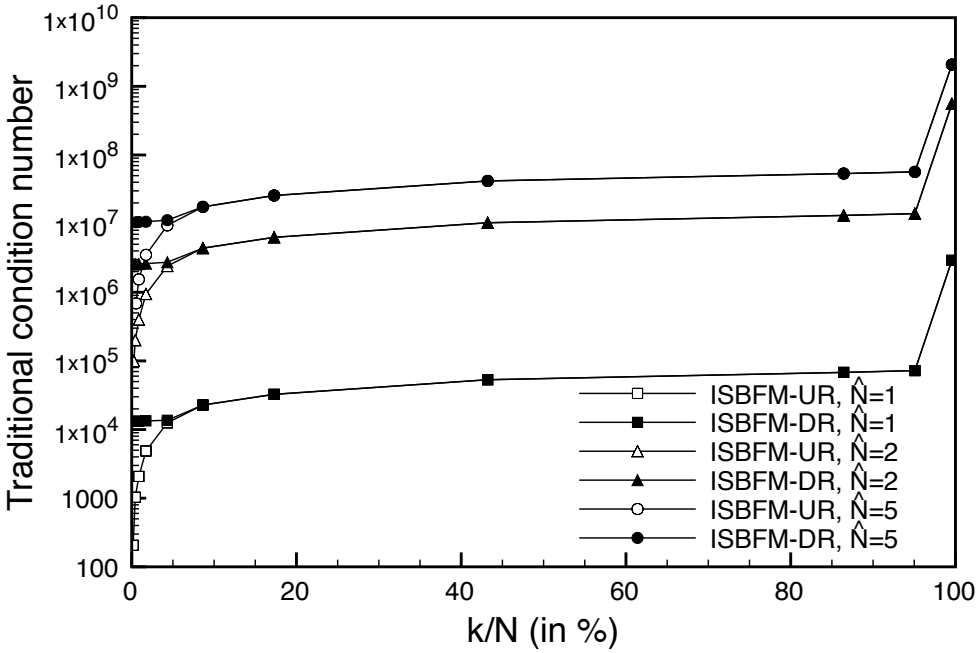

Figure 7.9: Traditional condition number for the cracked beam Poisson problem

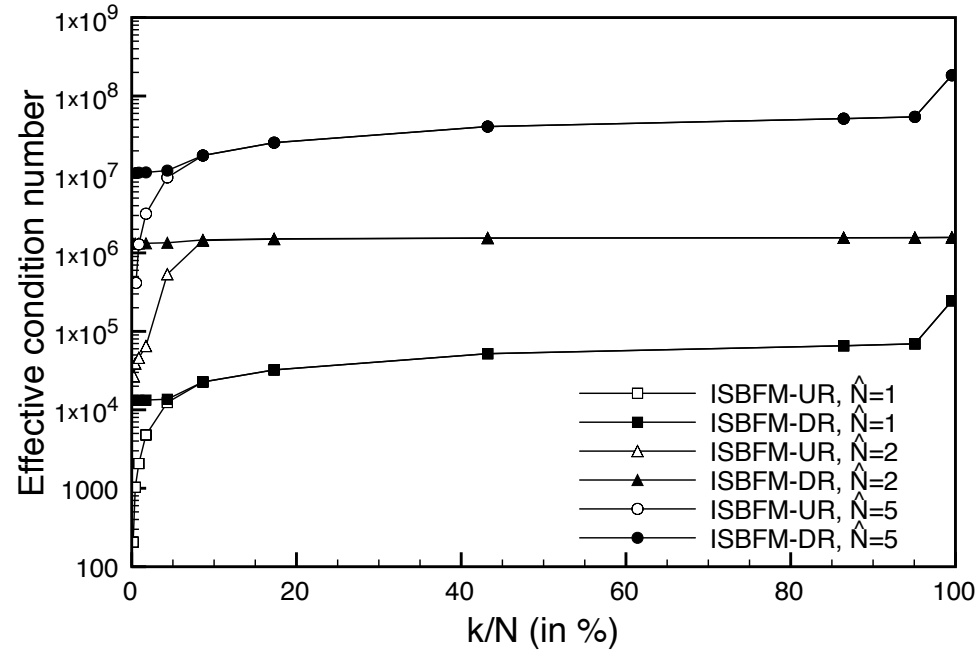

Figure 7.10: Effective condition number for the cracked beam Poisson problem

Table 7.7: Numerical traditional and effective condition numbers of the full system for the cracked beam Poisson problem

	$\bar{N} = 1152, \hat{N} = 1$	$\bar{N} = 1152, \hat{N} = 2$	$\bar{N} = 1152, \hat{N} = 5$
Cond($\boldsymbol{K}$)	$2.94\ 10^{6}$	$5.71\ 10^{8}$	$2.33\ 10^{9}$
$\text{Cond}_{\text{Eff}}(\boldsymbol{K})$	$2.45\ 10^{5}$	$1.58\ 10^{6}$	$1.84\ 10^{8}$

Table 7.8: Numerical traditional condition numbers for ISBFM-UR and ISBFM-DR for the cracked beam Poisson problem

$k = \bar{k} + \hat{N}$	λ_1^{ur}	λ_k^{ur}	λ_1^{dr}	λ_k^{dr}	$\lambda_k^{ur}/\lambda_1^{ur}$	$\lambda_k^{dr}/\lambda_1^{dr}$
$k = 5$ $\bar{k} = 4, \hat{N} = 1$	$3.35\ 10^{-5}$	$3.46\ 10^{-2}$	$3.35\ 10^{-5}$	$4.43\ 10^{-1}$	$1.03\ 10^{3}$	$1.32\ 10^{4}$
$k = 10$ $\bar{k} = 8, \hat{N} = 2$	$1.73\ 10^{-7}$	$6.91\ 10^{-2}$	$1.73\ 10^{-7}$	$4.45\ 10^{-1}$	$4.00\ 10^{5}$	$2.57\ 10^{6}$
$k = 20$ $\bar{k} = 15, \hat{N} = 5$	$4.24\ 10^{-8}$	$1.49\ 10^{-1}$	$4.24\ 10^{-8}$	$4.51\ 10^{-1}$	$3.50\ 10^{6}$	$1.06\ 10^{7}$

Table 7.9: Theoretical bounds of the traditional condition number from ISBFM-DR for the cracked beam Poisson problem

$k = \bar{k} + \hat{N}$	$\mu_{\bar{k}}$	$\eta_{\hat{N}}$	ϵ_N	$\dfrac{\mu_{\bar{k}} + \eta_{\hat{N}} + \epsilon_N}{\lambda_1}$
$k = 5$ $\bar{k} = 4, \hat{N} = 1$	$2.03\ 10^{-2}$	$4.41\ 10^{-1}$	$1.08\ 10^{-1}$	$1.70\ 10^{4}$
$k = 10$ $\bar{k} = 8, \hat{N} = 2$	$6.13\ 10^{-2}$	$4.41\ 10^{-1}$	$2.00\ 10^{-1}$	$4.06\ 10^{6}$
$k = 20$ $\bar{k} = 15, \hat{N} = 5$	$1.19\ 10^{-1}$	$4.43\ 10^{-1}$	$3.05\ 10^{-1}$	$2.05\ 10^{7}$

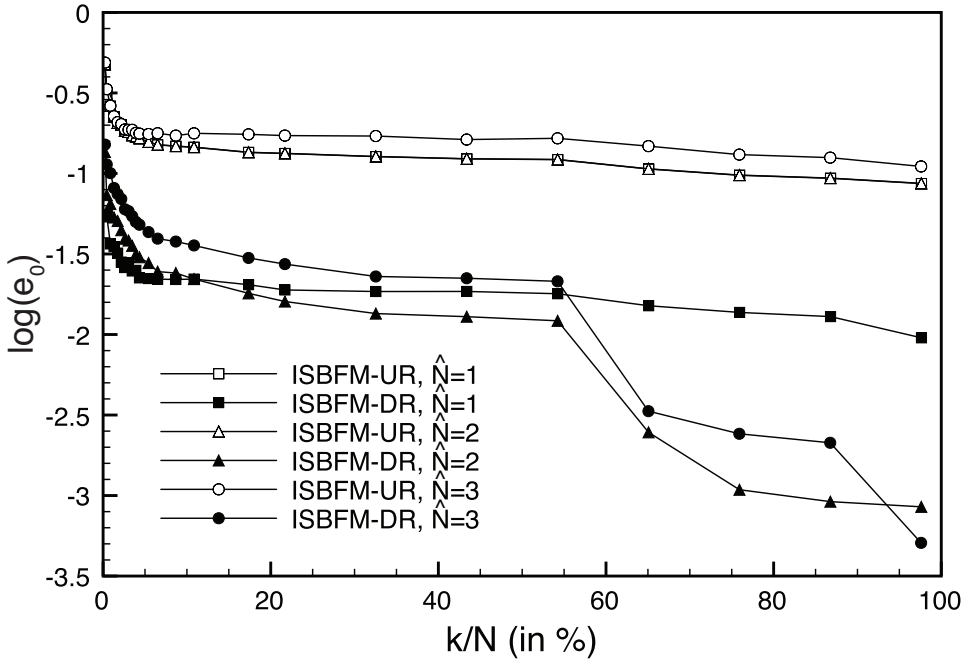

Figure 7.11: Relative error in L^2 norm for the linear elastic fracture problem

influences the bound of the condition number of the reduced stiffness matrix from ISBFM-DR.

7.5.3 Linear Elastic Fracture Problem

The performance of the proposed reduction methods is also examined for the linear elastic fracture problem as described in Section 6.3. The relative errors in L^2 and in H^1 norms are considered in the discussion of convergence.

Figure 7.11 and Figure 7.12 show the relative error plots in L^2 and in H^1 norms, respectively. It can be observed that the reduced model from ISBFM-UR does not converge , and similar phenomenon is also observed in ISBFM-DR for the case of using one set of enrichment functions. However this non-convergence behavior is corrected in ISBFM-DR when more than one set of enrichment functions are used, while in ISBFM-UR the situation remains the same using more enrichment functions.

For the case of $\bar{N} = 4608$ and $\hat{N} = 1$, the ratio of analytical error bound for ISBFM-DR to the one for ISBFM-UR is shown in Table 7.10 for different orders of reduction $k/N =$

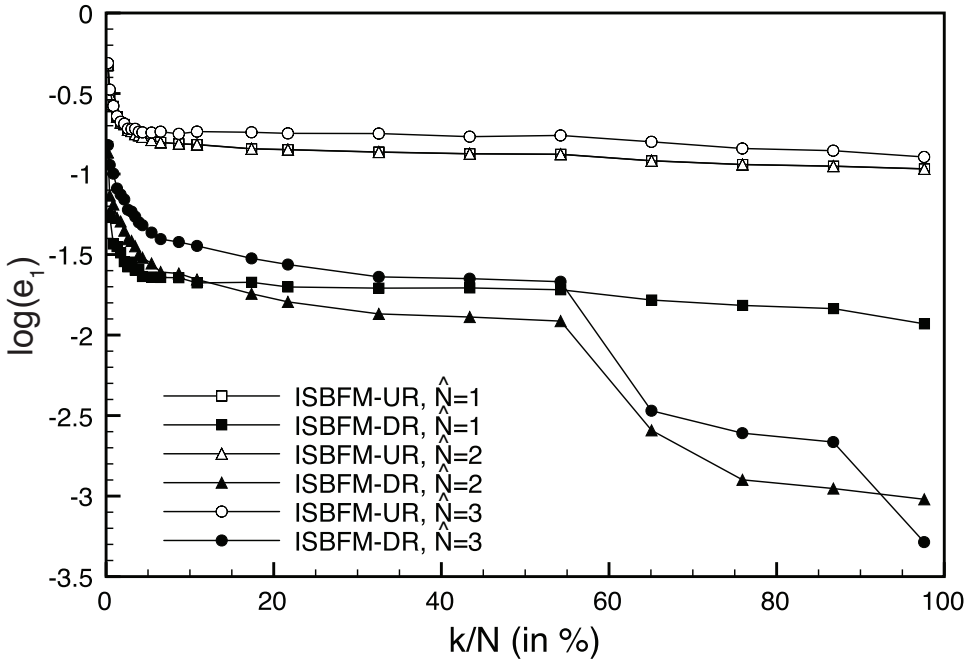

Figure 7.12: Relative error in H^1 norm for the linear elastic fracture problem

Table 7.10: Ratio of error bounds of ISBFM-DR and ISBFM-UR for the linear elastic fracture problem obtained from numerical results

k/N	0.5%	1%	5%	10%	20%
λ_{k+1}	$1.60\ 10^3$	$3.45\ 10^3$	$1.69\ 10^4$	$2.33\ 10^4$	$3.16\ 10^4$
$\mu_{\bar{k}+1}$	$1.56\ 10^3$	$3.45\ 10^3$	$1.68\ 10^4$	$2.32\ 10^4$	$3.16\ 10^4$
$\dfrac{\bar{C}_2\sqrt{\bar{N}}\mu_{\bar{k}+1}^{-1}\|\|\bar{\boldsymbol{f}}^c\|\|_\infty}{\bar{C}_1\sqrt{N}\lambda_{k+1}^{-1}\|\|\boldsymbol{f}\|\|_\infty}$	$1.45\ 10^{-1}$	$1.41\ 10^{-1}$	$1.41\ 10^{-1}$	$1.41\ 10^{-1}$	$1.41\ 10^{-1}$

Table 7.11: Numerical traditional and effective condition numbers of the full system for the linear elastic fracture problem

	$\bar{N} = 4608, \hat{N} = 1$	$\bar{N} = 4608, \hat{N} = 2$	$\bar{N} = 4608, \hat{N} = 3$
Cond($\boldsymbol{K}$)	$2.80\ 10^{12}$	$4.39\ 10^{12}$	$1.05\ 10^{13}$
$\text{Cond}_{\text{Eff}}(\boldsymbol{K})$	$4.73\ 10^{9}$	$7.34\ 10^{9}$	$1.11\ 10^{10}$

$0.5\%, 1\%, 5\%, 10\%, 20\%$. The theoretical ratio of error bounds of the two MOR methods is of the order $O(10^{-1})$, which is in good agreement with the numerical results in Figure 7.11. As shown in the theoretical prediction in Table 7.10, the error of the two MOR methods is mainly due to the values of the norms $\|\boldsymbol{f}\|_\infty = 2.40\ 10^6$ and $\|\bar{\boldsymbol{f}}^c\|_\infty = 3.34\ 10^5$, indicating that the right hand side vectors of the full and reduced systems indeed control the error behavior of the two MOR methods.

Figure 7.13 and Figure 7.14 present the traditional and effective condition numbers of the reduced systems with percentage of reduction k/N up to 11%, and the condition numbers of the fine scale system is also shown in Table 7.11 for comparison. The reduced system from ISBFM-UR is much better conditioned than the one from ISBFM-DR. This result confirms that the conditioning of ISBFM-DR is sacrificed by its accuracy compared to the ISBFM-UR method. However, both MOR methods offer better conditioning in the reduced systems than the fine scale system.

The characteristics of the condition number of the two MOR systems is further studied. The numerical condition numbers from ISBFM-UR and ISBFM-DR are presented in Table 7.12 for three different cases of reduced models, while the analytical condition numbers for ISBFM-DR are given in Table 7.13. From Table 7.12, it is observed that the reduced system from ISBFM-UR does yield a smaller condition number than that from ISBFM-DR. It is also confirmed from the theoretical analysis in Table 7.13 that the eigenvalue $\eta_{\hat{N}}$ from the non-smooth stiffness sub-matrix $\hat{\boldsymbol{K}}$ and the eigenvalue ϵ_N from $\boldsymbol{K}'$ strongly influence the bound of the condition number of the reduced system from ISBFM-DR. The contribution of ϵ_N to the conditioning of the reduced system reflects the influence of the unreduced enrichment part on ISBFM-DR reduced system.

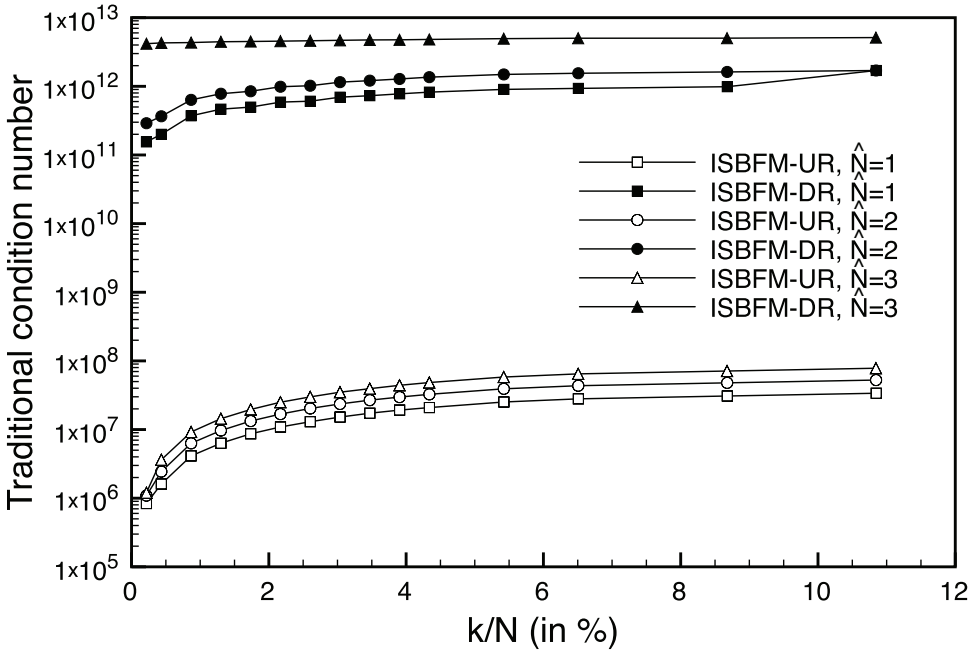

Figure 7.13: Traditional condition number for the linear elastic fracture problem

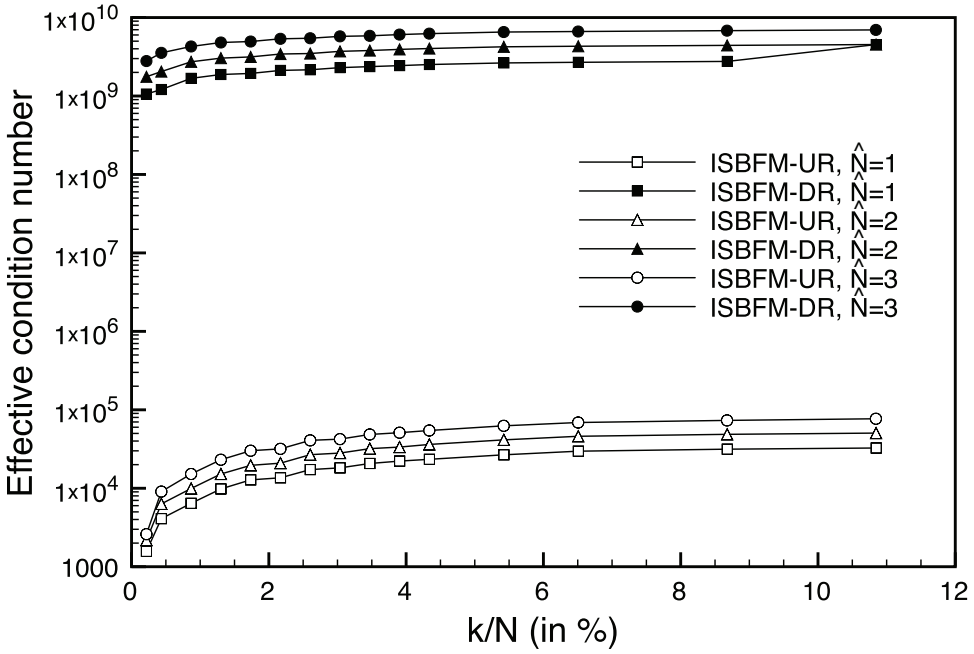

Figure 7.14: Effective condition number for the linear elastic fracture problem

Table 7.12: Numerical traditional condition numbers for ISBFM-UR and ISBFM-DR for the linear elastic fracture problem

$k = \overline{k} + \hat{N}$	λ_1^{ur}	λ_k^{ur}	λ_1^{dr}	λ_k^{dr}	$\lambda_k^{ur}/\lambda_1^{ur}$	$\lambda_k^{dr}/\lambda_1^{dr}$
$k = 5$ $\overline{k} = 4, \hat{N} = 1$	$7.12\ 10^{-4}$	$8.63\ 10^{1}$	$7.88\ 10^{-4}$	$3.92\ 10^{7}$	$1.21\ 10^{5}$	$4.98\ 10^{10}$
$k = 10$ $\overline{k} = 8, \hat{N} = 2$	$4.57\ 10^{-4}$	$4.96\ 10^{2}$	$4.70\ 10^{-4}$	$1.36\ 10^{8}$	$1.09\ 10^{6}$	$2.90\ 10^{11}$
$k = 20$ $\overline{k} = 17, \hat{N} = 3$	$3.07\ 10^{-4}$	$1.12\ 10^{3}$	$3.11\ 10^{-4}$	$1.33\ 10^{9}$	$3.63\ 10^{6}$	$4.29\ 10^{12}$

Table 7.13: Theoretical bounds of the traditional condition number from ISBFM-DR for the linear elastic fracture problem

$k = \overline{k} + \hat{N}$	$\mu_{\overline{k}}$	$\eta_{\hat{N}}$	ϵ_N	$\frac{\mu_{\overline{k}} + \eta_{\hat{N}} + \epsilon_N}{\lambda_1}$
$k = 5$ $\overline{k} = 4, \hat{N} = 1$	$8.63\ 10^{1}$	$4.07\ 10^{3}$	$1.96\ 10^{9}$	$2.76\ 10^{12}$
$k = 10$ $\overline{k} = 8, \hat{N} = 2$	$3.69\ 10^{2}$	$8.39\ 10^{6}$	$1.98\ 10^{9}$	$4.36\ 10^{12}$
$k = 20$ $\overline{k} = 17, \hat{N} = 3$	$9.95\ 10^{2}$	$1.27\ 10^{9}$	$2.81\ 10^{9}$	$1.33\ 10^{13}$

Chapter 8

Conclusion

8.1 Conclusion

MOR techniques for enriched meshfree methods for problems with singularities and discontinuities have been presented in this dissertation. These techniques acknowledge the fact that the reduced approximations are greatly affected by the behavior of the full solution. In the proposed approach, the full approximation consisting of a smooth part from the RK approximation and a non-smooth part using enrichment basis functions has been reduced by a uniform and a decomposed MOR methods. Analytical investigation on the errors, stability, and efficiency of the reduced systems from the proposed MOR methods is also provided in this work.

Under the framework of ISBFM, a modified Galerkin formulation is obtained in which the non-smooth part of solution appears only in the boundary integrals away from the singularity point. This approach avoids the need of higher order integration in the domain and renders the full solution with enhanced accuracy which yields a more effective decomposed reduction method. A formulation under the framework ISBFM has also been developed for fracture mechanics problems, for which appropriate enrichment functions have been derived. Enrichment bases that satisfy the governing equation near the singularity points are introduced for fracture mechanics.

Two ISBFM based reduced order projections were developed for problems with singularities.

The first is a uniform reduction method, termed ISBFM-UR, that projects all smooth and non-smooth DOFs to the reduced order space. The second is a decomposed reduction method, named ISBFM-DR, that intends to retain the singular behavior of the full solution in the reduced order system. Since the number of enrichment bases used for the non-smooth solution is relatively small compared to the smooth DOF, the order reduction of only the smooth part of the solution offers a better accuracy. The performance of the two proposed MOR method is further analyzed through a theoretical error estimation and stability analysis of the reduced order models.

Error bounds of the proposed ISBFM-UR and ISBFM-DR methods have been derived and validated with numerical results. The stability of the two MOR methods has also been investigated and the bounds for the condition numbers of the reduced linear systems have been derived. In addition, the total operational counts of the full and reduced systems have been estimated analytically to provide an estimate of the computational efficiency of the proposed methods.

The proposed MOR methods have been applied to well-known Poisson problems such as a cracked beam problem and a L-shaped domain problem which represent problems with different order of singularities. A linear elastic fracture mechanics problem has also been investigated to study the performance of the proposed MOR methods. The numerical and analytical investigation of the proposed MOR methods show that keeping the enrichment bases or the non-smooth part of solution unprojected in the ISBFM-DR method allows significant reduction of the discrete system while properly capturing the singularity behavior of the model problems. Numerical results also reveals that the proposed ISBFM-DR with decomposed reduction offers better accuracy and faster convergence than ISBFM-UR with uniform reduction of the entire finite dimensional space of the fine scale model. It is also demonstrated numerically and confirmed analytically that while the ISBFM-DR method offers a substantial accuracy and convergence over the ISBFM-UR method, the condition number of the former is slightly increased compared to the later one.

8.2 Recommandations for Future Research

This research focuses on development of MOR methods singularity problem without time variation. It is recommended that this work be used as the basis for extension to singularity problems subjected to transient dynamics. This will allow the reduced order modeling of crack propagation and shock dynamics. Further, incorporation of model order reduction with adaptive refinement could provide an optimal balance of computational accuracy and efficiency for many nonlinear and dynamic problems.

Bibliography

Antoulas, A. C. and Sorensen, D. C. (2001). Approximation of large-scale dynamical systems: An overview. *Appl. Math. and Comput. Sci.*, 11(5):1093–1121.

Arnoldi, W. E. (1951). The principle of minimized iterations in the solution of the matrix eigenvalue problem. *Quart. Appl. Math.*, 9(1):17–29.

Babuška, I. and Melenk, J. M. (1997). The partition of unity method. *Int. J. Numer. Meth. Engng.*, 40(4):727–758.

Bai, Z. (2000). *Templates for the solution of algebraic eigenvalue problems: a practical guide*, volume 11. Siam.

Bai, Z., Slone, R. D., Smith, W. T., and Ye, Q. (1999). Error bound for reduced system model by padé approximation via the lanczos process. *IEEE Trans. Comput.-Aided Design Integr. Circuits Syst.*, 18(2):133–141.

Bai, Z. and Su, Y. (2005). Soar: a second-order arnoldi method for the solution of the quadratic eigenvalue problem. *SIAM J. Matrix Anal. Appl.*, 26(3):640–659.

Belytschko, T. and Black, T. (1999). Elastic crack growth in finite elements with minimal remeshing. *Int. J. Numer. Meth. Engng.*, 45(5):601–620.

Belytschko, T. and Fleming, M. (1999). Smoothing, enrichment and contact in the element-free galerkin method. *Comput. & Struct.*, 71(2):173–195.

Belytschko, T., Krongauz, Y., Fleming, M., Organ, D., and Snm Liu, W. K. (1996a). Smoothing and accelerated computations in the element free galerkin method. *J. Comput. Appl. Math.*, 74(1):111–126.

Belytschko, T., Krongauz, Y., Organ, D., Fleming, M., and Krysl, P. (1996b). Meshless methods: an overview and recent developments. *Comput. Methods Appl. Mech. Engrg.*, 139(1):3–47.

Belytschko, T., Lu, Y. Y., and Gu, L. (1994). Element-free galerkin methods. *Int. J. Numer. Meth. Engng.*, 37(2):229–256.

Belytschko, T., Lu, Y. Y., and Gu, L. (1995a). Crack propagation by element-free galerkin methods. *Engrg. Fracture Mech.*, 51(2):295–315.

Belytschko, T., Lu, Y. Y., Gu, L., and Tabbara, M. (1995b). Element-free galerkin methods for static and dynamic fracture. *Int. J. Solids Structures*, 32(17):2547–2570.

Bergamaschi, L. and Putti, M. (2002). Numerical comparison of iterative eigensolvers for large sparse symmetric positive definite matrices. *Comput. Methods Appl. Mech. Engrg.*, 191(45):5233–5247.

Boley, D. L. (1994). Krylov space methods on state-space control models. *Circ. Syst. Signal Process.*, 13(6):733–758.

Calvetti, D., Reichel, L., and Sorensen, D. C. (1994). An implicitly restarted lanczos method for large symmetric eigenvalue problems. *Electron. Trans. Numer. Anal.*, 2(1):1–21.

Chan, T. F. and Foulser, D. E. (1988). Effectively well-conditioned linear systems. *SIAM J. Sci. Stat. Comp.*, 9(6):963–969.

Chatterjee, A. (2000). An introduction to the proper orthogonal decomposition. *Curr. Sci.*, 78(7):808–817.

Chen, J. S., Han, W., You, Y., and Meng, X. (2003). A reproducing kernel method with nodal interpolation property. *Int. J. Numer. Meth. Engng.*, 56(7):935–960.

Chen, J. S., Pan, C., Roque, C. M. O. L., and Wang, H. P. (1998). A lagrangian reproducing kernel particle method for metal forming analysis. *Comput. Mech.*, 22(3):289–307.

Chen, J. S., Pan, C., and Wu, C. T. (1997). Large deformation analysis of rubber based on a reproducing kernel particle method. *Comput. Mech.*, 19(3):211–227.

Chen, J. S., Pan, C., Wu, C. T., and Liu, W. K. (1996). Reproducing kernel particle methods for large deformation analysis of non-linear structures. *Comput. Methods Appl. Mech. Engrg.*, 139(1):195–227.

Chen, J. S. and Wang, H. P. (2000). New boundary condition treatments in meshfree computation of contact problems. *Comput. Methods Appl. Mech. Engrg.*, 187(3):441–468.

Chen, J. S., Yoon, S., Wang, H. P., and Liu, W. K. (2000). An improved reproducing kernel particle method for nearly incompressible finite elasticity. *Comput. Methods Appl. Mech. Engrg.*, 181(1):117–145.

Chessa, J., Wang, H., and Belytschko, T. (2003). On the construction of blending elements for local partition of unity enriched finite elements. *Int. J. Numer. Meth. Engng.*, 57(7):1015–1038.

Cullum, J. and Zhang, T. (2002). Two-sided arnoldi and nonsymmetric lanczos algorithms. *SIAM J. Matrix Anal. Appl.*, 24(2):303–319.

Elfadel, I. M. and Ling, D. D. (1997). A block rational arnoldi algorithm for multipoint passive model-order reduction of multiport rlc networks. In *Proceedings of the 1997 IEEE/ACM international conference on Computer-aided design*, pages 66–71. IEEE Computer Society.

Elliotis, M., Georgiou, G., and Xenophontos, C. (2005). Solving laplacian problems with boundary singularities: a comparison of a singular function boundary integral method with the *p*/*hp* version of the finite element method. *Appl. Math. Comput.*, 169(1):485–499.

England, A. H. (2003). *Complex variable methods in elasticity*. Courier Dover Publications.

Erdogan, F. and Sih, G. C. (1963). On the crack extension in plates under plane loading and transverse shear. *J. Basic Eng.*, 85:519.

Everson, R. and Sirovich, L. (1995). Karhunen–loeve procedure for gappy data. *J. Opt. Soc. Am. A*, 12(8):1657–1664.

Feldmann, P. and Freund, R. W. (1995). Efficient linear circuit analysis by padé approximation via the lanczos process. *IEEE Trans. Comput.-Aided Design Integr. Circuits Syst.*, 14(5):639–649.

Fernández-Méndez, S. and Huerta, A. (2004). Imposing essential boundary conditions in mesh-free methods. *Comput. Methods Appl. Mech. Engrg.*, 193(12):1257–1275.

Fleming, M., Chu, Y. A., Moran, B., Belytschko, T., Lu, Y. Y., and Gu, L. (1997). Enriched element-free galerkin methods for crack tip fields. *Int. J. Numer. Meth. Engng.*, 40(8):1483–1504.

Fries, T. P. (2008). A corrected xfem approximation without problems in blending elements. *Int. J. Numer. Meth. Engng.*, 75(5):503–532.

Fries, T. P. and Belytschko, T. (2010). The extended/generalized finite element method: an overview of the method and its applications. *Int. J. Numer. Meth. Engng.*, 84(3):253–304.

Gallivan, K., Grimme, E., and Van Dooren, P. (1994). Asymptotic waveform evaluation via a lanczos method. *Appl. Math. Lett.*, 7(5):75–80.

Georgiou, G., Boudouvis, A., and Poullikkas, A. (1997). Comparison of two methods for the computation of singular solutions in elliptic problems. *J. Comput. Appl. Math.*, 79(2):277–287.

Georgiou, G. C., Olson, L., and Smyrlis, Y. S. (1996). A singular function boundary integral method for the laplace equation. *Commun. Numer. Meth. Engng.*, 12(2):127–134.

Gingold, R. A. and Monaghan, J. J. (1977). Smoothed particle hydrodynamics-theory and application to non-spherical stars. *Mon. Not. R. Astron. Soc.*, 181:375–389.

Golub, G. H. and van Van Loan, C. F. (1996). *Matrix computations (Johns Hopkins studies in mathematical sciences)*. The Johns Hopkins University Press.

Griffith, A. A. (1921). The phenomena of rupture and flow in solids. *Phil. Trans. R. Soc. A*, 221:163–198.

Grimme, E. J. (1997). *Krylov projection methods for model reduction*. PhD thesis, Citeseer.

Guan, P. C., Chi, S. W., Chen, J. S., Slawson, T. R., and Roth, M. J. (2011). Semi-lagrangian reproducing kernel particle method for fragment-impact problems. *Int. J. Impact Eng.*, 38(12):1033–1047.

Holmes, P., Lumley, J. L., and Berkooz, G. (1998). *Turbulence, coherent structures, dynamical systems and symmetry*. Cambridge university press.

Horn, R. A. and Johnson, C. R. (2012). *Matrix analysis*. Cambridge university press.

Hu, H. Y., Chen, J. S., and Chi, S. W. (2011). Perturbation and stability analysis of strong form collocation with reproducing kernel approximation. *Int. J. Numer. Meth. Engng.*, 88(2):157–179.

Hu, H. Y., Lai, C. K., and Chen, J. S. (2009). A study on convergence and complexity of reproducing kernel collocation method. *Interact. Multisc. Mechs.*, 2:295–319.

Huang, H. T. and Li, Z. C. (2006). Effective condition number and superconvergence of the trefftz method coupled with high order fem for singularity problems. *Engineering analysis with boundary elements*, 30(4):270–283.

Hung, E. S. and Senturia, S. D. (1999). Generating efficient dynamical models for microelectromechanical systems from a few finite-element simulation runs. *J. Microelectromech. Syst.*, 8(3):280–289.

Igarashi, H. and Honma, T. (1996). A boundary element method for potential fields with corner singularities. *Appl. Math. Model.*, 20(11):847–852.

Irwin, G. R. (1957). Analysis of stresses and strains near the end of a crack traversing a plate. *J. Appl. Mech.*

Irwin, G. R. (1958). Fracture encyclopedia of physics, vol. vi.

Kanninen, M. F. and Popelar, C. H. (1985). *Advanced fracture mechanics*, volume 386. Oxford University Press New York.

Kerfriden, P., Passieux, J. C., and Bordas, S. P. A. (2012). Local/global model order reduction strategy for the simulation of quasi-brittle fracture. *Int. J. Numer. Meth. Engng.*, 89(2):154–179.

Kirby, M. and Sirovich, L. (1990). Application of the karhunen-loeve procedure for the characterization of human faces. *IEEE Trans. Pattern Anal. Mach. Intell.*, 12(1):103–108.

Kosambi, D. D. (1943). Statistics in function space. *J. Indian Math. Soc.*, 7(1):76–88.

Krysl, P. and Belytschko, T. (1997). Element-free galerkin method: Convergence of the continuous and discontinuous shape functions. *Comput. Methods Appl. Mech. Engrg.*, 148(3):257–277.

Lall, S., Krysl, P., and Marsden, J. E. (2003). Structure-preserving model reduction for mechanical systems. *Physica D: Nonlinear Phenomena*, 184(1):304–318.

Lall, S., Marsden, J. E., and Glavaški, S. (2002). A subspace approach to balanced truncation for model reduction of nonlinear control systems. *Int. J. Robust Nonlinear Control*, 12(6):519–535.

Lancaster, P. and Salkauskas, K. (1981). Surfaces generated by moving least squares methods. *Math. Comp.*, 37(155):141–158.

Lanczos, C. (1950). An iteration method for the solution of the eigenvalue problem of linear differential and integral operators. *J. Res. Natl. Bur. Stand.*, 45:255–282.

Lehoucq, R. B. and Sorensen, D. C. (1996). Deflation techniques for an implicitly restarted arnoldi iteration. *SIAM J. Matrix Anal. Appl.*, 17(4):789–821.

Li, F. Z., Shih, C. F., and Needleman, A. (1985). A comparison of methods for calculating energy release rates. *Engrg. Fracture Mech.*, 21(2):405–421.

Li, Z. C. and Lu, T. T. (2000). Singularities and treatments of elliptic boundary value problems. *Math. Comput. Model.*, 31(8):97–145.

Li, Z. C., Lu, T. T., Hu, H. Y., and Cheng, A. H. D. (2005). Particular solutions of laplace's equations on polygons and new models involving mild singularities. *Eng. Anal. Bound. Elem.*, 29(1):59–75.

Li, Z. C., Lu, T. T., Hu, H. Y., and Cheng, A. H. D. (2008). *Trefftz and collocation methods*. WIT Press Southampton.

Li, Z. C., Mathon, R., and Sermer, P. (1987). Boundary methods for solving elliptic problems with singularities and interfaces. *SIAM J. Numer. Anal.*, 24(3):487–498.

Libersky, L. D. and Petschek, A. G. (1991). Smooth particle hydrodynamics with strength of materials. In *Advances in the Free-Lagrange Method Including Contributions on Adaptive Gridding and the Smooth Particle Hydrodynamics Method*, pages 248–257. Springer.

Liu, W. K., Jun, S., Li, S., Adee, J., and Belytschko, T. (1995a). Reproducing kernel particle methods for structural dynamics. *Int. J. Numer. Meth. Engng.*, 38(10):1655–1679.

Liu, W. K., Jun, S., and Zhang, Y. F. (1995b). Reproducing kernel particle methods. *Int. J. Numer. Meth. Fluids*, 20(8-9):1081–1106.

Loève, M. (1945). Fonctions aléatoires de second ordre. *CR Acad. Sci. Paris*, 220:380.

Lu, T. T., Hu, H. Y., and Li, Z. C. (2004). Highly accurate solutions of motz's and the cracked beam problems. *Eng. Anal. Bound. Elem.*, 28(11):1387–1403.

Lu, Y. Y., Belytschko, T., and Gu, L. (1994). A new implementation of the element free galerkin method. *Comput. Methods Appl. Mech. Engrg.*, 113(3):397–414.

Lucy, L. B. (1977). A numerical approach to the testing of the fission hypothesis. *The astronomical journal*, 82:1013–1024.

Lumley, J. L. (1967). The structure of inhomogeneous turbulent flows. *Atmospheric turbulence and radio wave propagation*, pages 166–178.

Melenk, J. M. and Babuška, I. (1996). The partition of unity finite element method: basic theory and applications. *Comput. Methods Appl. Mech. Engrg.*, 139(1):289–314.

Moës, N., Dolbow, J., and Belytschko, T. (1999). A finite element method for crack growth without remeshing. *Int. J. Numer. Meth. Engng.*, 46:131–150.

Moore, B. (1981). Principal component analysis in linear systems: Controllability, observability, and model reduction. *IEEE Trans. Auto. Control*, 26(1):17–32.

Moran, B. and Shih, C. F. (1987). Crack tip and associated domain integrals from momentum and energy balance. *Engrg. Fracture Mech.*, 27(6):615–642.

Nayroles, B., Touzot, G., and Villon, P. (1992). Generalizing the finite element method: diffuse approximation and diffuse elements. *Comput. Mech.*, 10(5):307–318.

Nitsche, J. (1971). Über ein variationsprinzip zur lösung von dirichlet-problemen bei verwendung von teilräumen, die keinen randbedingungen unterworfen sind. In *Abhandlungen aus dem Mathematischen Seminar der Universität Hamburg*, volume 36, pages 9–15. Springer.

Nuismer, R. J. (1975). An energy release rate criterion for mixed mode fracture. *Int. J. Fracture*, 11(2):245–250.

Olson, L. G., Georgiou, G. C., and Schultz, W. W. (1991). An efficient finite element method for treating singularities in laplace's equation. *J. Comput. Phys.*, 96(2):391–410.

Organ, D., Fleming, M., Terry, T., and Belytschko, T. (1996). Continuous meshless approximations for nonconvex bodies by diffraction and transparency. *Comput. Mech.*, 18(3):225–235.

Padé, H. (1899). Mémoire sur les développements en fractions continues de la fonction exponentielle, pouvant servir d'introduction à la théorie des fractions continues algébriques. In *Annales scientifiques de l'École Normale Supérieure*, volume 16, pages 395–426. Société mathématique de France.

Pillage, L. T. and Rohrer, R. A. (1990). Asymptotic waveform evaluation for timing analysis. *IEEE Trans. Comput.-Aided Design Integr. Circuits Syst.*, 9(4):352–366.

Press, W. H., Flannery, B. P., Teukolsky, S. A., and Vetterling, W. T. (1986). Numerical recipes: The art of scientific computing, 818 pp.

Randles, P. W. and Libersky, L. D. (1996). Smoothed particle hydrodynamics: some recent improvements and applications. *Comput. Methods Appl. Mech. Engrg.*, 139(1):375–408.

Rathinam, M. and Petzold, L. R. (2003). A new look at proper orthogonal decomposition. *SIAM J. Numer. Anal.*, 41(5):1893–1925.

Rice, J. R. (1968). A path independent integral and the approximate analysis of strain concentration by notches and cracks. *J. Appl. Mech.*, 35:379–386.

Salimbahrami, B. and Lohmann, B. (2006). Order reduction of large scale second-order systems using krylov subspace methods. *Linear Algebra Appl.*, 415(2):385–405.

Schilders, W. H. A., Van Der Vorst, H. A., and Rommes, J. (2008). *Model order reduction: theory, research aspects and applications*, volume 13. Springer.

Shih, C. H. F., Moran, B., and Nakamura, T. (1986). Energy release rate along a three-dimensional crack front in a thermally stressed body. *Int. J. Fracture*, 30(2):79–102.

Sih, G. C. (1974). Strain-energy-density factor applied to mixed mode crack problems. *Int. J. Fracture*, 10(3):305–321.

Volkwein, S. (2001). Optimal control of a phase-field model using proper orthogonal decomposition. *ZAMM-J. Appl. Math. Mech.*, 81(2):83–97.

Wang, L., Chen, J. S., and Hu, H. Y. (2010). Subdomain radial basis collocation method for fracture mechanics. *Int. J. Numer. Meth. Engng.*, 83(7):851–876.

Westergaard, H. M. (1997). Bearing pressures and cracks. *SPIE MILESTONE SERIES MS*, 137:18–22.

Wiederhorn, S. M. (1969). Fracture surface energy of glass. *J. Amer. Ceramic Soc.*, 52(2):99–105.

Willcox, K. and Peraire, J. (2002). Balanced model reduction via the proper orthogonal decomposition. *AIAA Journal*, 40(11):2323–2330.

Williams, M. L. (1952). Stress singularities resulting from various boundary conditions in angular corners of plates in extension. *J. Appl. Mech.*, 19(4):526–528.

Williams, M. L. (1957). On the stress distribution at the base of a stationary crack. *J. Appl. Mech.*, 24(1):109–114.

Zhu, T. and Atluri, S. N. (1998). A modified collocation method and a penalty formulation for enforcing the essential boundary conditions in the element free galerkin method. *Comput. Mech.*, 21(3):211–222.